Mr. Melvin G. Rosche, Code RV-2

N70 29006 N70-29006

NASA TECHNICAL MEMORANDUM

NASA TM X-53820

1969

NASA TM X-53820

THERMOPHYSICS RESEARCH AT MSFC

RESEARCH ACHIEVEMENTS REVIEW

VOLUME III REPORT NO. 6

SCIENCE AND ENGINEERING DIRECTORATE
GEORGE C. MARSHALL SPACE FLIGHT CENTER
MARSHALL SPACE FLIGHT CENTER, ALABAMA

CASE FILE COPY

GEORGE C. MARSHALL SPACE FLIGHT CENTER

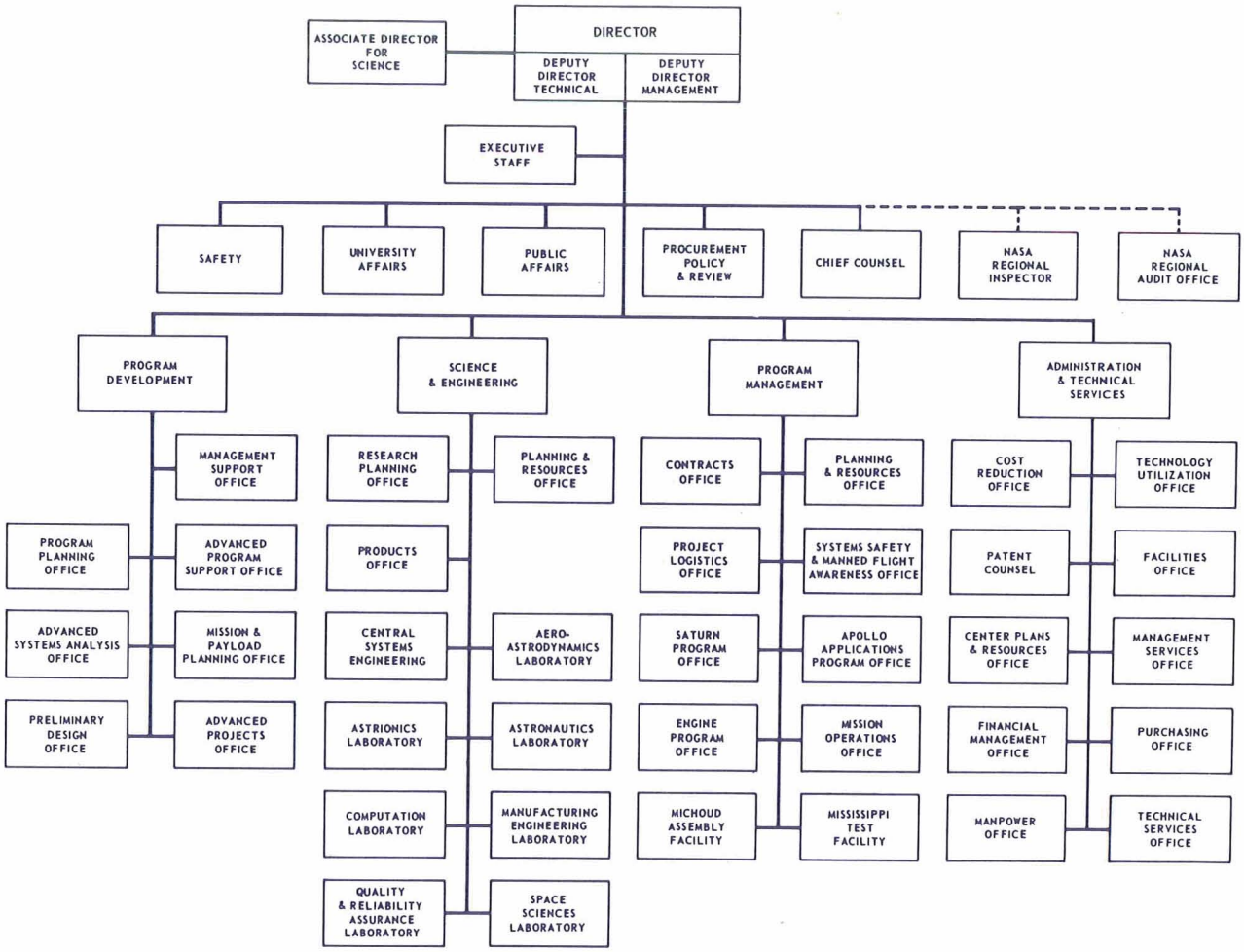

RESEARCH ACHIEVEMENTS REVIEWS COVER THE FOLLOWING FIELDS OF RESEARCH

- Radiation Physics
- Thermophysics
- Chemical Propulsion
- Cryogenic Technology
- Electronics
- Control Systems
- Materials
- Manufacturing
- Ground Testing
- Quality Assurance and Checkout
- Terrestrial and Space Environment
- Aerodynamics
- Instrumentation
- Power Systems
- Guidance Concepts
- Astrodynamics
- Advanced Tracking Systems
- Communication Systems
- Structures
- Mathematics and Computation
- Advanced Propulsion
- Lunar and Meteoroid Physics

NASA TM X- 53820

NATIONAL AERONAUTICS AND SPACE ADMINISTRATION
WASHINGTON, D. C.

RESEARCH ACHIEVEMENTS REVIEW
VOLUME III REPORT NO. 6

THERMOPHYSICS RESEARCH AT MSFC

SCIENCE AND ENGINEERING DIRECTORATE
GEORGE C. MARSHALL SPACE FLIGHT CENTER
MARSHALL SPACE FLIGHT CENTER, ALABAMA

1969

PREFACE

In February, 1965, Dr. Ernst Stuhlinger, Director, Research Projects Laboratory (now Space Sciences Laboratory), initiated a series of Research Achievements Reviews which set forth those achievements accomplished by the laboratories of the Marshall Space Flight Center. Each review covered one or two fields of research in a form readily usable by specialists, systems engineers and program managers. The review of February 24, 1966, completed this series. Each review was documented in the "Research Achievements Review Series."

In March, 1966, a second series of Research Achievements Reviews was initiated. This second series emphasized research areas of greatest concentration of effort, of most rapid progress, or of most pertinent interest and was published as "Research Achievements Review Reports, Volume II." Volume II covered the reviews from March, 1966, through February, 1968.

This third series of Research Achievements Reviews was begun in March, 1968, and continues the concept introduced in the second series. Reviews of the third series are designated Volume III and will span the period from March, 1968, through February, 1970.

The papers in this report were presented January 30, 1969

William G. Johnson
Director
Research Planning Office

CONTENTS. . .

Page

INTRODUCTION TO THERMOPHYSICS RESEARCH AT MSFC

By Gerhard Heller 1

THERMAL CONTROL COATINGS DEVELOPMENT

By Dan Gates

Page

SUMMARY 3

INTRODUCTION. 3

PAINTS 7

PIGMENTS 8

CONCLUSIONS AND FUTURE PLANS 10

REFERENCES. 11

BIBLIOGRAPHY. 13

LIST OF ILLUSTRATIONS

Figure	Title	Page
1.	Heat Balance in a Spacecraft	3
2.	Examples of Some Ideal Non-Spectral Surfaces	4
3.	Basic Types of Surfaces	4
4.	Steady State Temperatures of a Flat Plate for Mars, Earth, and Venus Orbits	4
5.	Solar Radiation after Johnson and NASA SP-8005	5
6.	Solar Spectral Irradiance: GSFC Data (1968) and Johnson Data (1954)	5
7.	Spectral Intensity of B-H6 Ultraviolet Lamp	6
8.	Solar Absorptance Versus Thickness in Zinc Oxide/Potassium Silicate Coatings (Z-93)	7
9.	Effect of 4170 ESH in Vacuum on Solar Spectral Reflectance of Zinc Oxide (Calcined) — Potassium Silicate Coating (Sample Z-93)	7
10.	Temperature Cycling of Pegasus II Surface (Grey and Z-93 Surfaces)	7

CONTENTS (Continued). . .

		Page
11.	Z-93 At 400 X Magnification	8
12.	Spectral Reflectance of ZnO and TiO_2 (Wet-Sprayed Powders)	8
13.	Spectral Reflectance of Zn_2TiO_4 (Wet-Sprayed Powder) — 850° C Preparation	8
14.	Spectral Reflectance of Zn_2TiO_4 (Wet-Sprayed Powder) — 950° C Preparation	9
15.	Spectral Reflectance of Zn_2TiO_4 (Wet-Sprayed Powder) — 1050° C Preparation	9
16.	Absolute Hemispherical Reflectance of Zn_2TiO_4, Extracted (Wet-Sprayed Powder) — 1000° C Preparation	9
17.	Absolute Hemispherical Reflectance of Zn_2TiO_4, Extracted (Wet-Sprayed Powder) — 1100° C Preparation	9
18.	Absolute Hemispherical Reflectance of $CaWO_4$ (Wet-Sprayed Powder)	10
19.	Spectral Reflectance of $CaWO_4$ in OI-650 Paint and with 600 ESH of Ultraviolet	10
20.	Absolute Hemispherical Reflectance of $BaWO_4$ (Wet-Sprayed Powder)	10

STUDIES RELATED TO THE DEVELOPMENT OF COLOR CENTERS IN ZINC OXIDE

By Gary M. Arnett and Roger L. Kroes

	Page
SUMMARY	15
INTRODUCTION	15
DISCUSSION OF DEGRADATION MODEL AND MEASUREMENTS USED IN INVESTIGATING THE MODEL	15
RESULTS AND CONCLUSIONS	16
REFERENCES	19

LIST OF ILLUSTRATIONS

Figure	Title	Page
1.	Luminescence Facility	16
2.	Photoluminescence Spectrum from Activated ZnO	17
3.	Luminescence Maximum for Excitation Wavelengths 3000Å to 4000Å from Activated ZnO	17
4a.	ESR from Sample Radiated with 0.2 to 0.4 μ Wavelength Radiation using A-H6 High Pressure Mercury Lamp	18

CONTENTS (Continued)...

		Page
4b.	ESR from Sample Radiated with 0.8 μ Wavelength Radiation	18
5.	Comparison of Experimental and Theoretical Line Shapes	18
6a.	ESR Spectra of a Mechanically Damaged Sample	18
6b.	Annealing Effect on the Mechanically Damaged Sample	18

EFFECT OF SOLAR WIND ON THERMAL CONTROL COATINGS

By Donald R. Wilkes

	Page
INTRODUCTION	21
SOLAR WIND SIMULATION	21
ENVIRONMENTAL TESTING	21
REFERENCES	23
BIBLIOGRAPHY	23

LIST OF TABLES

Table	Title	Page
I.	Proton and Alpha Particle Content in the Solar Wind	22

LIST OF ILLUSTRATIONS

Figure	Title	Page
1.	Ion Generator for Solar Wind Simulation	21
2.	In Situ Chamber	22
3.	Solar Wind Effects on Z-93	22

PORTABLE SOLAR REFLECTOMETER

By Joe E. Zimmerman

	Page
SUMMARY	25
INTRODUCTION	25
DESIGN GUIDELINES	25

CONTENTS (Continued)...

	Page
DETECTION METHODS	25
OPTICAL SYSTEM DESIGN	27
PROTOTYPE DESIGN	28
CONCLUSIONS	31

LIST OF TABLES

Table	Title	Page
I.	Design Goals	26
II.	Reflectometer Performance Data	31

LIST OF ILLUSTRATIONS

Figure	Title	Page
1.	Integrating Sphere Theory	26
2.	Filter Wheel	27
3.	Reflectometer Optical Design	28
4.	Optical Mechanical Relationship of Reflectometer	29
5.	Block Diagram of Reflectometer Electronics	29
6.	Laboratory Prototype Reflectometer	30

CONTAMINATION DURING THERMAL VACUUM TESTING

By James M. Zwiener

	Page
SUMMARY	33
INTRODUCTION	33
TEST APPROACH	33
TEST RESULTS	36
CONCLUSIONS	37
REFERENCE	38

CONTENTS (Continued). . .

LIST OF ILLUSTRATIONS

Figure	Title	Page
1.	Laboratory Vacuum System — Oil	33
2.	Vacuum System — Oil	34
3.	Sample Chamber — Oil System	34
4.	Laboratory Vacuum System — Ion	35
5.	Vacuum System — Ion	35
6.	Sample Chamber — Ion System	35
7.	Reflectance Degradation as Related to Ultraviolet Exposure	36
8.	Reflectance Degradation in an Oil Vacuum System	37
9.	Scanning Electron Microscope Picture	38

THE PTD500 THERMAL ANALYZER SYSTEM

By Frederick D. Bachtel

	Page
SUMMARY	39
LIST OF SYMBOLS	39
INTRODUCTION	40
SYSTEM ORGANIZATION	40
SYSTEM INTEGRATION	42
LUMPED PARAMETER FUNDAMENTALS	43
NETWORK ELEMENTS	46
DIAGNOSTICS	47
INFRARED RADIATION	47
STEADY-STATE SOLUTION	48
TRANSIENT SOLUTION	49
CONCLUSION	52

CONTENTS (Continued). . .

LIST OF ILLUSTRATIONS

Figure	Title	Page
1.	PTD500 Module Breakdown and Data Allocation	41
2.	PTD500 Input/Output Data Flow	42
3.	Lumped Parameter Representation	45
4.	PTD500 Capabilities	52
5.	PTD500 Capacity	52

THERMAL SIMILITUDE

By Jimmy R. Watkins

	Page
SUMMARY	53
INTRODUCTION	53
CONTRACTUAL EXPERIMENTAL EFFORT	53
CONCLUSION	59
REFERENCES	60

LIST OF TABLES

Table	Title	Page
I.	Structural Scaling Laws	54
II.	Temperature History of the Prototype's Primary Mirror (°K)	59

LIST OF ILLUSTRATIONS

Figure	Title	Page
1.	Two-Meter OTES Concept	53
2.	Orbit Configuration	54
3.	Geometry of the Model	55
4.	Thermocouple Locations on the Model	55

CONTENTS (Continued)...

		Page
5.	Primary Mirror Thermocouples	55
6.	Assembled Optical System	56
7.	Assembled Model Before Testing	56
8.	Transient Thermal Behavior, Section A	56
9.	Transient Thermal Behavior, Section B	57
10.	Transient Thermal Behavior, Section C	57
11.	Transient Thermal Behavior, Section D and Primary Mirror	58
12.	Temperature History for the Prototype's Primary Mirror and the Surrounding Area	58
13.	Temperature History for the Prototype's Secondary Support Rods	59
14.	Thermal Expansion of the Model's Secondary Support Rods	59

PHASE CHANGE THERMAL CONTROL DEVELOPMENT

By Tommy C. Bannister

	Page
INTRODUCTION	61
SUMMARY OF IMPORTANT FACTORS AND PROBLEM AREAS	61
MAJOR ACTIVITIES IN THE AREA	62
OPTICAL OBSERVATION OF CRYSTAL GROWTH	63

LIST OF TABLES

Table	Title	Page
I.	Thermal Factors/Other Factors	62
II.	Summary of Major Activities	62

LIST OF ILLUSTRATIONS

Figure	Title	Page
1.	The Space Radiator Experiment	63
2.	Optical Observation of Crystal Growth	64

CONTENTS (Continued). . .

		Page
3.	A Typical Microphotograph of a Solid/Liquid Interface (34X)	65
4.	Peak Heights Versus Growth Velocity in a Binary Mixture of 5 Percent Hexadecane and 95 Percent Octadecane	65

SPACE APPLICATIONS OF THE HEAT PIPE

By C. G. Fritz

	Page
SUMMARY	67
INTRODUCTION	67
OPERATION OF A HEAT PIPE	68
ANALYSIS OF THE HEAT PIPE	68
EXPERIMENTAL	70
HEAT PIPE APPLICATION	73
REFERENCE	79

LIST OF TABLES

Table	Title	Page
I.	Summary of Experimental Heat Inputs and Losses for Heat Pipes as Radiating Fins	72

LIST OF ILLUSTRATIONS

Figure	Title	Page
1.	Heat Pipe Operational Schematic	67
2.	Equations for a Heat Pipe	70
3.	Comparison of Fluids for a Heat Pipe	71
4.	Thermal Conductivity versus Temperature	71
5.	Comparison of a Heat Pipe and a Solid Rod	72
6.	Heat Input versus L/D	73
7.	Temperature Variation with Time	73

CONTENTS (Continued)...

		Page
8.	Temperature Equalization of an Optical Mirror	73
9.	Temperature Equalization by a Heat Pipe Device	74
10.	A Device (Wick) Whose Arrangement is Similar to the Operation of a Heat Pipe Can Prevent Excessive Condensation on the Cold Side of a Spacecraft Cabin	75
11.	Heat Pipe Thermally Connects the Cold Plate to the External Spacecraft Shell	76
12.	Thermal Radiator	76
13.	Thermal Conditioning Heat Pipe — Sublimator Panel	76
14.	Heat Pipe Radiator	77
15.	Heat Pipe Application with Instrument Wiring	77
16.	Variable Heat Pipe	78

THERMAL CONDUCTIVITY OF A PARTICULATE BASALT AS A FUNCTION OF DENSITY IN SIMULATED LUNAR AND MARTIAN ENVIRONMENTS

By James A. Fountain and Edward A. West

	Page
SUMMARY	81
LIST OF SYMBOLS	81
INTRODUCTION	81
THE LUNAR DENSITY	81
SAMPLE SELECTION	83
TEST PROCEDURE	83
RESULTS	84
CONCLUSIONS	87
REFERENCES	88

LIST OF TABLES

Table	Title	Page
I.	A and B Coefficients from Computer Curve Fit Program	85

CONTENTS (Concluded). . .

LIST OF ILLUSTRATIONS

Figure	Title	Page
1.	Density versus Depth in the Lunar Outermost Layer and Observational Data	82
2.	Calibration Graph of the Radiation Densimeter — Russian Luna 13	82
3.	Sample Holder	84
4.	Thermal Conductivity of Particulate Basalt as a Function of Temperature and Density	85
5.	Thermal Conductivity of Particulate Basalt as a Function of Density and Temperature	85
6.	Thermal Conductivity of Basalt as a Function of Density	86
7.	Thermal Conductivity of Particulate Basalt in a Simulated Martian Environment as a Function of Temperature and Density	86
8.	Thermal Conductivity of Basalt	87

INTRODUCTION TO THERMOPHYSICS RESEARCH AT MSFC

By

Gerhard Heller

This is the third review of thermophysics research at Marshall Space Flight Center; the last one was held during March 1966. The definition of thermophysics as stated by the American Institute of Aeronautics and Astronautics (AIAA) Thermophysics Committee is as follows:

> Study and applications of the properties and mechanisms involved in thermal energy transfer within and between solids, and between an object and its environment, particularly by radiation. Study of environmental effects on such properties and mechanisms.

In other words, thermophysics includes emissivity physics or the study of radiative properties of natural and engineering surfaces, spacecraft thermal control, definition of the space environment, its effect on thermal control surfaces, and instruments for flight experiments.

Thermophysics research at MSFC was given a strong impetus by having to meet the requirements for thermal control of EXPLORER I.

An area of thermophysics of continuous concern to Marshall is the definition of the thermal environment for present and future projects assigned to MSFC. This includes the environment of spacecraft for near-earth missions, deep-space probes, and the thermophysical properties of lunar and planetary surfaces. Our activity in measuring the radiative properties of the lunar surface and the evaluation of results by other investigators are included in this area.

Two volumes of the AIAA series "Progress in Aeronautics and Astronautics" (vol. 18 and vol. 20) have appeared during this period; both volumes contain many papers prepared by Marshall personnel and MSFC contractors. Volume 20 contains 5 papers with 9 authors and co-authors from MSFC and 10 papers by MSFC contractors. This volume can be used by those who want to become informed of the progress in thermophysics research at MSFC during the period since the last review.

There is strong participation by members of MSFC in thermophysics activities on a national scale. As MSFC becomes increasingly involved in scientific payload activities and space stations, the research activity in thermophysics has increased. Because of the challenging technology problems that have to be solved, more people are working in the area than ever before. In many cases, Marshall personnel have been responsible for the organization of numerous thermophysics and related conferences. The following are the more important ones:

- The yearly Thermophysics Specialist Conference of the AIAA.
- The yearly AIAA Aerospace Sciences Meeting with two or three sessions devoted to thermophysics papers.
- A joint NASA-DOD conference held at Wright-Patterson AFB in the summer of 1968 at which the thermal problems of all NASA and DOD space projects were reviewed.
- A regular NASA conference with participation by NASA headquarters and many other NASA centers, in addition to MSFC.

The participation in this activity is important for a number of reasons: (1) the exchange of information with others will aid in solving our problems at MSFC; (2) the participation of members of MSFC in national efforts will foster professional growth for MSFC; and (3) the activity helps in the formulation of our research tasks.

The problems covered in the previous research reviews and in the papers presented by members of MSFC at national conferences are still present. A new item is a paper on the heat pipe. Research work in this new technology was started by Marshall about two years ago. The heat pipe is based on an invention by Dr. Grover of Los Alamos. Considerable work is needed to define the research problems, and to develop the heat pipe's potential for engineering applications. One promising approach is the combination of the heat pipe concept with the heat of fusion radiator.

The assignment of the ATM-A project to MSFC has provided an additional strong impetus and requirement for thermophysics knowledge. It has also shown that MSFC should increase its effort in research toward better engineering solutions and advanced technology in this area. I am glad that an increased effort toward spacecraft oriented problems has begun; however, a further increase would be desirable.

THERMAL CONTROL COATINGS DEVELOPMENT

By

Dan Gates

SUMMARY

The material discussed in this paper concerns work accomplished under contracts NAS 8-5379[1], NAS 8-21317[2] and NAS 8-21270[3] which involve the development of various aspects of white thermal-control coatings. A general introduction to thermal control coatings is followed by a more detailed discussion of the present work with paints and pigments for space-stable thermal-control coatings of low alpha (high reflectance to sun input) and high emissivity in the infrared and low alpha/epsilon ratios.

INTRODUCTION

One of the more interesting aspects of spacecraft design is the control of the temperature of the vehicle. In relation to the exposed surface of the spacecraft, the temperature of the experiment must be maintained at approximately 23° C with a minimum of variation. This must be accomplished in an environment of 5000° C for the sun and -270° C for deep space. As shown in the simplified diagram of Figure 1 [1,2], the principal heat input is from the sun with minor reflections and emissions from nearby bodies, and internal heat is generated within the craft by electronics inefficiencies, etc. These heat sources are controlled by reflection, when pointing toward the heat source and by emission when pointing toward the near absolute zero of deep space. Whether the system is active or passive, reference is made to a surface, thus a "thermal-control" surface exists.

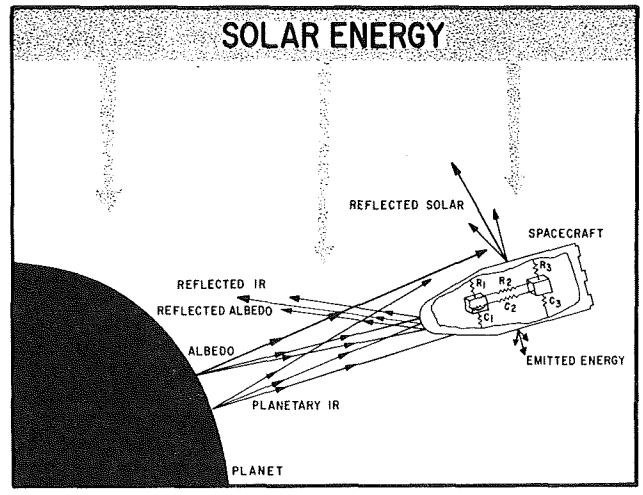

FIGURE 1. HEAT BALANCE IN A SPACECRAFT

The coatings to be considered here are the low-alpha, high-epsilon coatings as shown in Figures 2 and 3. These coatings have a low ratio of alpha to epsilon, but, importantly, this is a low ratio and a low alpha. This type of coating has high diffuse reflection [3, 4, 5] in the visible spectrum

---

1. NAS 8-5379, Development of Space-Stable Thermal-Control Coatings. IIT Research Institute Chicago, Illinois. Funded under 124-09-18-05-04-25-8-004-028-2510. G. A. Zerlaut, principal investigator.

2. NAS 8-21317, Preparation of Pigments for Space-Stable Thermal Control Coatings. The Ohio State University Research Foundation, Columbus, Ohio. Funded under 124-09-18-1200-25-9-004-028-2510. Dr. W. B. Campbell, principal investigator.

3. NAS 8-21270, Induction Plasma Calcining of Pigment Particles for Thermal Control Coatings. Stanford Research Institute, Menlo Park, California. Funded under 124-09-18-1100-25-9-004-028-2510. Dr. R. W. Bartlett, principal investigator.

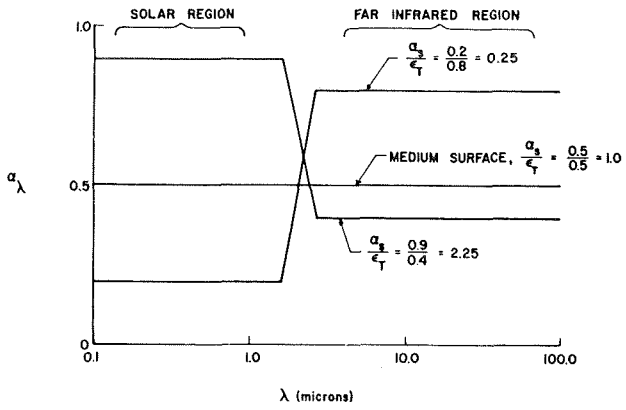

FIGURE 2. EXAMPLES OF SOME IDEAL NON-SPECTRAL SURFACES

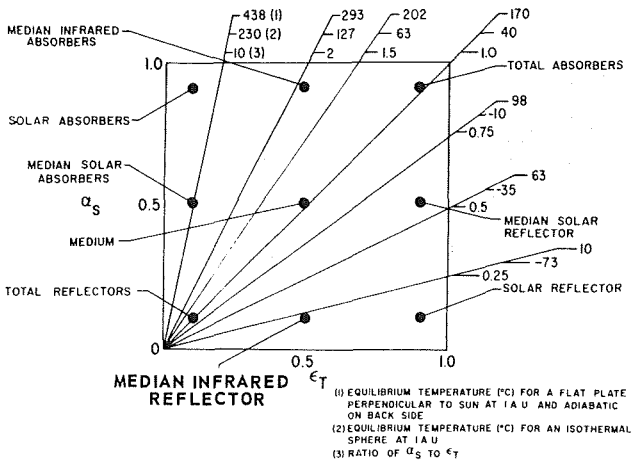

FIGURE 3. BASIC TYPES OF SURFACES

(sun input) and is highly emissive in the infrared spectrum. Thus, the coatings are white and cold-running. Figure 2, the plot of absorptance versus wavelength in microns [6,7], shows solar absorbers, medium grey surfaces, and the white surfaces of interest. The white coatings are distinguished by low absorptance in the solar region and high absorptance in the far infrared region for a low alpha/epsilon ratio. Figure 3 illustrates the same idea, but plots alpha versus epsilon [8]. A number of coatings are specifically identified by Figure 3 and the white coatings of interest are noted in the lower right corner of the diagram as "solar reflector."

The effect of the various coatings in several planetary environments is shown by the flat plate example of Figure 4 [6]. The reason for the "cold-running" term can be seen from this example, and the special properties of these particular white coatings can be compared with aluminum and black-paint surfaces. Aluminum has high reflectance over the total spectrum, and thus can dissipate very little energy in the infrared to the deep-space heat sink. Because aluminum is not a perfect reflector and does absorb some energy which it is not able to reradiate, the aluminum surfaces indeed run hotter than the surfaces painted black. A perfect mirror would constitute a perfect insulating system, i.e., no thickness, reflects all energy, etc. A perfect thermal-control system is selective in that it reflects the selected input energy spectrum and emits in all other wavelengths. When the surface is desired to run hot, as in distilling water by means of sun energy, the coating may be designed to absorb in the sun-input spectrum and reflect in all other wavelengths. The white coatings reflect in the selected wavelength (sun input) and have a high epsilon, i.e., they emit in all other wavelengths (infrared). This is the distinguishing feature of these coatings.

Coating	α_s/ϵ	Temperature		
		Mars	Earth	Venus
White paint	0.15	196°K (-77°C)	250°K (-23°C)	285°K (12°C)
Black paint	1.0	320°K (47°C)	388°K (115°C)	455°K (182°C)
Aluminum (vapor-deposited)	8.0	537°K (264°C)	660°K (387°C)	783°K (510°C)

FIGURE 4. STEADY STATE TEMPERATURES OF A FLAT PLATE FOR MARS, EARTH, AND VENUS ORBITS

To test the materials, "solar simulation" is used. Fortunately, the requirements for near-earth orbits have, as a known input, the sun's sharply defined solar spectrum. This is illustrated by the Johnson curve [9,10] (Fig. 5). The measurements that make up this curve have been refined for many years and made extensively until 1954. Therefore, it was quite startling to discover that one of the major changes recently proposed was in the maximum energy wavelength in the visible, amounting to slightly more than 3.5 percent of the energy, as shown in the proposed new Goddard curve [11,12] (Fig. 6). To duplicate our changing requirements for sun input, a source such as the B-H6 lamp, which has a spectral output as given in Figure 7, is used [13]. This lamp is indeed one of the more popular

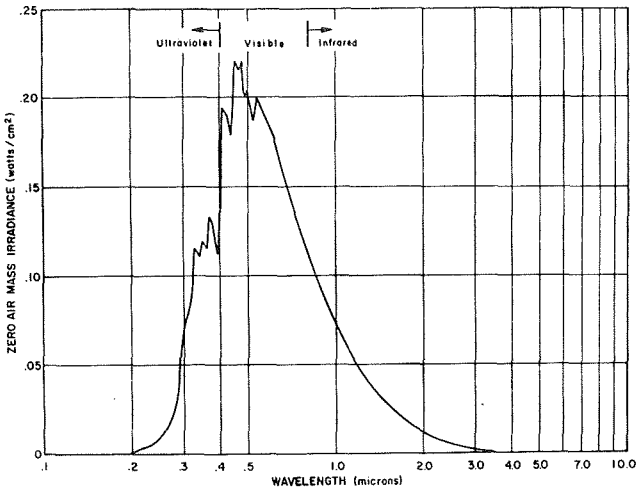

FIGURE 5. SOLAR RADIATION AFTER JOHNSON AND NASA SP-8005

and gives results from simulation testing that closely approximate coating results of certain satellites. Very close attention to detail in the simulation has led to reproducible results in such equipment as the IRIF [14, 15, 16], which both exposes samples and measures the resultant degradation from ultraviolet and proton environment while the sample is still in a vacuum. Samples can be reproduced to 1 to 5 percent reproducibility, but the accuracy of the measurement depends upon comparison with results from space experiments. Measurements of the space environment spectrum from 0.385 microns wavelength down to Lyman alpha are very spotty and of dubious reproducibility and accuracy [17, 18]. Samples made up at the same time and tested in facilities at two different locations gave essentially the same results as simulated proton exposures of 3 years and 15 years [19]. There is doubt in such results, and open loop testing of experimental coatings should be an experiment as a prime part of every satellite or probe. Allowance for coating variation, where thermal control depends on a coating, should be as lenient as possible in the thermal design, similar to the Pegasus louver system of reference to a cold surface [2].

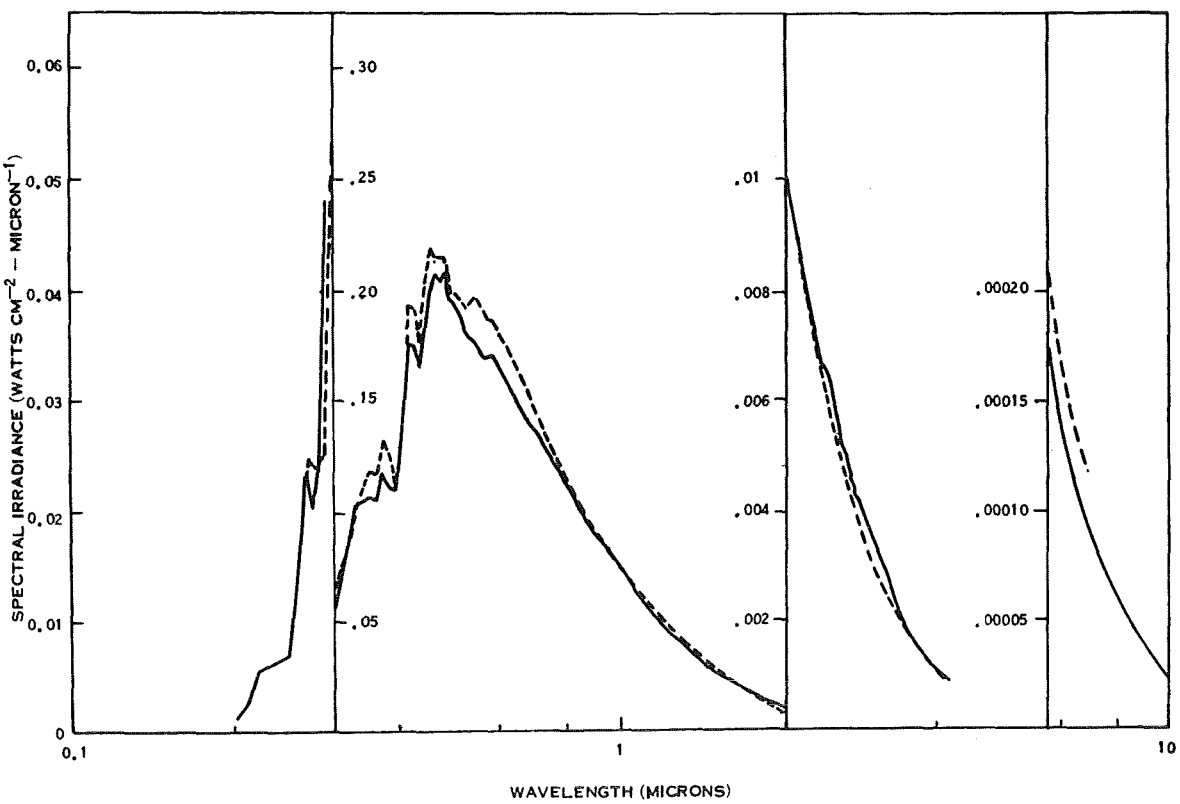

FIGURE 6. SOLAR SPECTRAL IRRADIANCE: GSFC DATA (1968) AND JOHNSON DATA (1954)

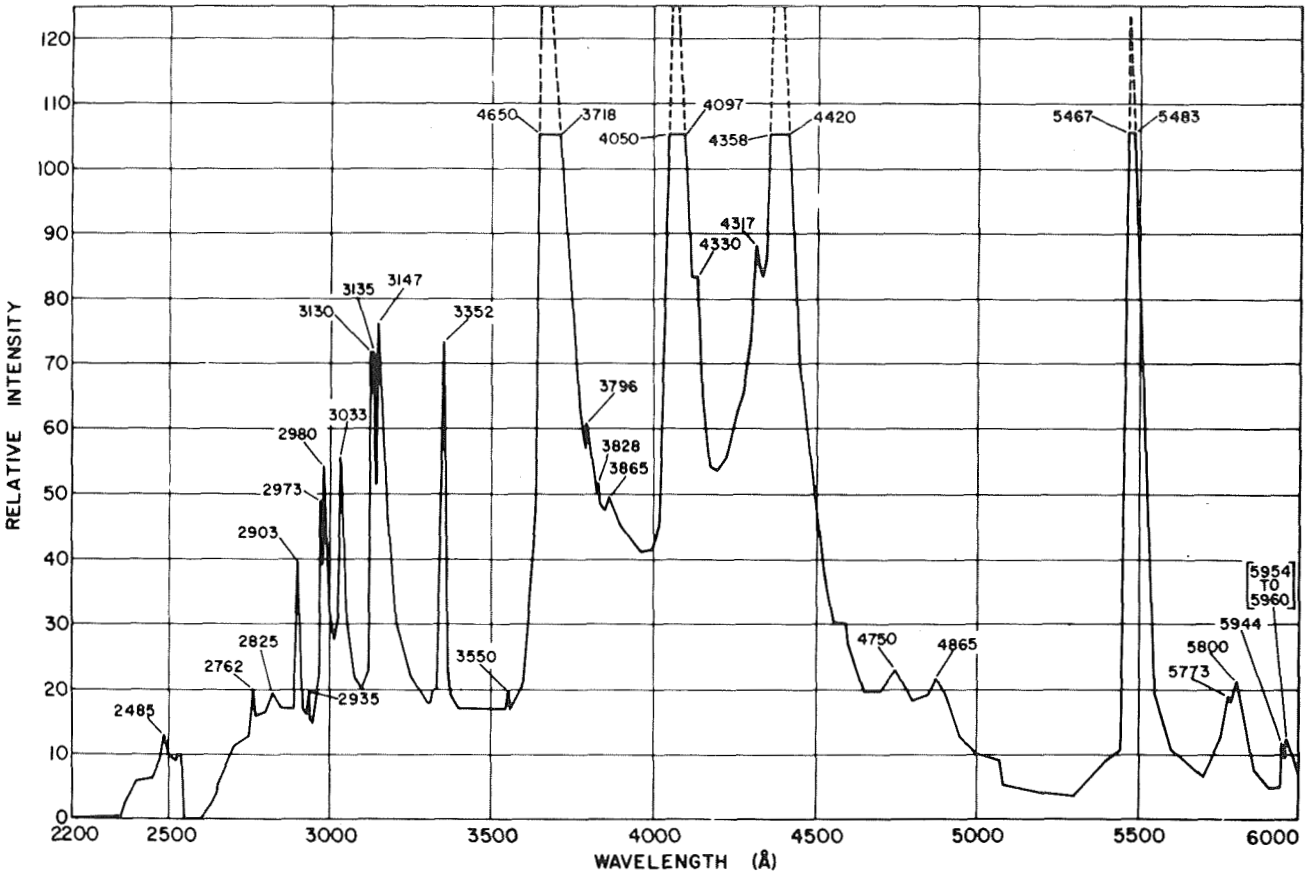

FIGURE 7. SPECTRAL INTENSITY OF B-H6 ULTRAVIOLET LAMP

This brief discussion serves to illustrate that the environment is not completely known, and the method of testing is not a very accurate reproduction of what is presumed to be required. There are still a number of difficulties inherent in "solar simulation."

There are a number of processes available for applying these coatings:

1. Flame spray
2. Fused vitreous enameling
3. Vapor deposition
4. Troweling and casting
5. Electrophoretic deposition
6. Fluidized-bed
7. Solution and flame ceramics from certain solutions
8. Pack cementation
9. Sprayed and/or brushed.

Only a limited number of these have received any wide usage in orbital spacecraft. Paint coatings, applied by spray and/or brush, of silicate, phosphate, and silicones have been widely used, and the optical solar reflector (OSR) of the vapor-deposited type has been used. The latter is used where the low emissivity and high reflectivity of the OSR can be controlled in the design [20, 21]. While it is difficult to apply on anything but a flat surface of limited area, the OSR presently makes available the lowest alpha values obtainable. Fused vitreous enamels have special advantages in that pigments are probably more stable in the enamel glass matrix than in any other medium [22, 23]. However, the complications of firing this type coating to the substrate, and the somewhat higher alpha values with the pigment loading possible (unless excessively thick coatings with an accompanying increase in weight are used) has precluded any appreciable application. The paints, of course, can be applied to any shape or size surface and, for practical engineering reasons of manufacture, are usually the first choice for consideration.

PAINTS

An inorganic coating of the paint type is Z-93 [24, 25, 26]. This coating is a standard, white thermal-control paint consisting of PS-7 potassium silicate with about 70 percent pigment volume concentration (PVC) of SP-500 (a spectrographic grade zinc oxide of high purity). An example of the silicone paints is S-13g [27, 28, 29]. This consists of a methyl-silicone vehicle such as RTV-602 or OI-650 glass resin, with about 35 percent PVC of the same zinc oxide as used in Z-93. Such coatings are applied to appropriate thickness (Fig. 8). For the silicone coating, the required thickness is about twice that shown for Z-93, because the PVC is only 35 percent as contrasted with the 70 percent possible with a silicate vehicle. Z-93 gives a coating with approximately the reflectance and stability illustrated by Figure 9. The results of using this coating on a space vehicle are shown in Figure 10.

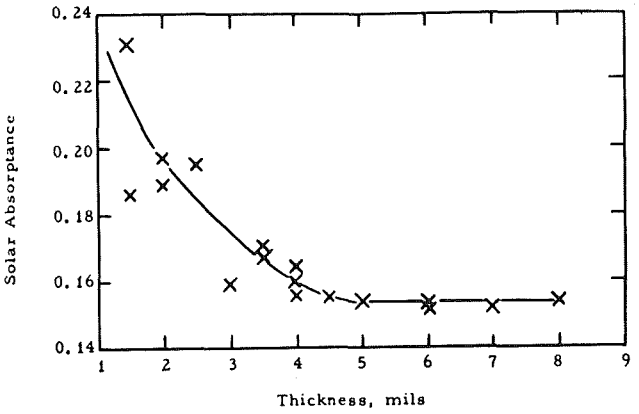

FIGURE 8. SOLAR ABSORPTANCE VERSUS THICKNESS IN ZINC OXIDE/POTASSIUM SILICATE COATINGS (Z-93)

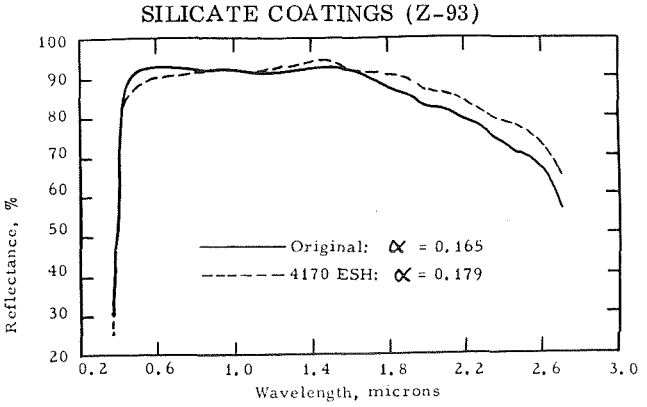

FIGURE 9. EFFECT OF 4170 ESH IN VACUUM ON SOLAR SPECTRAL REFLECTANCE OF ZINC OXIDE (CALCINED) — POTASSIUM SILICATE COATING (SAMPLE Z-93)

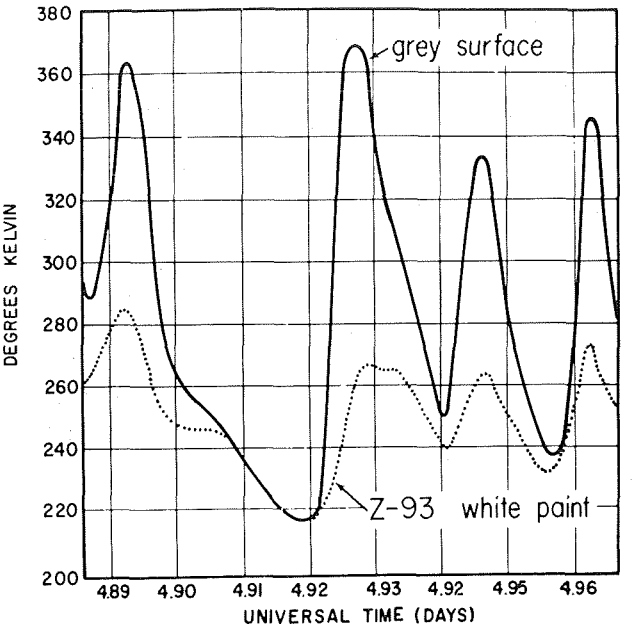

FIGURE 10. TEMPERATURE CYCLING OF PEGASUS II SURFACE (GREY AND Z-93 SURFACES)

The purpose in using this type coating is to run cold on the surface, both as a reference for heat dissipation in active control systems and to reduce the cycling of the surface temperature as the vehicle is rotated into and out of the sun input. The comparison from Pegasus II [3] of a grey-to-black surface with a white surface (Fig. 10) illustrates that we are able to accomplish our objectives. This is the type coating used on the Apollo, Surveyor, Mariner, and others. However the silicate coatings have certain problems as follow:

1. The surface is porous and difficult, if not impossible, to clean and thus requires extremely careful handling after the coating has been applied. Shown in Figure 11 at 400 X magnification is an example of the type surface exhibited by the silicate paints.

2. Adherence must be worked out for each substrate.

3. In thin coats from 0.02 to 0.07 mm the coating is extremely flexible, but between 0.08 and 0.10 mm the coating becomes considerably more frangible and is subject to thermal and mechanical shock.

4. While not soluble in the ordinary sense, the surface will retain moisture.

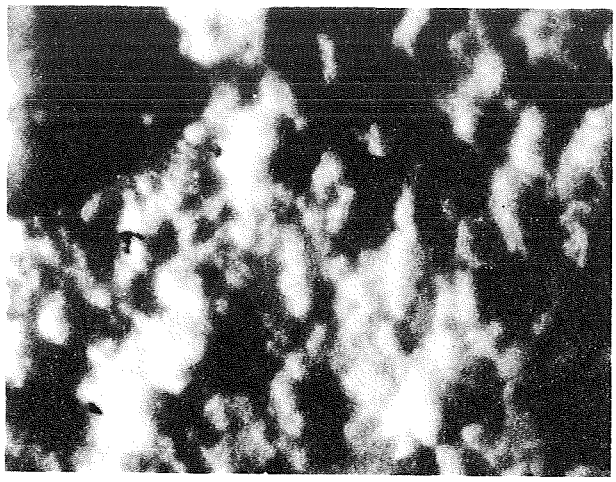

FIGURE 11. Z-93 AT 400 X MAGNIFICATION

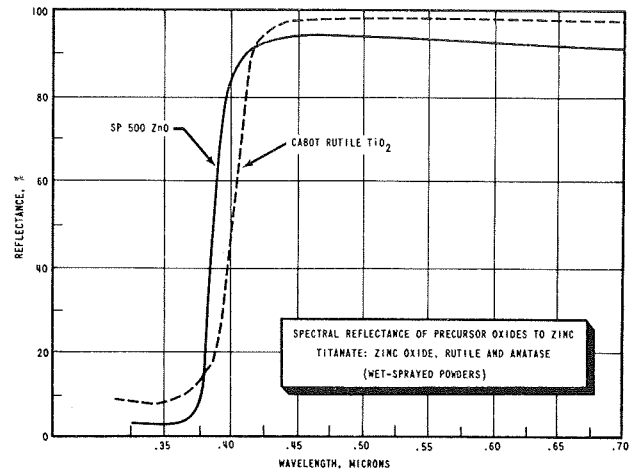

FIGURE 12. SPECTRAL REFLECTANCE OF ZnO AND TiO_2 (WET-SPRAYED POWDERS)

5. Zinc oxide has an absorption edge at about 0.385 microns wavelength, which means that there is about 9 percent of the sun input absorbed below this wavelength.

6. Repair in the field has proven to be difficult.

7. Sharp edges and corners with small radii should be avoided in the substrate design.

For several years efforts have been largely devoted to developing the elastomeric coating of the S-13g type. Because the absorption edge of the vehicles was lower than that of the zinc oxide, pigments were the first consideration for development.

PIGMENTS

The absorption edge is associated with the band gap of the pigment. Dielectric materials such as alumina have a very low absorption edge, but have never proven stable [6,13,22]. Semiconductor materials of high refractive index and close-bound ionic structures of dication and trication types were considered. One whose absorption edge is still above that of the methyl silicone vehicles (at longer wavelengths than the methyl silicones), such as OI-650 when this vehicle is cured without a catalyst, is zinc orthotitanate (Zn_2TiO_4) [30]. The two raw materials used in preparing this pigment are zinc oxide (ZnO) and anatase (TiO_2). Their optical properties are shown in Figure 12. When combined, they show a small amount of residual ZnO, off-stoichiometry, and this is evidenced optically by the shoulder at the absorption edge. This ZnO can be extracted with acetic acid, and the shoulder is eliminated as shown by the dotted curve in Figures 13, 14, and 15. By increasing the reaction temperature from 850° C (Fig. 13) to 950° C (Fig. 14), the reaction can be carried closer to completion, and a further increase to 1050° C (Fig. 15) shows further improvement in the shoulder of the curve. With acetic acid extraction, all of these are about the same optically as when sprayed in wet-powder

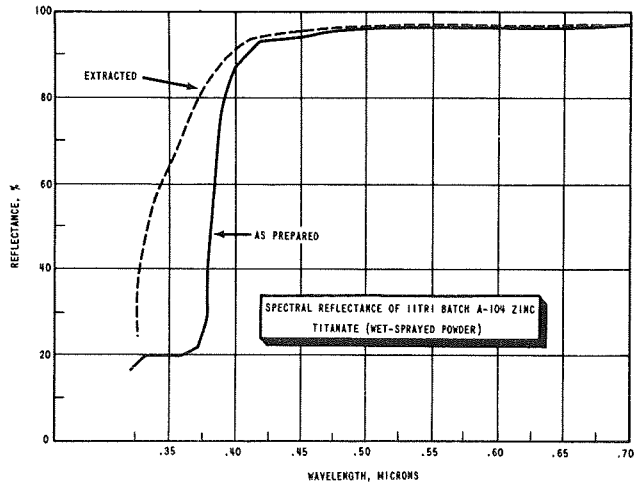

FIGURE 13. SPECTRAL REFLECTANCE OF Zn_2TiO_4 (WET-SPRAYED POWDER) — 850° C PREPARATION

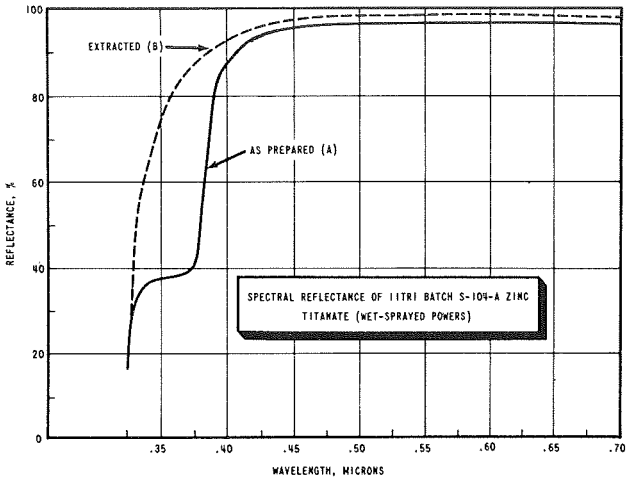

FIGURE 14. SPECTRAL REFLECTANCE OF Zn_2TiO_4 (WET-SPRAYED POWDER) — 950° C PREPARATION

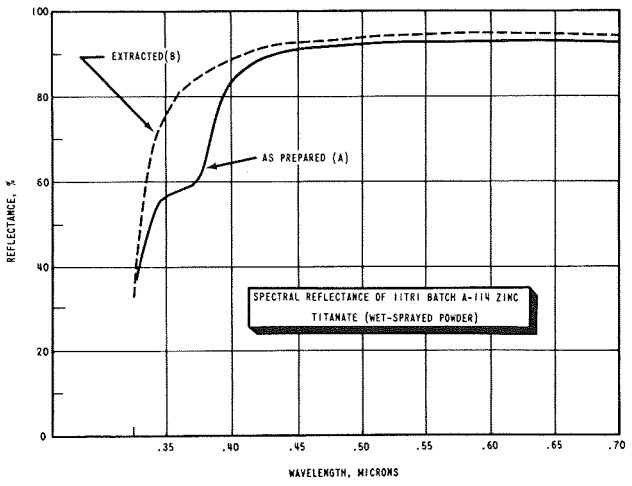

FIGURE 15. SPECTRAL REFLECTANCE OF Zn_2TiO_4 (WET-SPRAYED POWDER) — 1050° C PREPARATION

form and measured in a vacuum before radiation exposure (Figs. 13, 14, and 15). In the higher temperature products the stability is improved. However, the particle size increases, destroying the efficiency of diffuse reflection at the ultraviolet wavelengths [3, 4, 5], and the particles become very hard and difficult to reduce in size. Size reduction by grinding also destroys much of the improved stability to ultraviolet radiation. At Stanford Research Institute (SRI) [23] and Ohio State University Research Foundation (OSURF), an attempt is being made to prepare the powders at the required high temperature and in the particle size desired without further grinding. SRI is performing a final heat treatment on the suspended particles in a plasma-heated gas, and OSURF is using the homogeneous-nucleation technique to make the desired composition. Reactive encapsulation by silicate and phosphate treatments to stabilize the surface of the pigments is also being performed. The best results to date on the Zn_2TiO_4 are shown in Figures 16 and 17 [31, 14]. For practical use of these paints a long shelf life is desirable. Laboratory

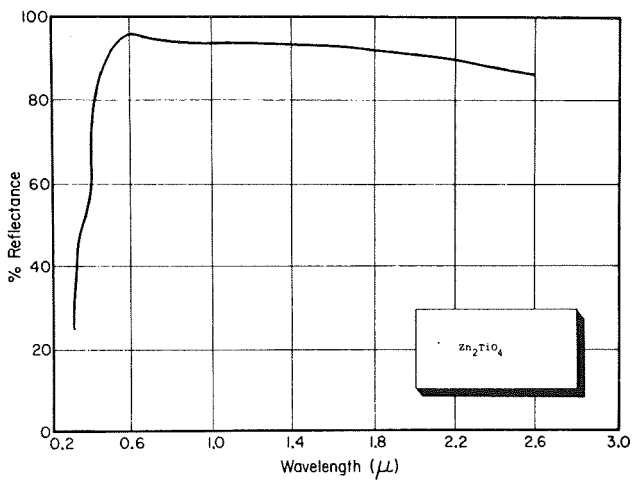

FIGURE 16. ABSOLUTE HEMISPHERICAL REFLECTANCE OF Zn_2TiO_4, EXTRACTED (WET-SPRAYED POWDER) — 1000° C PREPARATION

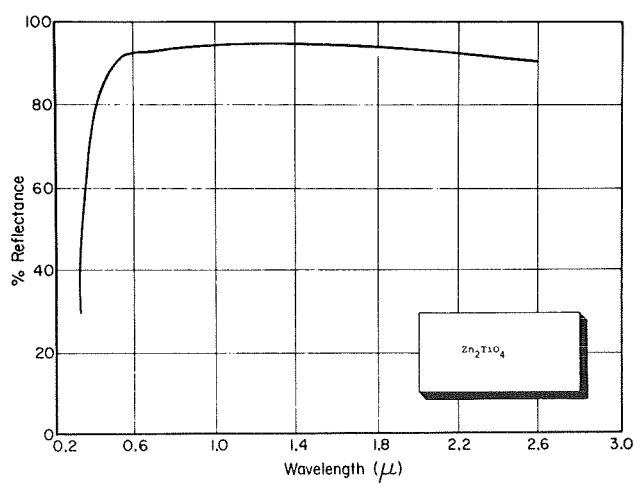

FIGURE 17. ABSOLUTE HEMISPHERICAL REFLECTANCE OF Zn_2TiO_4, EXTRACTED (WET-SPRAYED POWDER) — 1100° C PREPARATION

samples of S-13g initially had a shelf life of only hours after mixing the pigment and the RTV-602 vehicle. Shelf life with an improved methyl silicone vehicle, OI-650 glass resin, was so short that complete mixing could not be achieved before gelling occurred. This gelling is believed to be caused by the ph of the highly alkaline potassium silicate treated pigment surface. By careful attention to details such as washing the pigment thoroughly, drying and keeping the treated pigment very dry, and buffering with phosphate, shelf life has been extended to several weeks. This has been accomplished without optical damage and has been found somewhat beneficial, both in initial alpha value and in values subsequent to ultraviolet exposure. Further tests of heat-treated pigments from SRI and more effective buffering materials will eliminate the problem entirely; i.e., the mixed paints will have no change in viscosity over months of storage. The new pigments (Figs. 18, 19, and 20) [30, 31] have not caused gelling of the vehicle, and none is

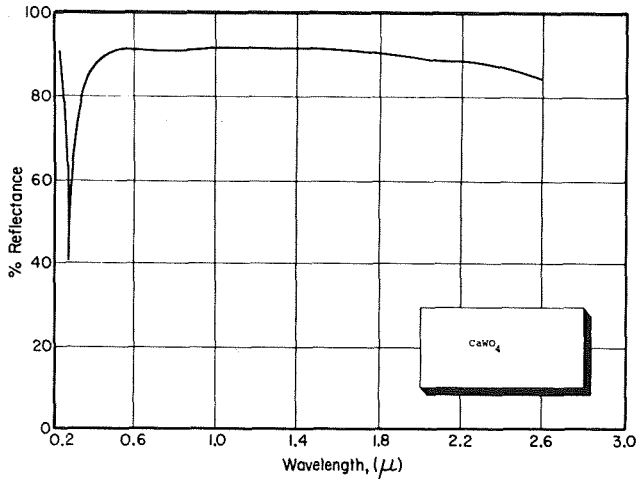

FIGURE 18. ABSOLUTE HEMISPHERICAL REFLECTANCE OF $CaWO_4$ (WET-SPRAYED POWDER)

anticipated unless potassium silicate treatment is required to improve optical stability. If silicate and/or phosphate processing appears worthwhile, the resulting pigments can be handled satisfactorily. In both calcium tungstate ($CaWO_4$) and barium tungstate ($BaWO_4$), the absorption edge has again been lowered, below that of Zn_2TiO_4 (i.e., reflects more of the ultraviolet of the sun input), which in turn was below that of the ZnO. Thus the possibility of obtaining even better initial alpha values is most promising.

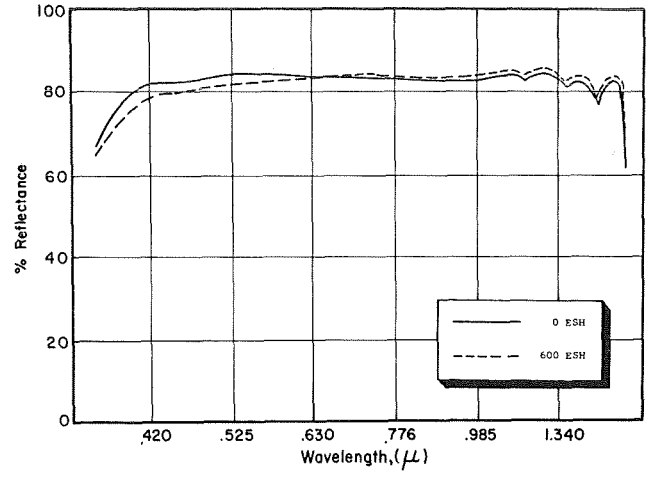

FIGURE 19. SPECTRAL REFLECTANCE OF $CaWO_4$ IN OI-650 PAINT AND WITH 600 ESH OF ULTRAVIOLET

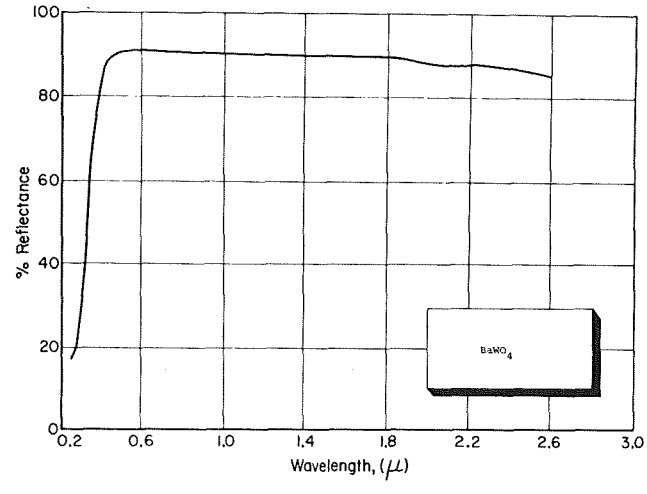

FIGURE 20. ABSOLUTE HEMISPHERICAL REFLECTANCE OF $BaWO_4$ (WET-SPRAYED POWDER)

CONCLUSIONS AND FUTURE PLANS

Coatings presently being used on spacecraft have about 88 percent reflectance for the Z-93 type and 82 percent for the S-13g type. The decrease during a year in space is up to 6 percent for a near-earth orbit. In the foreseeable future, pigments will be available for 90+ percent reflectance and in earth orbit will show a maximum 2 percent change in one year. The absorption edge of our

present pigments in the laboratory is now enough lower than ZnO that the absorption edge of the vehicles must be considered. Thinners, catalysts, and other additions must be found that do not absorb, and vehicles must be provided that retain their elastomeric properties in a space environment. Resistance (insensibility) to both thermal and mechanical shock and good adherence to a variety of substrates are also necessary qualities. Epsilon values of reradiation in the infrared must be kept in the 85+ percent range for best heat dissipation. If doping is practical, it must be done with materials that do not cause initial discoloration. Otherwise, the initial loss in alpha value because of the dopant will be such that for any normal length of time the degradation of the undoped material still gives an alpha value better than that of the stable but lower initial alpha of doped pigment. Shelf life, as exhibited by the change in viscosity with time of storage, has been improved from initial values of hours in S-13g to three or more weeks and should be extended to several months as testing of present laboratory samples is completed. However, as in all the above, the major hurdle is open-loop test samples in the space environment. These are necessary to confirm and maintain assurance that the "Space-Simulation" testing has within its parameters those necessary to give results similar to flight experiment results. It is important that space radiation damage be simulated rather than attempt to have some nebulous exact "space environment" in our environmental test program.

REFERENCES

1. Heller, G.: Thermal Problems of Satellites. Published in Materials in Space Environment. Proceedings of the Fifth Sagamore Ordnance Materials Research Conference, Sagamore Conference Center, Racquette Lake, New York, September 16-19, 1958.

2. Bannister, T. C.: Pegasus Thermal Design. NASA TMX-53300, 1965.

3. Jaenicke, W.: Zeit. Electrochemie 60, No. 2, 163 (1956).

4. Van de Hulst, H. C.: Light Scattering by Small Particles. Wiley, 1957.

5. a Zerlaut, G. A.; and Kaye, B. H.: Summary of Investigations of Light Scattering in Highly Reflecting Pigmented Coatings. Volume I, NASA CR-844, 1967.

   b. Zerlaut, G. A.; Katz, S.; Raziunas, V.; and Jackson, M.: Classical Investigations; Theoretical and Experimental. Volume II, MSFC NASA CR-61166, 1967.

   c. Kaye, B. H.; Jackson, M.; and Zerlaut, G. A.: Monte Carlo and Other Statistical Investigations. Volume III, MSFC NASA CR-61167, 1967.

6. Zerlaut, G. A.; Carroll, W. F.; and Gates, D. W.: Spacecraft Temperature-Control Coatings: Selection, Utilization and Problems Related to the Space Environment. Proceedings XVIth, International Astronautical Federation, Springer-Verlag Publishers, Warsaw, 1966.

7. Zerlaut, G. A.: Utilization of Pigmented Coatings for the Control of Equilibrium Skin Temperature of Space Vehicles. Aerospace Finishing Symposium (Proceedings), Fort Worth, Texas, December 8-9, 1959.

8. Snoddy, W. C.; and Miller, E.: Areas of Research on Surfaces for Thermal Control, Symposium on Thermal Radiation of Solids (S. Katzoff, Ed.). NASA SP-55, Washington, D.C., 1965.

9. Johnson, F. S.: The Solar Constant. Journal of Meteorology, Volume II, No. 6, December 1954.

10. Solar Electromagnetic Radiation. NASA SP-8005, Washington, D.C., June 1965.

REFERENCES (Continued)

11. Kaplin, J.: Near-Earth Electromagnetic Radiation Environment. Report No. 4, Space Physics Laboratory, General Electric. Under Contract No. NAS 8-21420, MSFC, W. T. Roberts, contract technical monitor, December 1968.

12. NASA-GSFC: The Solar Constant and the Solar Spectrum Measured from a Research Aircraft at 38,000 Feet. NASA TMX-322 68-304, 1968.

13. Carroll, W. F.: Development of Stable Temperature Control Surfaces for Spacecraft. Jet Propulsion Laboratory, Report No. 33-340, 20 November 1962.

14. Zerlaut, G. A.; Noble, G.; and Rogers, F. O.: Development of Space-Stable Thermal-Control Coatings. Interim Report No. U6002-55, MSFC Contract No. NAS8-5379, September 1967.

15. Zerlaut, G. A.; and Courtney, W. J.: Space-Simulation Facility for In-Situ Reflectance. Thermophysics of Spacecraft and Planetary Bodies (G. Heller, Ed.), Academic Press, 1967.

16. Zerlaut, G. A.; and Roger, F. O.: The Behavior of Several White Pigments as Determined by In-Situ Reflectance Measurements of Irradiated Specimens. Proceedings of the Joint Air Force-NASA Thermal Control Working Group. AFML-TR-68-198, Air Force Materials Laboratory, Wright-Patterson Air Force Base, Ohio, 1968.

17. Gillette, R. B.; Brown, R. R.; Seiler, R. F.; and Sheldon, W. R.: Effect of Protons and Alpha-Particles on the Thermal Properties of Spacecraft and Solar-Concentrator Coatings. Thermophysics and Temperature Control of Spacecraft and Entry Vehicles (G. Heller, Ed.), Academic Press, 1966.

18. Breuch, R. A.: Exploratory Trapped-Particle and Trapped-Particle-Plus-Ultraviolet Effects on the Optical Properties of Spacecraft Thermal Control Coatings. Thermophysics and Temperature Control of Spacecraft and Entry Vehicles (G. Heller, Ed.), Academic Press, 1966.

19. Wehner, G. K.: Solar Wind Bombardment of a Surface in Space. Symposium on Thermal Radiation of Solids (S. Katzoff, Ed.), NASA SP-55, Washington, D.C., 1965.

20. Greenberg, S. A.; Vance, D. A.; and Streed, E. R.: Low Solar Absorptance Surfaces with Controlled Emittance: A Second Generation of Thermal Control Coatings. Thermophysics of Spacecraft and Planetary Bodies (G. Heller, Ed.), Academic Press, 1967.

21. Breuch, R. A.; and Greenberg, S. A.: Recent Coating Developments and Exposure Parameters. Proceedings of the Joint Air Force-NASA Thermal Control Working Group. AFML-TR-68-198, Air Force Materials Laboratory, Wright-Patterson Air Force Base, Ohio, 1968.

22. Zerlaut, G. A.; Harada, Y.; and Tompkins, E. H.: Ultraviolet Irradiation of White Spacecraft Coatings in Vacuum. Symposium on Thermal Radiation of Solids (S. Katzoff, Ed.), NASA SP-55, Washington, D.C., 1965.

23. Zerlaut, G. A.; Gilligan, J. E.; and Harada, Y.: Stable White Coatings. IIT Research Institute Report IITRI-C6027-16 (Interim Technical Progress Report). Under Jet Propulsion Laboratory Task-959746, W. F. Carroll, technical monitor (NAS 7-100) Pasadena, California, 30 June 1965.

24. Gilligan, J. E.; Siebert, M. E.; and Greening, T. A.: Passive Thermal Control Coatings. Presented at the Seventh Meeting of the Refractory Composites Working Group, Palo Alto, California. Published in RTD-TDR-63-4131, Wright-Patterson Air Force Base, Ohio, 1963.

REFERENCES (Concluded)

25. Zerlaut, G. A.; and Harada, Y.: Stable White Coatings. Final IIT Research Institute Report C207-25 on task 950111 (subcontract under NAS 7-100), W. F. Carroll, technical monitor for Jet Propulsion Laboratory, Pasadena, California, 1963.

26. Streed, E. R.: An Experimental Study of the Combined Space Environmental Effects on a Zinc-Oxide/Potassium Silicate Coating. Thermophysics of Spacecraft and Planetary Bodies, Academic Press, 1967.

27. Zerlaut, G. A.; and Rogers, F. O.: Development of Space-Stable Thermal-Control Coatings. Interim Report No. U6002-47, Under MSFC Contract NAS8-5379, November 1966.

28. Zerlaut, G. A.; and Rubin, G. A.: Development of Space-Stable Thermal-Control Coatings. Interim Report No. U6002-36, MSFC Contract No. NAS8-5379, February 1966.

29. Zerlaut, G. A.; and Rogers, F. O.: Development of S-13G-Type Coatings as Engineering Materials, Final Report. IIT Research Institute task No. 951737 under Jet Propulsion Laboratories Contract No. NAS7-100, W. F. Carroll contract monitor, March 1969.

30. Zerlaut, G. A.; Marcour, M.; and Noble, G.: Development of Space-Stable Thermal-Control Coatings. Interim Report No. U6002-69, MSFC Contract No. NAS8-5379, October 1968.

31. Zerlaut, G. A.; and Ashford, N.: Development of Space-Stable Thermal-Control Coatings. Interim Report No. U6002-73, MSFC Contract No. NAS8-5379, January 1969.

BIBLIOGRAPHY

Bartlett, W. R.: Induction Plasma Calcining of Pigment Particles for Thermal Control Coatings. Final report for February to August 1968, MSFC Contract No. NAS 8-21270, August 1968.

Measurement of Thermal Radiation Properties of Solids. NASA SP-31 (Richmond, Ed.) Washington, D.C., 1963.

Neel, C. B.: Research on the Stability of Thermal-Control Coatings for Spacecraft. Paper presented at the Fifth International Symposium on Space Technology and Science in Tokyo, Japan. Published in the proceedings, 1964.

Proceedings of the Fifth Sagamore Ordnance Materials Research Conference, Materials in the Space Environment (W. Steurer, Ed.). Syracuse University Research Institute, Syracuse, New York and The Office of Ordnance Research of U.S. Army, Durham, North Carolina. Held at Sagamore Conference Center, Racquette Lake, New York, September 1958.

Proceedings of the Joint Air Force-NASA Thermal Control Working Group (Johnson and Boebel, Eds.). AFML-TR-68-198, Wright-Patterson Air Force Base, Ohio, 1968.

Symposium on Thermal Radiation of Solids. NASA SP-55 or Air Force ML-TDR-64-159 (Katzoff, Ed.), Washington, D.C. or Wright-Patterson Air Force Base, Ohio, 1965.

Thermophysics and Temperature Control of Spacecraft and Entry Vehicles (G. Heller, Ed.). Academic Press, 1966.

Thermophysics of Spacecraft and Planetary Bodies. (G. Heller, Ed.). Academic Press, 1967.

STUDIES RELATED TO THE DEVELOPMENT OF COLOR CENTERS IN ZINC OXIDE

By

G. M. Arnett and R. L. Kroes

SUMMARY

Zinc oxide (ZnO) samples of single crystals, powders, and thin films were studied using a variety of experimental techniques in order to reach an understanding of the degradation mechanism observed in ZnO pigment thermal control coatings when subjected to ultraviolet irradiation under vacuum. The techniques used were electron paramagnetic resonance (EPR), photo conductivity, photo-Hall effect, and optical properties including luminescence. The measurements made were correlated and evaluated in terms of the degradation model discussed in this paper.

INTRODUCTION

ZnO has been used extensively as a paint pigment for the thermal control coating of spacecrafts. However, when subjected to ultraviolet irradiation in a space environment, the ZnO coating degrades and absorbs a higher percentage of incident solar energy. To understand this degradation mechanism, Lockheed Missiles and Space Co. [1] proposed the following model.

DISCUSSION OF DEGRADATION MODEL AND MEASUREMENTS USED IN INVESTIGATING THE MODEL

Under normal conditions, zinc oxide is known to have chemisorbed oxygen on the surface. This causes the electronic energy bands at the surface to bend upward. Irradiation with ultraviolet light produces electron-hole pairs. Trapping these photo-produced holes neutralizes the surface oxygen and allows it to be desorbed, thereby reducing the degree of band bending. This increases the concentration of defect centers and the population of these centers at the surface. Photo-desorption of oxygen increases the concentration of zinc, which ultimately defuses in the bulk of the sample and causes lattice strain. This may lead to localized changes in the band gap. The increase in the concentration and population of the oxygen-ion vacancies on the surface and the resultant increase in the zinc interstitial defects have been used to explain the higher absorption of solar energy for the infrared and visible regions in the degraded sample.

To verify the above model, some optical, magnetic, and electrical measurements are being conducted on ZnO in various forms; e.g., powders, thin film, and single crystals.

The creation of oxygen-ion vacancy by photo-desorption of oxygen may result in the creation of a paramagnetic defect which should be observable by electron spin resonance and magnetic susceptibility techniques. The creation of significant density of conduction electrons or holes can also be observed by EPR techniques.

The effects of surface oxygen could be more clearly understood by measurements on thin films where surface phenomena are more pronounced. If ultraviolet radiation decreases the band bending at the surface, then this could be displayed by an increase in the electron concentration in ZnO samples during irradiation.

It is possible to verify the increase in concentration of zinc interstitials, if they exist, through optical measurements. Moreover, optical measurements on thin films in the infrared region will show whether or not this is a surface phenomenon.

In case the phenomenon taking place in ZnO upon irradiation is an aggregate of surface and bulk effects, then it is possible to investigate the nature of the defect centers by luminescence and bulk electrical and magnetic properties.

There are several ways in which to associate the luminescence study with the proposed Lockheed model. This model predicts that ultraviolet interaction with the sample in a vacuum produces a

zinc-rich sample. It also predicts the production of paramagnetic defect centers. Zinc rich powder samples have been produced by subjecting the samples to a reduction process. This process removes oxygen from the sample and leaves it zinc rich. These samples then exhibit photo-luminescence that was not present before the reduction process. The exact nature of the defect centers responsible for the luminescence is not yet known. However, there are plans to compare the EPR signal already observed in vacuum-irradiated ZnO to any EPR signal that may be observed in the luminescence samples, particularly to see if they are the same type of center.

RESULTS AND CONCLUSIONS

The A-H6 lamp, the monochromators, the sample chamber, and the photomultiplier detector can be seen in the luminescence facility shown in Figure 1.

Figure 2 shows the photoluminescence spectrum of activated ZnO. This is a powder sample which had been heated in a reducing atmosphere of carbon monoxide at 1000° C. This reduction process produced a zinc rich sample by removing some of the oxygen. The luminescence in this

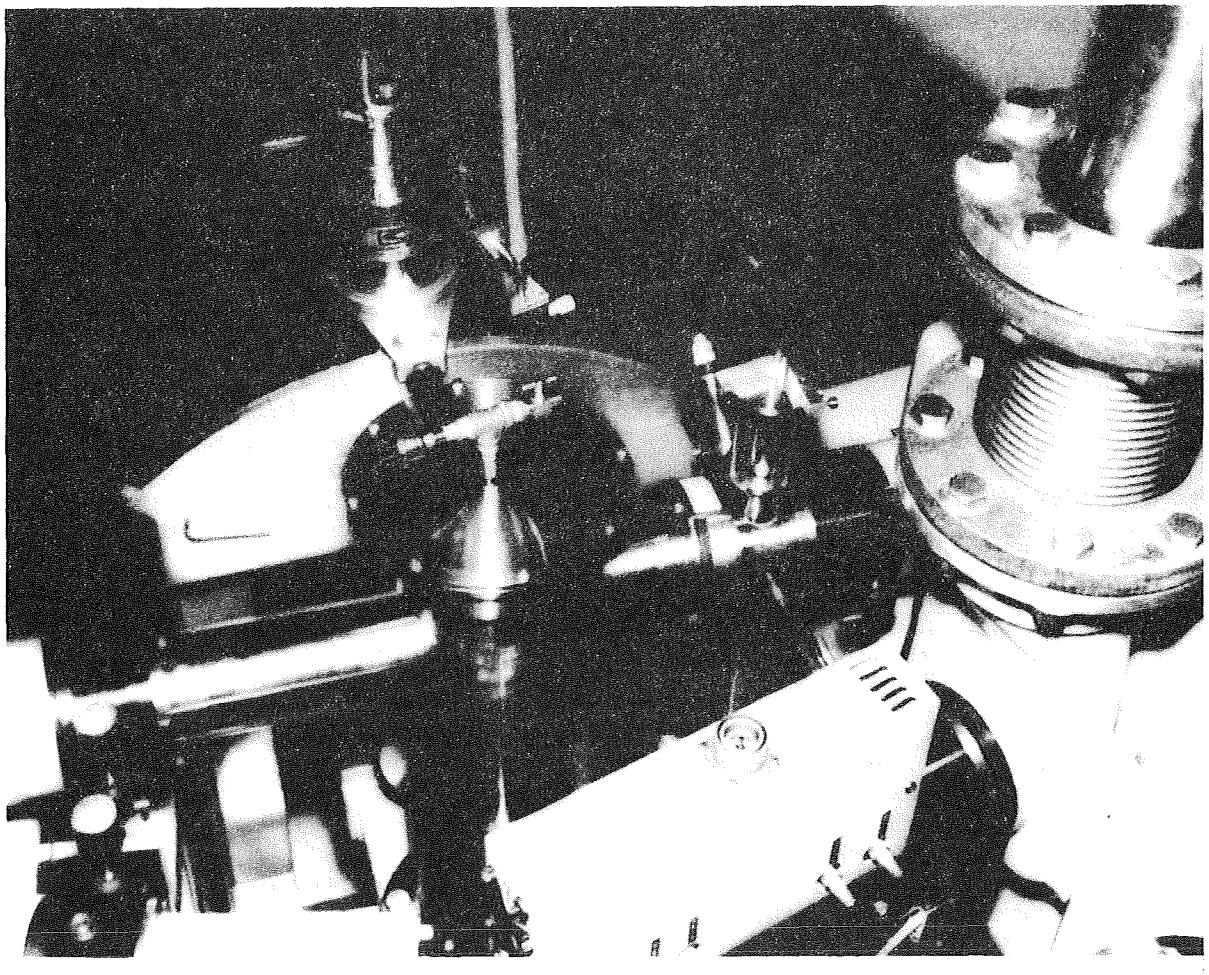

FIGURE 1. LUMINESCENCE FACILITY

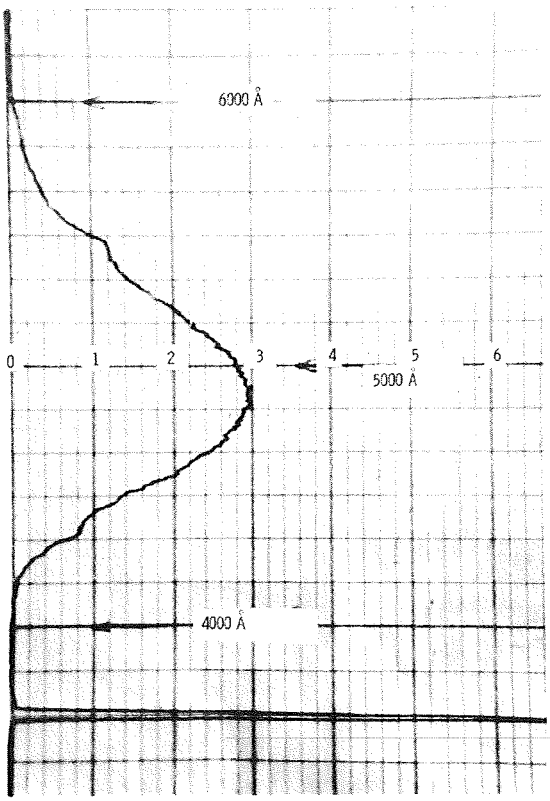

FIGURE 2. PHOTOLUMINESCENCE SPECTRUM FROM ACTIVATED ZnO

sample was produced by excitation with ultraviolet light having a wavelength of 3660Å, and produces a broad-band green luminescence.

Figure 3 shows the intensity of luminescence produced by excitation with wavelengths from 3000Å to 4000Å from an A-H6 lamp. The main feature to note is the very intense luminescence produced when activated ZnO is irradiated with near band-gap energy.

As can be seen from Figure 4, the electron spin resonance (ESR) signal consists of one absorption line with no structure [2]. The spectroscopic splitting factor for the sample irradiated with radiation having a wavelength between 0.2 micron and 0.4 micron is equal to 1.9342, and that for the sample irradiated with a light of wavelength 0.8 micron is 1.9193. Both spectra have the same line width of 4.8 gauss. Theoretical analyses of the absorption curves for both Lorentzian and Gaussian line shapes are made, and these are plotted against the experimentally observed line shape. There is a one-to-one correspondence between the theoretical Lorentzian and the experimental line shape as can be seen in Figure 5. Although there appears to be a one-to-one correspondence between the theoretical Gaussian and the experimental line shape near the absorption peak, there is a considerable deviation at the tail of the absorption curve.

Figure 6 shows the ESR spectra from a mechanically damaged ZnO sample. Two distinct degradations

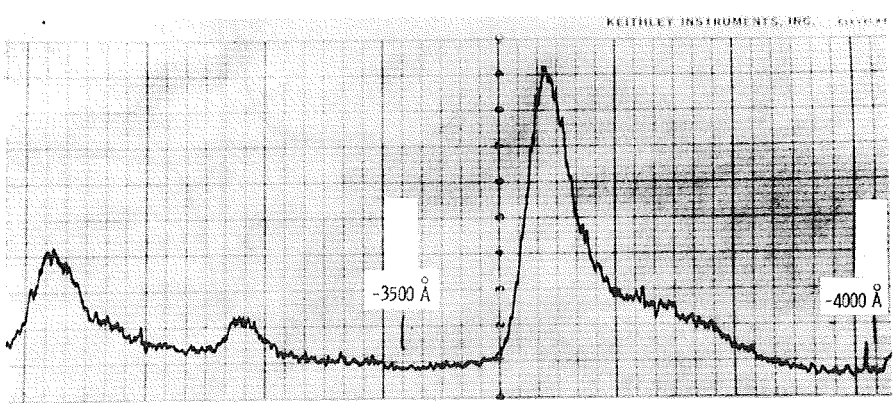

FIGURE 3. LUMINESCENCE MAXIMUM FOR EXCITATION WAVELENGTHS 3000Å TO 4000Å FROM ACTIVATED ZnO

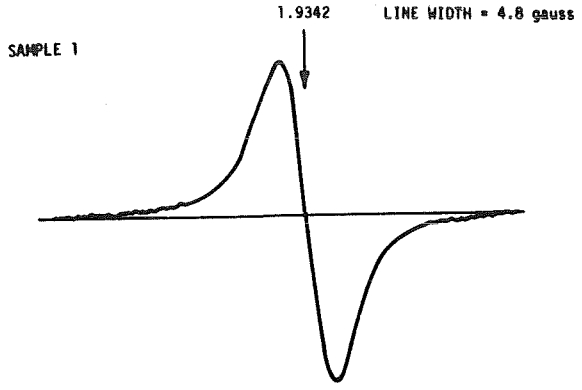

FIGURE 4a. ESR FROM SAMPLE RADIATED WITH 0.2 TO 0.4 μ WAVELENGTH RADIATION USING A-H6 HIGH PRESSURE MERCURY LAMP

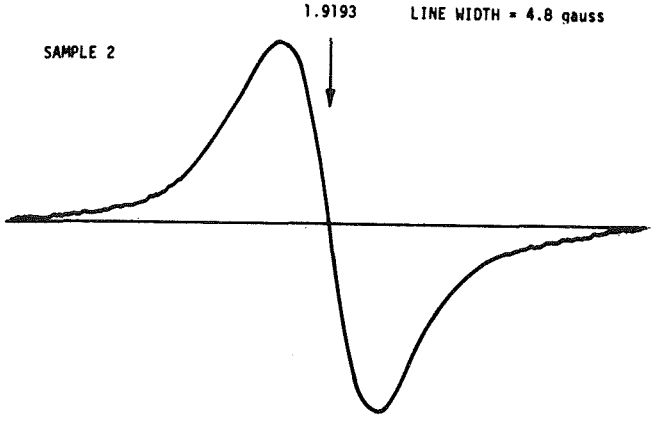

FIGURE 4b. ESR FROM SAMPLE RADIATED WITH 0.8 μ WAVELENGTH RADIATION

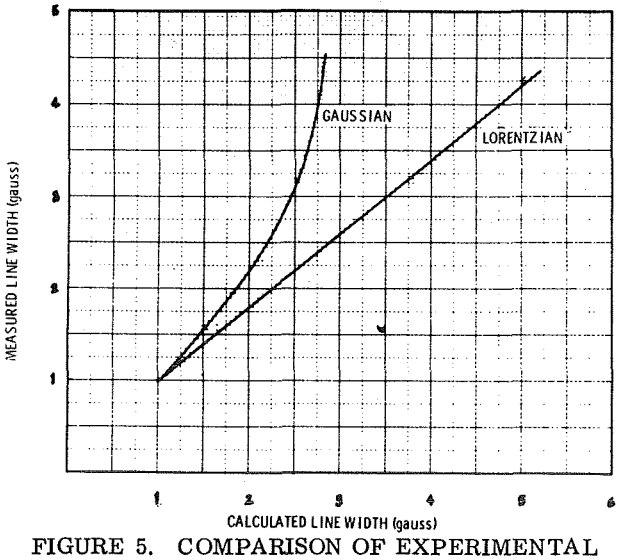

FIGURE 5. COMPARISON OF EXPERIMENTAL AND THEORETICAL LINE SHAPES

appear to be taking place in this sample. The signal with the structure disappears when the sample is annealed at 600° C in the presence of oxygen. However, the second signal remains, and it has a g-value very close to the one which has been ultravioletly radiated.

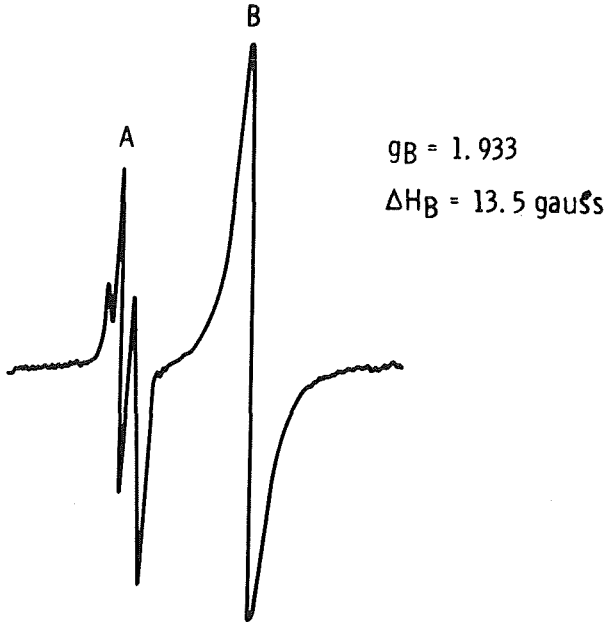

FIGURE 6a. ESR SPECTRA OF A MECHANICALLY DAMAGED SAMPLE

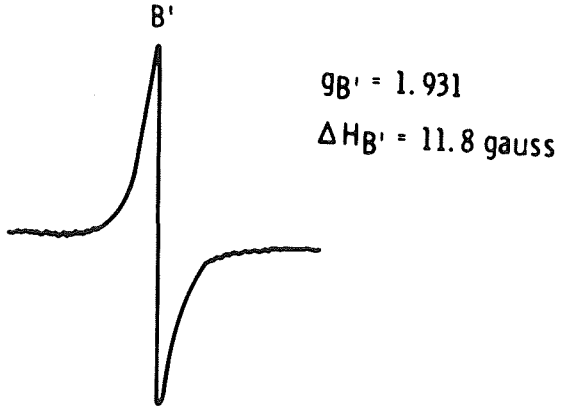

FIGURE 6b. ANNEALING EFFECT ON THE MECHANICALLY DAMAGED SAMPLE

From the measurements, it appears that the spin resonance observed is probably not caused by holes. The orbital of the paramagnetic defect

appears not to be localized on surrounding zinc ions. It is also possible that there is inhomogeneous broadening of the resonance line. The spin-orbit coupling also has some effect in determining the exact character of the resonance.

Without further study of the temperature variation of the spectroscopic splitting factor, the effect of radiation of varying energy, etc., it is not possible to draw more conclusions about the degradation mechanism.

REFERENCES

1. Sklensky, A. F.; MacMillan, H. F.; and Greenberg, S. A.: Solar-Radiation-Induced Damage to Optical Properties of ZnO-Type Pigments. Contract NAS8-18114, Technical Summary Report, Lockheed Missiles and Space Company, Palo Alto, California, February 1968.

2. Mookherji, T.: Electron Paramagnetic Resonance Study of Ultraviolet Irradiated ZnO Single Crystals and Powders. Contract NAS8-20166, Brown Engineering Co., Huntsville, Alabama.

EFFECT OF SOLAR WIND ON THERMAL CONTROL COATINGS

By

Donald R. Wilkes

INTRODUCTION

Thermal-control coatings are used as passive thermal-control systems of spacecraft. If the optical properties of these coatings are changed, this will upset the temperature balance of the vehicle, causing it to become too hot or too cold. When this vehicle is used for a high-earth orbit or for an interplanetary mission, the thermal-control surfaces are subjected to solar-wind particulate radiation in addition to the environmental conditions found in low-earth orbit. This is because the solar wind does not penetrate the Van Allen belts and reach the low-orbit satellites.

High earth-orbit satellites or interplanetary probes have shown much greater damage to coatings than did low earth-orbit satellites [1]. Generally, this difference has been attributed to solar wind damage.

It has also been shown that particulate radiation of the same mass and energy can damage thermal-control coatings. If this damage can be experimentally determined on a particular coating, this information can be used to overdesign the thermal control system to allow for this change in the properties of the coating. This information can also be used to improve the existing coatings.

This paper is a brief summary of work done to simulate the solar wind radiation and to determine its effect on thermal control coatings.

SOLAR WIND SIMULATION

The solar wind is a plasma consisting of protons, electrons, alpha particles, and other heavier nuclei drifting outward from the general direction of the sun. Each of the constituents in the solar wind has the same velocity distribution [2]. This plasma has been measured by several satellites such as the Mariner II Venus probe.

Table I shows measurements of the proton and alpha particle fluxes and velocities made by the Mariner II Venus probe [2]. The fluxes of the heavier nuclei are very small compared to the proton and alpha fluxes and are not generally considered to cause significant damage. Electrons in the solar wind are also considered to be unimportant since they have a very low energy (~1 eV). Therefore, to simulate the solar wind, an ion generator is required and it must be capable of emitting very low fluxes of both protons and alpha particles with velocities of from 250 to 1000 km/sec. Figure 1 shows an ion generator specifically designed to accomplish this requirement.

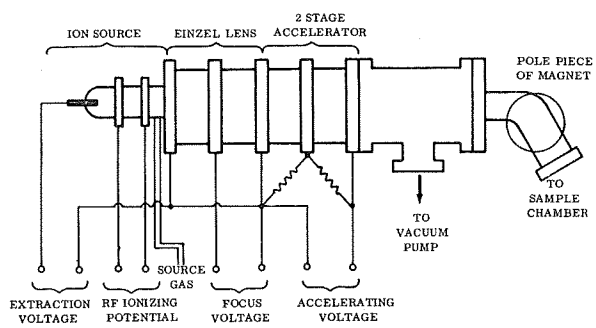

FIGURE 1. ION GENERATOR FOR SOLAR WIND SIMULATION

Hydrogen and helium gases are ionized to obtain protons and alpha particles, respectively. These ions are then extracted and accelerated down the tube toward the sample under test. Since the ionized gas has some impurities, an analyzing magnet is used to choose only the ions desired. After the ions are generated, they enter the sample chamber and bombard the selected sample.

ENVIRONMENTAL TESTING

An in situ test chamber having a five sample capacity is shown in Figure 2. Each of these samples

TABLE I. PROTON AND ALPHA PARTICLE CONTENT IN THE SOLAR WIND

Particle	Flux (cm^{-2} sec^{-1})	Velocity (km/sec)
Proton (average solar)	2×10^8	600
Proton (solar storm)	2×10^9	1000
Alpha (average solar)	3×10^7	600
Alpha (solar storm)	3×10^8	1000

can be irradiated and measured using a scanning reflectometer without breaking the vacuum (in situ). This is important since it has been discovered that part, or all of the type surface damage caused by solar wind as well as solar ultraviolet will bleach when oxygen is admitted to the surface. Figure 3 shows the reflectance of a Z-93 sample before and after a year's exposure to solar wind protons.

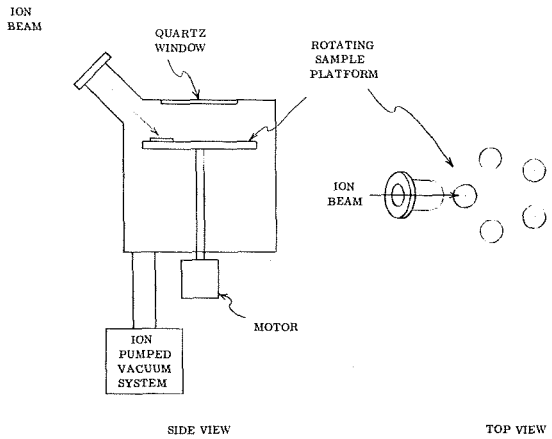

FIGURE 2. IN SITU CHAMBER

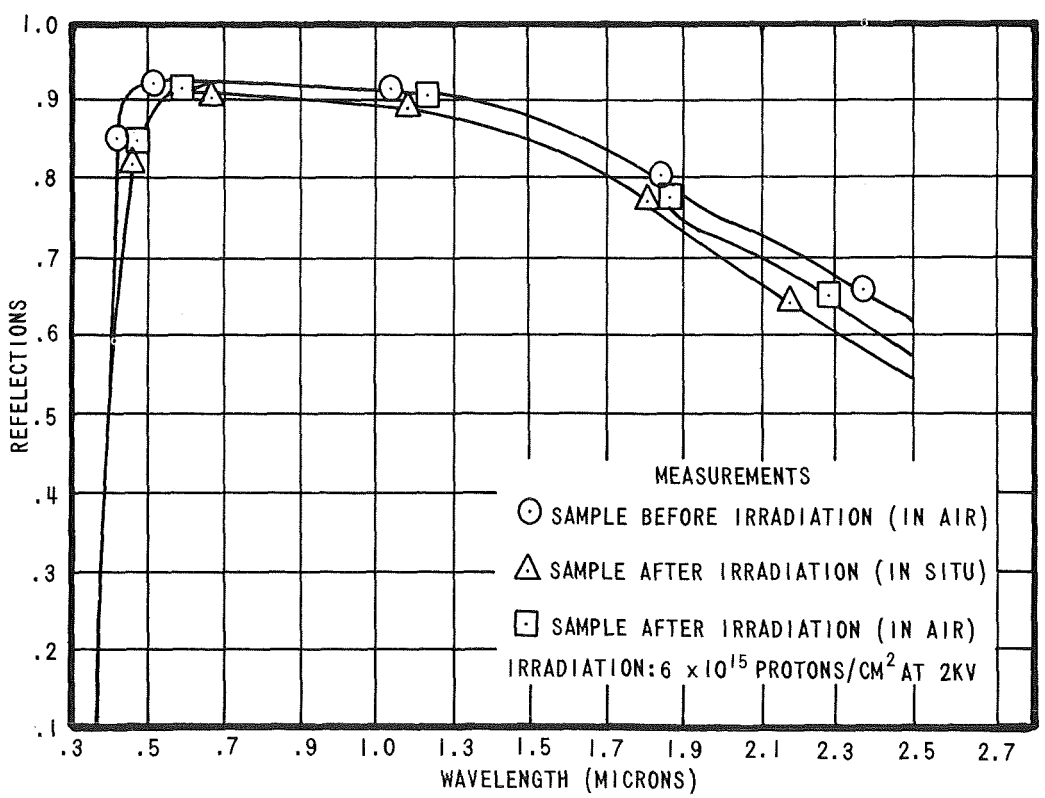

FIGURE 3. SOLAR WIND EFFECTS ON Z-93

Upon returning to the atmosphere, this damage to the Z-93 sample will partially bleach. This is an effect similar to that we have observed with solar ultraviolet damage to thermal-control coatings [3].

Simulated solar-wind damage to standard coatings has not been as high as had been indicated by the high-altitude satellites or interplanetary probes.

Recent data have indicated that there is possibly enough oxygen in low-earth orbit to cause some bleaching of ultraviolet damage to coatings. This might account for part of the differences in measured damage in high and low orbits [1].

This work is continuing and consists of (1) varying the parameters of the solar wind to investigate different total fluxes and energies to determine if there is a damage threshold, and (2) investigating different flux rates to determine if the reciprocity relation is valid. Also, the combined environment of simulated solar wind and simulated solar ultraviolet will be used to determine what synergistic effects on thermal-control coatings occur with this combination.

The damage mechanism of this particulate-radiation interaction with surfaces will be investigated using solid-state techniques such as electron-paramagnetic resonance, ultraviolet luminescence, and the Hall effect.

REFERENCES

1. Miller, E. R.; Wilkes, D. R.; and Zwiener, J. M.: Space Simulation for Thermal Control Surfaces Research. Proceedings of ASTM Meeting, Atlanta, Georgia, September 29 - October 4, 1968.

2. Jorgenson, G. V.: Effects of Simulated Solar-Wind Bombardment on Spacecraft Thermal Control Surfaces. Thermophysics and Temperature Control of Spacecraft and Entry Vehicles, AIAA, vol. 18, G. Heller, ed., 1965.

3. Greenburg, S. A.; MacMillan, H. F.; and Sklensky, A. F.: Solar Radiation-Induced Damage to Optical Properties of ZnO-Type Pigments. NAS8-18114 Technical Summary Report, July 1966 - February 1968.

BIBLIOGRAPHY

Arvesen, J. C.: Spectral Dependence of Ultraviolet-Induced Degradation of Coatings for Spacecraft Thermal Control. vol. 21, AIAA Progress in Astronautics and Aeronautics, G. Heller, ed., 1967.

Bonette, A.; Bridge, H. S.; Lazarus, A. J.; Rossi, B.; and Scherb, F.: Explorer 10 Plasma Measurements. J. of Geophys. Res., vol. 68, no. 13, July 1963.

Breuch, R. A.; and Greenburg, S. A.: Recent Coatings Developments and Exposure Parameters. Presented at Thermal Control Working Group Meeting, August 16-17, 1967, Dayton, Ohio. (Used by permission of author.)

Coon, J. H.: Solar Wind Observations. Atomic Energy Commission Report LA-DC-8944.

Gaumer, R.; Streed, E.; and Vajta, T.: Methods for Experimental Determination of the Extraterrestrial Solar Absorptance of Spacecraft Materials. Measurement of Thermal Radiation Properties of Solids, 1963, NASA SP-31, a symposium, Dayton, Ohio, September 5-7, 1962.

Heller, G.: Thermal Problems of Satellites. Materials in Space Environment, Proc. of Fifth Sagamore Ordnance Materials Res. Conf., Syracuse U. Res. Inst., MET 597-596, September 1958, pp. 89-126.

BIBLIOGRAPHY (Concluded)

Heller, G.: Requirements for Emittance Measurements of Thermal Control Surfaces of Spacecraft. Measurement of Thermal Radiation Properties of Solids, 1963, NASA SP-31, a symposium, Dayton, Ohio, September 5-7, 1962.

Neel, C. B.: Research on the Stability of Thermal Control Coatings for Spacecraft. October 1963, NASA-TMX-51, p. 196.

Neel, C. B.; and Robinson, G. G.: Measurement of Thermal Radiation Properties of Temperature-Control Surfaces in Space. Measurement of Thermal Radiation Properties of Solids, 1963, NASA SP-31, a symposium, Dayton, Ohio, September 5-7, 1962.

Schafer, C. F.; and Bannister, T. C.: Thermal Control Coatings Degradation Data from the Pegasus Experiment Packages. Thermophysics of Spacecraft and Planetary Bodies, G. Heller, ed., AIAA, vol. 20.

Snoddy, W.; and Miller, E.: Areas of Research on Surfaces for Thermal Control. NASA SP-55, 1965.

Wolf, J. H.; Silva, R. W.; and Myers, M. A.: Observations of the Solar Wind during the Flight of Imp 1. J. of Geophys. Res., vol. 71, no. 5, March 1966.

Zerlaut, G. A.: Study of In-Situ Degradation of Thermal Control Surfaces. IIT Res. Inst. NASA Contract No. NAS8-21074, February - March 1968, Technical Progress Report. (Final report to be published.)

PORTABLE SOLAR REFLECTOMETER

By

Joe E. Zimmerman

SUMMARY

A laboratory prototype reflectometer is described that measures reflectance in 11 wavelength bands covering the spectrum from 0.25 to 2.5 microns. An integrating sphere is used in the detecting system with the sample placed over a small hole in the sphere wall. The instrument is battery powered and has a satellite tape recorder included as part of the electronics so that the reflectometer is entirely self-contained. The operation of the instrument is discussed and some representative sample reflectance is presented.

INTRODUCTION

Several experiments have been conceived and proposed wherein surface characteristics are to be studied as a function of time in space. One of these experiments involved an orbital rendezvous with a Pegasus satellite and an astronaut's EVA to make reflectance measurements on some selected thermal control samples located on the satellite's solar panels. The characteristics of the thermal control samples were well defined in an earth laboratory, but information was required about the surface's degradation after long-term exposure to the space environment. Space-rated instruments were not available to perform such measurements; therefore, a development program was undertaken to provide a portable, self-contained reflectometer that could be operated by an astronaut during an EVA.

An instrument is described that could be used in a space environment to obtain surface reflectance characteristics in 11 wavelength intervals from 0.25 to 2.5 microns. The instrument is battery operated with all data processed and stored internally on magnetic tape.

DESIGN GUIDELINES

In order for the portable reflectometer to produce useful data, it must possess characteristics and accuracies comparable to laboratory type instruments. To satisfy this requirement, an integrating sphere was specified as a component in the measurement system. The absolute reflectance of the sample could then be obtained by comparing the spectral brightness of the internal sphere wall when directly illuminated, to the spectral brightness of the sphere wall when illuminated by the reflections off the sample. Table I is a summary of the design goals for the portable reflectometer.

The instrument was to be constructed in two modular components: (1) the optical head, which is a hand-held device housing the integrating sphere, the optical system including light sources, the detectors, and the other associated electronics not feasible for location in the electronics module, and (2) the electronics module, which would include the batteries, the power supplies, the signal conditioning circuits and the data recording system.

DETECTION METHODS

An integrating sphere may be used to measure the absolute reflectance of a sample by comparing the intensity of the sphere wall when illuminated by reflections from the sample to the intensity when the sphere is illuminated by reflections off a portion of the sphere wall. Figure 1 shows an incident flux beam, E_i, entering a sphere through an entrance port and focused on the sample. If the sample has a reflectance of ρ_s, then the flux leaving the sample has a value of $\rho_s E_{is}$. If the sample is specular (mirror surface), the reflected beam will take the path shown in Figure 1, striking

TABLE I. DESIGN GOALS

1. Spectral Scan and Resolution:

   0.25 - 0.35 microns
   0.35 - 0.45
   0.45 - 0.55
   0.55 - 0.75
   0.75 - 0.95
   1.0 - 1.5
   1.5 - 2.0
   2.0 - 2.5

2. Accuracy: ±2% of full scale with no discrimination between specular and diffuse samples

3. Repeatability: ±1% of full scale

4. Scan Rate: 15 seconds maximum for complete spectral scan of one sample

5. Minimum Sample Diameter: 1.25 cm

6. Data Recording: Self-contained tape recorder

7. Size: $32 \times 32 \times 30$ cm^3

8. Weight: 14 kg

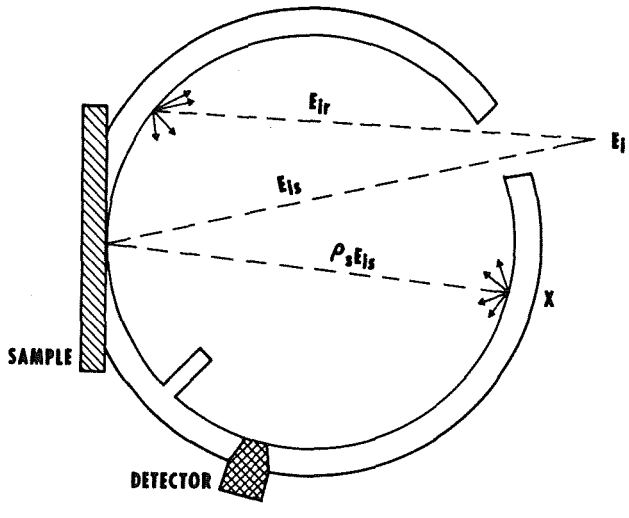

FIGURE 1. INTEGRATING SPHERE THEORY

the sphere wall at point X, and be diffused throughout the sphere. The detector will respond proportional to the ratio of the detector area to the spherical area, A_d/A_s; i.e., $E_{is}\,\rho_s\,\rho_w\,A_d/A_s$.

Now, if the incident beam is shifted so as to strike the sphere wall, the detector will respond to an intensity proportional to $E_{ir}\,\rho_w\,A_d/A_s$. The ratio of the detector's response to the two beams is then

$$\frac{E_{is}\,\rho_s\,\rho_w\,(A_d/A_s)}{E_{ir}\,\rho_w\,(A_d/A_s)} = \rho_s \quad .$$

This greatly simplified, integrating-sphere theory serves to illustrate that the measurement is absolute, since the sphere wall reflectance cancels out of the ratio expression. This is a good approximation if the sphere wall is highly diffuse, its reflectance is high, and the ratio of hole areas to sphere area is low.

The portable reflectometer is to operate over the spectral range from 0.25 to 2.5 microns; therefore, the sphere coating must also meet its requirements over this range. Several types of coatings existed which were good from the visible through the infrared or visible through the near ultraviolet spectral range, but few materials existed that were adequate for both cases. The reflectometer required near ultraviolet, visible, and near infrared in one coating.

The most commonly used material for a sphere coating is magnesium oxide, MgO, which has a broad spectral band of high reflectance. It is relatively easy to apply, but has the disadvantage of being fragile. Smoked MgO is not, by itself, well suited for the portable instrument primarily because of its lack of mechanical strength.

A substrate was produced using a potassium titanate base with a silicate binder. This gave a highly reflective surface (on the order of 97 to 98 percent) in the visible and near infrared; however, it dropped quite sharply to unacceptable levels at wavelengths shorter than 0.35 microns. Barium sulphate was then added to the mix and the ultraviolet reflectance was improved. The substrate with 10 percent barium sulphate was then coated with MgO to produce a completely acceptable sphere coating. In addition to the good reflectance characteristics, the MgO would adhere to the substrate much better than to the bare aluminum sphere wall.

The light source consists of a low-pressure mercury arc lamp for illuminating the sphere in the ultraviolet wavelengths and a tungsten arc lamp for

use in the visible and infrared channels. An attempt was made to use a single tungsten arc lamp over the entire spectrum, but the ultraviolet output was too low to provide an acceptable signal-to-noise ratio for detection. The light sources are focused to produce a spot approximately 0.476-cm (3/16-in.) diameter on the sample and sphere wall, alternately. A rotating aperture will block the tungsten lamp from the sphere during the time that data are being taken in the 0.25 to 0.547 micron range. The rotating aperture will also block the mercury lamp from the sphere in the 2.5 micron filter position to eliminate any problem of fluorescence that might otherwise occur.

A special filter wheel, Figure 2, was designed to provide selective-wavelength filtering of the light sources and also to hold the beam-switching mirrors for each filter position. The sample mirrors and reference mirrors are inclined at 45 degrees and 52.5 degrees, respectively, to provide 15 degrees differential between the sample beam and the beam that strikes the sphere wall.

Two detectors are used to cover the required wavelength interval. A photomultiplier tube (RCA type C70129C) is used to cover the region from 0.25 microns through 0.547 microns. The photomultiplier tube has an S4 cathode with a sapphire window. Its peak response is at 0.375 microns

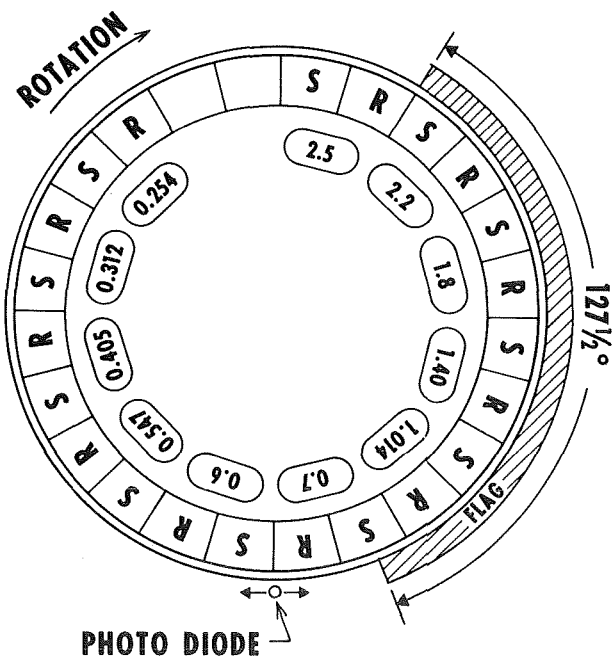

FIGURE 2. FILTER WHEEL

with the response falling to about 86 percent at 0.25 microns. A lead sulfide (PbS) detector (SBRC type 20A) with a sensitive area of 9 mm^2 is used to cover the region from 0.6 microns through 2.5 microns. The PbS detector was chosen as the infrared detector because of its high sensitivity at the long wavelength portion of the spectrum and because of its ability to function at room temperature. The PbS detector response peaks at about 3 microns; however, it has sufficient sensitivity to be useful into the visible regions of the spectrum.

Both of the detectors are mounted on the sphere so that their active surfaces become an integral part of the inner sphere surface. The detectors are located behind an optical shield so that first reflections off the sample will not strike the active areas of the detectors. They will, however, be permitted to sense the first reflected flux from the reference beam striking the sphere wall. The use of the detector shield allows the determination of absolute reflectance whether the sample characteristics are specular or diffuse.

OPTICAL SYSTEM DESIGN

The physical implementation of the above detection approach into the reflectometer was initiated as shown in Figure 3. It was desired to make reflectance measurements in a minimum of 8 wavelength intervals, each about 200 angstroms wide. With the 10-cm (4-in.) diameter filter wheel, it was feasible to place a maximum of 12 filters around the wheel. One filter position was left blank for use as a dark reference, leaving 11 filters to cover the 0.25 to 2.5 micron range.

The filter wheel is motor driven at a rate of 1 Hertz. A timing pulse is generated at the beginning of each spectral scan by a flag on the periphery of the wheel interrupting a light beam on each revolution of the filter wheel. The photo cell pulse circuit also serves as a reference for switching the appropriate detector output into the data recording circuit. A chopper is driven from the periphery of the filter wheel at a rate of 12 Hertz. The chopper wheel is divided into 10 segments, thus providing a chopped light frequency of 120 Hertz. Another photocell circuit associated with the chopper wheel is used to provide a data synchronization pulse for each filter and light beam position.

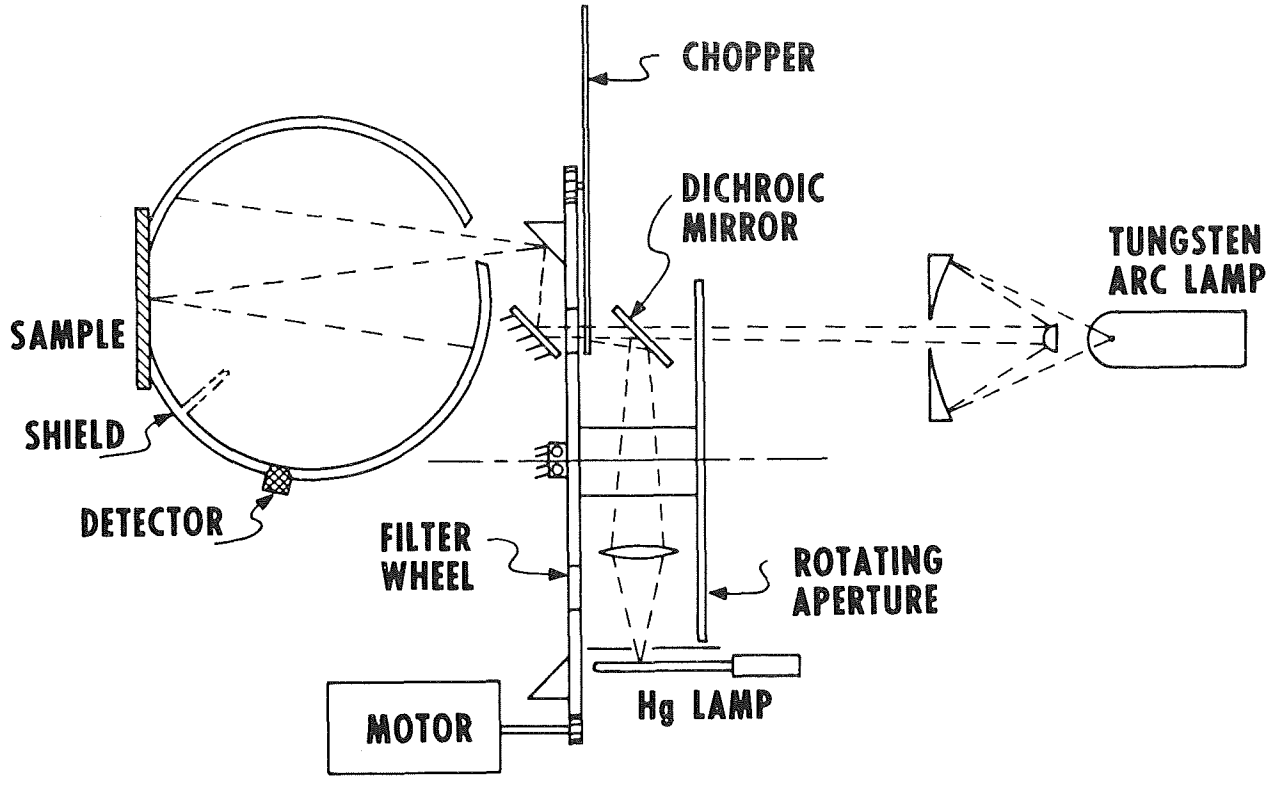

FIGURE 3. REFLECTOMETER OPTICAL DESIGN

Figure 4 shows the relationship between the rotating mirrors, filters, incident beam cross section, and chopper blade openings with respect to filter wheel position. It can be seen that every fifth opening of the chopper blade represents a valid data point for reading the detector outputs.

The detector outputs are fed through preamplifiers to a wavelength interval selector and attenuator where a different system gain is introduced for each wavelength or filter position. This was required because of the wide variations in spectral emission of the lamps and spectral transmission through the filters. The wavelength interval selector also selects the proper detector output for further signal conditioning, depending upon the filter wheel position. The pulses from the detector are then clamped to a common dc reference level and fed through a peak detector where they are also shaped to a uniform width. The valid data pulses are next sampled by the analog-to-digital converter and converted to 8-line parallel-output information. The final data are serialized and recorded in the time interval between valid data pulses. Figure 5 shows a block diagram of the electro-optical components of the instrument.

PROTOTYPE DESIGN

A prototype reflectometer has been designed and fabricated that basically conforms to the original design guidelines. The instrument, Figure 6, retains the modular concept of the hand gun and the electronics module, but additional features have been added to facilitate laboratory operation and checkout.

The hand gun contains all the optics, filtering, and detection mechanisms as described earlier, plus the detector and lamp power supplies. Preamplifiers and source followers for the optical detectors are also included in the hand gun portion. Two switches on the hand gun are used to (1) start the drive motor that turns the filter wheel and chopper, and (2) turn on the lamps. The size of the hand gun is approximately 22 cm by 18 cm by 11 cm.

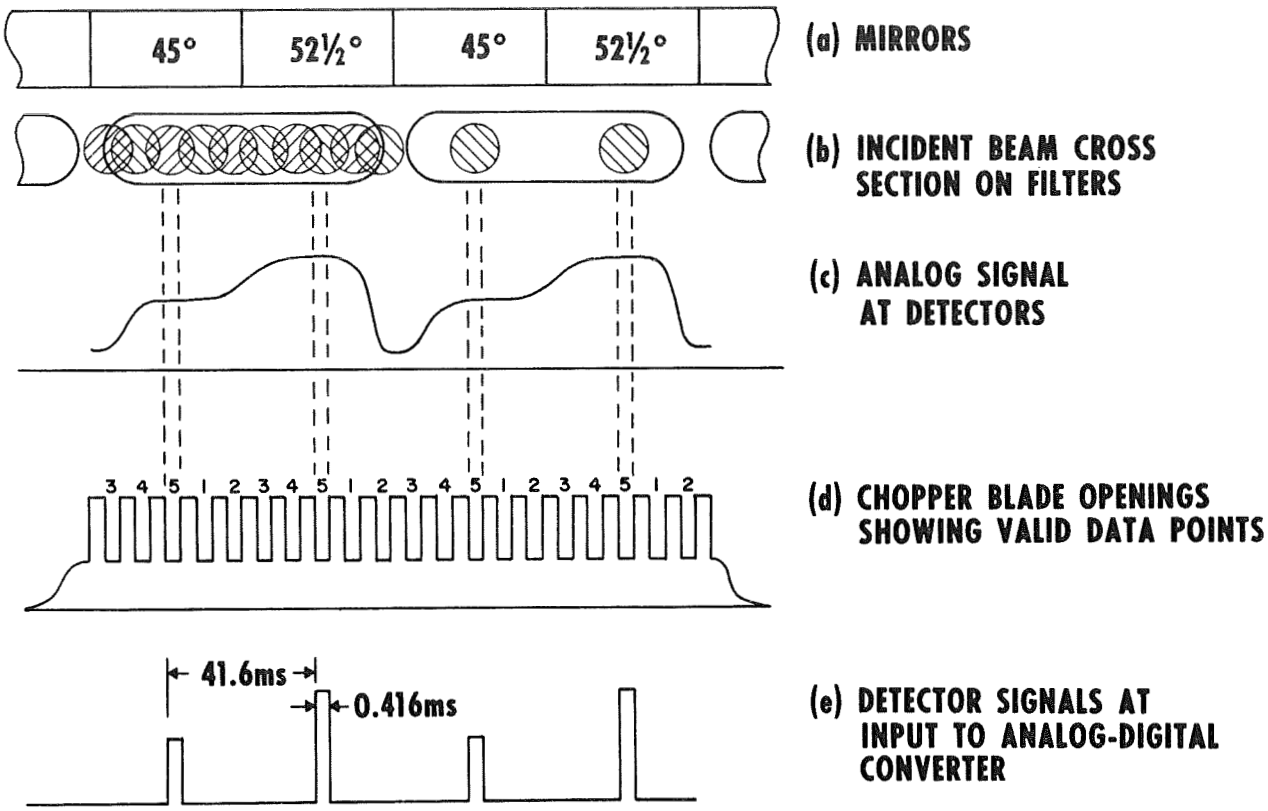

FIGURE 4. OPTICAL MECHANICAL RELATIONSHIP OF REFLECTOMETER

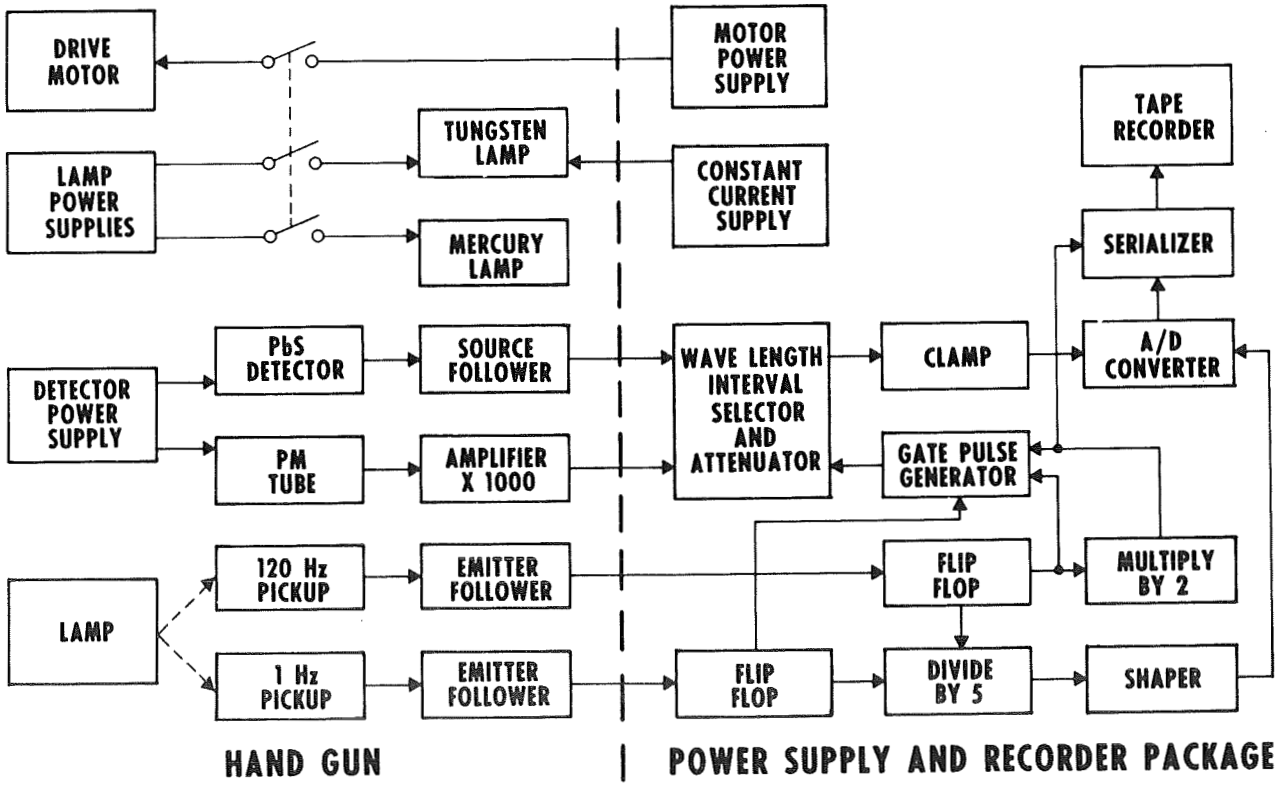

FIGURE 5. BLOCK DIAGRAM OF REFLECTOMETER ELECTRONICS

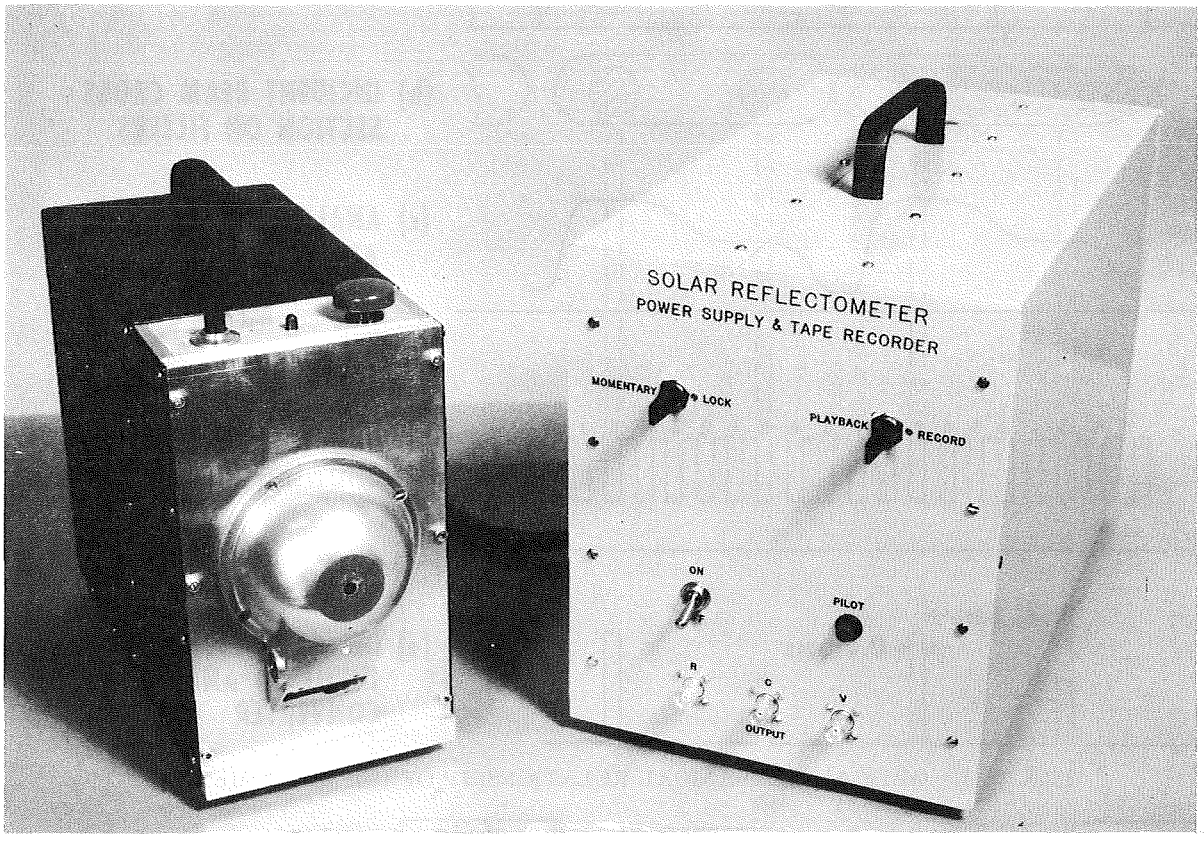

FIGURE 6. LABORATORY PROTOTYPE REFLECTOMETER

The electronics module contains the data processing and recording system and the main power supply. The wavelength interval selector and attenuator, counting circuits, analog-to-digital converter, and serializer are constructed on printed circuit cards and packaged to occupy a minimum volume. The tape recorder is a Parsons, type SIR-940, magnetic tape recorder/reproducer designed specifically for use on satellites or earth orbital vehicles. The recorder incorporates 336 m (1100 ft) of 25.4 μ (1 mil) base magnetic tape with record and reproduce speeds of 3.18 cm/sec (1.25 in./sec). The recording mechanism has the capability of four channels of information; one will be used as a voice channel for recording pertinent details of operation, and two other channels will be used for data recording. The recorder operates from unregulated 28 Vdc and nominally consumes 5.88 watts of power. The electronics module is packaged in a container 32 cm long, 18 cm wide, and 20 cm high.

The main power supply for the reflectometer is a bank of batteries located in the electronics module. Flight hardware would use silver-zinc batteries; however, for laboratory convenience, rechargeable nickel-cadmium batteries are used to produce the 28 Vdc. An additional convenience feature is a power supply module that fits in place of the battery pack and allows the instrument to be operated from 115 Vac for laboratory use.

Reflectance data taken with the instrument on representative material samples indicate very good conformance to the design goals. Table II shows the measured values of reflectance as compared

TABLE II. REFLECTOMETER PERFORMANCE DATA

	λ = 0.547 microns			λ = 0.700 microns			λ = 1.80 microns		
	Std.	Meas.	% Error	Std.	Meas.	% Error	Std.	Meas.	% Error
Mirror	0.882	0.900	+1.8	0.800	0.796	-0.4	0.966	0.986	+2.0
Aluminum Foil	0.875	0.856	-1.9	0.870	0.817	-5.3	0.965	0.935	-3.0
Sand Blast.	0.270	0.265	-0.5	0.280	0.250	-3.0	0.495	0.490	-0.5
White Diffuse	0.940	0.960	+2.0	0.940	0.935	-0.5	0.810	0.822	+1.2

with the accepted standard values for each material sample at selected wavelengths.

CONCLUSIONS

A portable, laboratory-prototype reflectometer has been developed for use in making spectro-reflectance measurements in the 0.25 to 2.5 micron wavelength range. An integrating sphere is used in conjunction with a rotating filter wheel; the absolute reflectance of the sample may be obtained in 11 discrete wavelength bands over the operating spectrum. The instrument is entirely self-contained with sufficient power and recorder tape to allow 2 hours of reflectance data to be recorded. The instrument was designed to use space-rated components so that only mechanical repackaging, for astronaut or experiment considerations, would be required to provide a completely space-rated instrument.

CONTAMINATION DURING THERMAL VACUUM TESTING

By

James M. Zwiener

SUMMARY

Thermal vacuum testing of spacecraft payloads has become a standard practice in the flight hardware testing sequence. Subsequently, with the advent of large optical payloads on a one-of-a-kind basis where the optical elements are difficult or impossible to replace on a practical basis, the question of possible optical degradation by contamination from the pumping systems has been raised. Well controlled laboratory tests have shown that optical degradation by contamination from the pumping systems is possible, and that the damage (1) occurs only in the ultraviolet (below 0.3 microns), (2) increases with exposure time, (3) is related to ultraviolet irradiance, and (4) occurs in oil systems as compared to oil free (ion) systems. Also, electron-microscope studies have revealed that the contaminant is composed of what may be described as a homogeneous layer covered with larger particles ranging from 0.5 microns to 20 microns in size.

INTRODUCTION

During the past year, laboratory tests have been performed to determine if optical degradation through the mechanism of contamination could occur in typical space-environmental simulation systems. With the advent of large optical spacecraft payloads undergoing extensive thermal vacuum testing, where replacement of degraded optical elements is impractical or impossible, degradation by contamination has become a very serious problem. Throughout this study, optical degradation will refer strictly to the loss of reflectance of a mirror. Within large vacuum systems, the contaminants usually consist of backstreaming hydrocarbons originating from mechanical roughing pumps and oil diffusion pumps, or in the case of ion pumped systems, can originate from saturated ion pumps where trapped gases are liberated by continued pumping action.

TEST APPROACH

Two typical laboratory space-environmental simulation systems were tested for contamination. One system had an oil type pumping system and the other had an ion type pumping system. The oil system consisted of a Welch mechanical roughing pump plus a Roots blower to bring the total system to a pressure of about 1.3 N/m^2 (10 microns). At that pressure, an oil-diffusion pump lowers the system pressure to the 13.33×10^{-5} N/m^2 (10^{-7} torr) range. The diffusion pump (Fig. 1) utilized both an optical and a liquid nitrogen cooled trap. The oils used were Convalex 10 and Conval 20 (CVC brand names) in the diffusion pump and mechanical pump, respectively [1]. A picture of the overall oil system

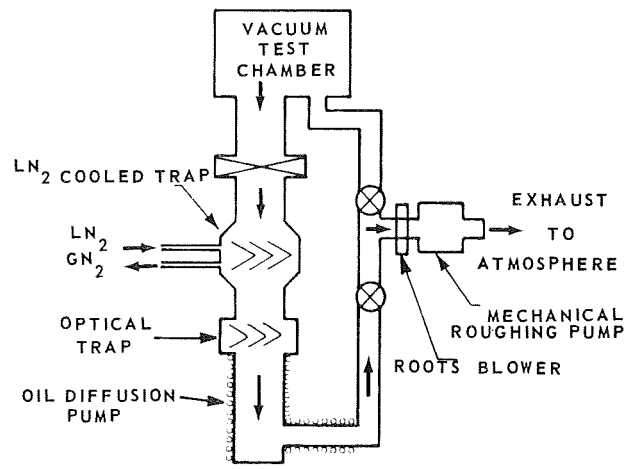

FIGURE 1. LABORATORY VACUUM SYSTEM — OIL

is given in Figure 2, showing the pumping system, sample chamber, and high-pressure mercury-arc lamp irradiation source. In some tests a high pressure Xenon or infrared lamp was used. A closeup of the sample chamber is shown in Figure 3. The samples are mounted on a water cooled stainless steel test bed.

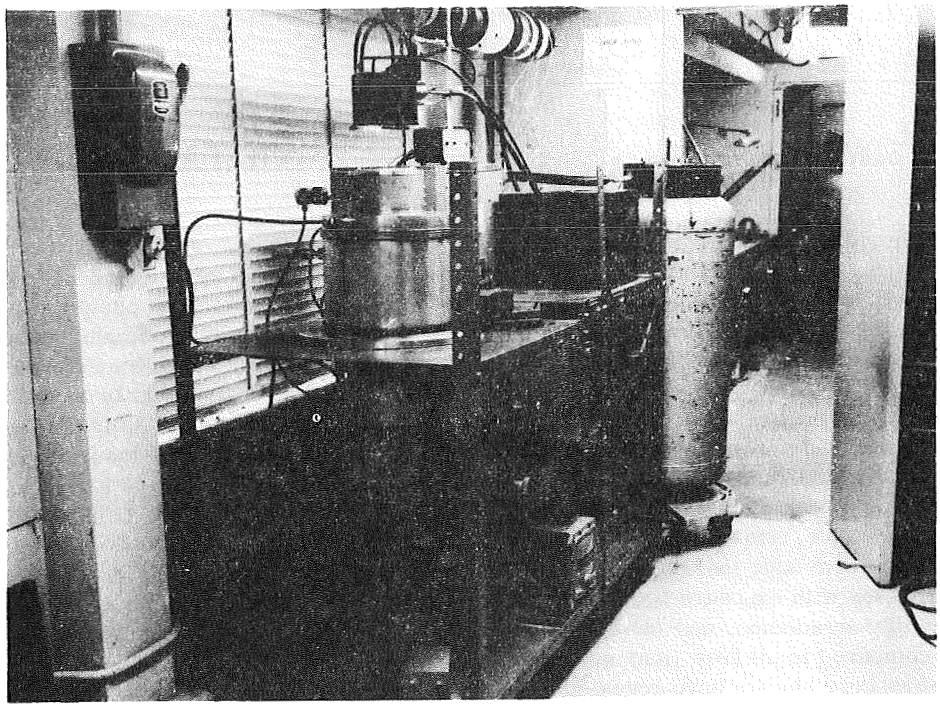

FIGURE 2. VACUUM SYSTEM — OIL

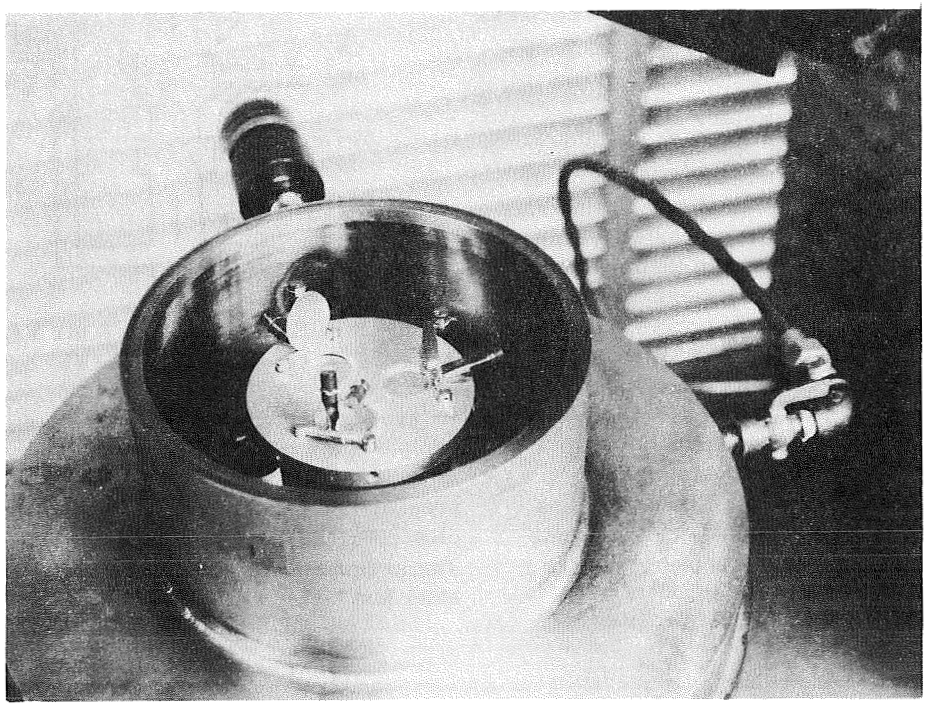

FIGURE 3. SAMPLE CHAMBER — OIL SYSTEM

The ion system, shown schematically in Figure 4, consisted of liquid nitrogen cooled sorption pumps and ion pumps. In the contamination tests, the titanium sublimation pump was not used. An overall picture of the ion system is presented in Figure 5, showing the three sorption pumps and ion pumps. A closeup of the test chamber and irradiance source is shown in Figure 6; note that a quartz window is used on both the test chambers, and all O-rings were Viton-A (to minimize outgassing).

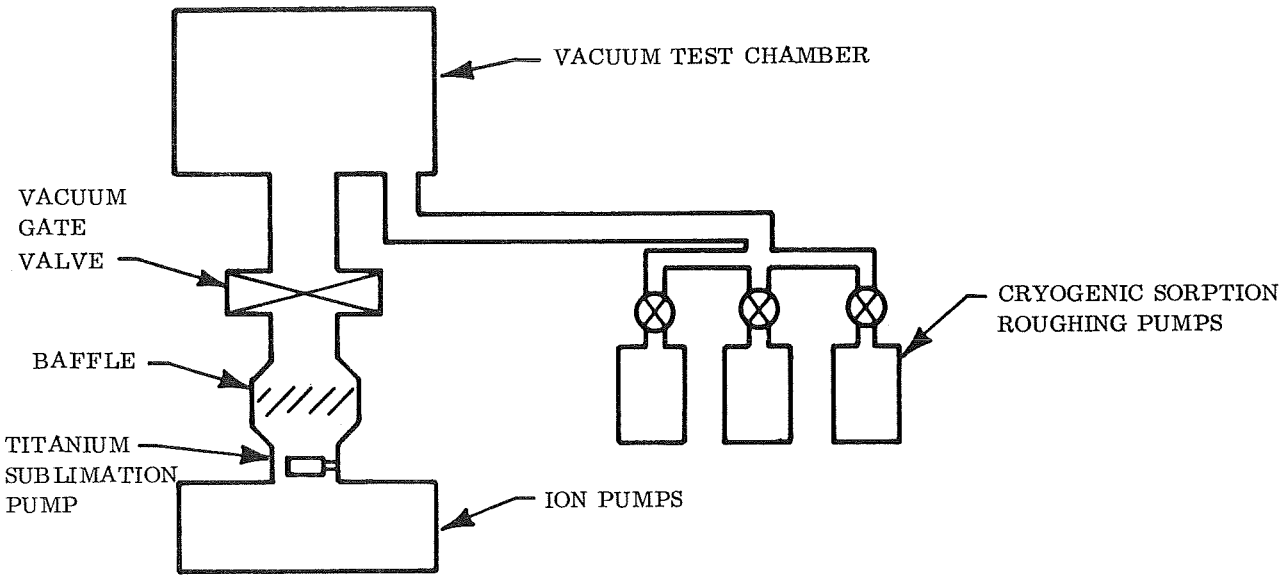

FIGURE 4. LABORATORY VACUUM SYSTEM — ION

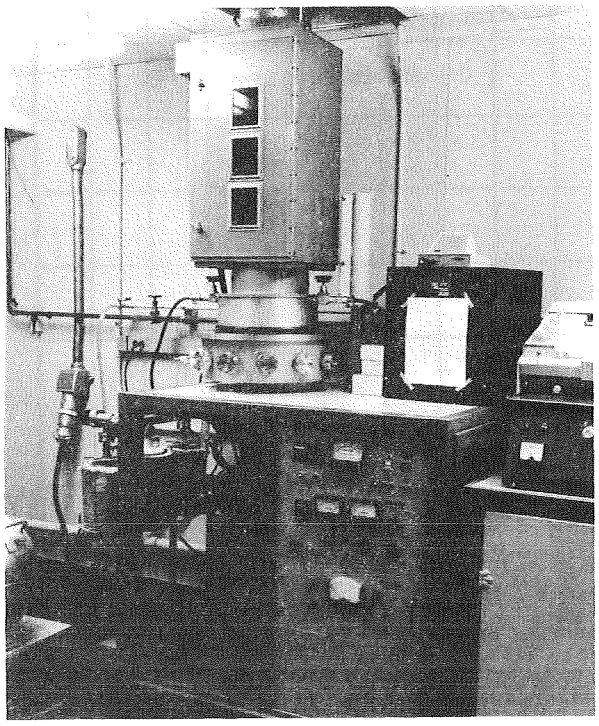

FIGURE 5. VACUUM SYSTEM — ION

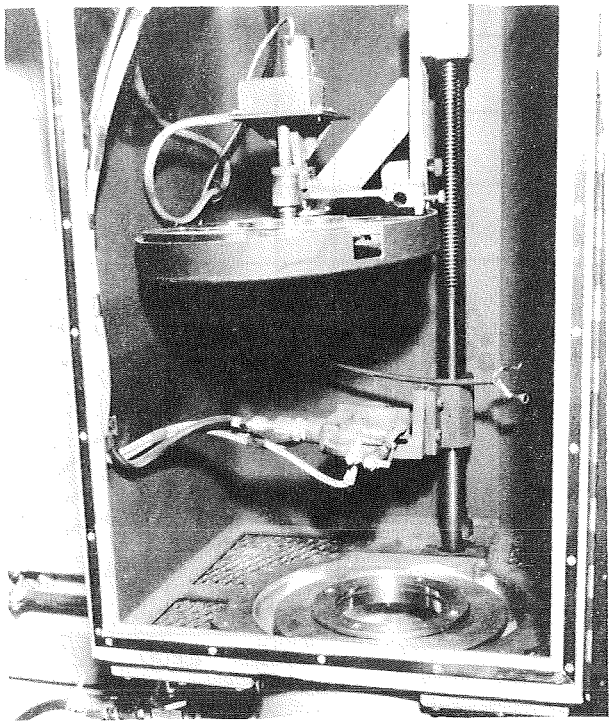

FIGURE 6. SAMPLE CHAMBER — ION SYSTEM

The technique used for measuring optical degradation was to use six mirrors, two each in the ion system and oil system, along with two control mirrors. In the vacuum systems, the samples were exposed to the vacuum environment while simultaneously being irradiated with the ultraviolet source. Optical degradation measurements were performed using a Beckman DK-2A scanning spectroreflectometer. The reflected energies from the exposed mirror were compared to those from the control mirror, thereby determining changes in reflectance.

TEST RESULTS

The results of the test described above are shown in Figure 7. The data in the figure are taken from two samples exposed in the oil system for periods of 50 hours with ultraviolet radiation. Measurements of changes of reflectance were made at every 50-hour interval up to 200 hours total irradiation exposure. Wavelength coverage was from 0.2 microns to 2.8 microns. Note that identical samples in the ion system exposed at the same time and at the same irradiance intensity levels did not show any measurable damage, whereas the mirrors in the oil system showed a loss of reflectance starting at approximately 0.25 microns and increasing to shorter wavelengths. Also, note that damage increases with exposure time. No measurable damage has been detected up to 2.8 microns in the near infrared.

Another test was performed to gain some idea of the effects of source-spectral irradiance. Again, mirrors were exposed in the oil system, but this time an infrared source was used for irradiance purposes. No detectable changes in reflectance were measured after the exposure in the oil system. The samples were then exposed in the ion system to the ultraviolet source. Measurements now showed a loss of reflectance as shown in Figure 8, thereby indicating that a nondegrading contaminant was deposited on the mirrors in the oil system which then degraded later under ultraviolet radiation in the ion system.

Figure 9 shows the results of a stereo-scan electron microscope picture of one of the samples degraded in the oil system. These pictures were

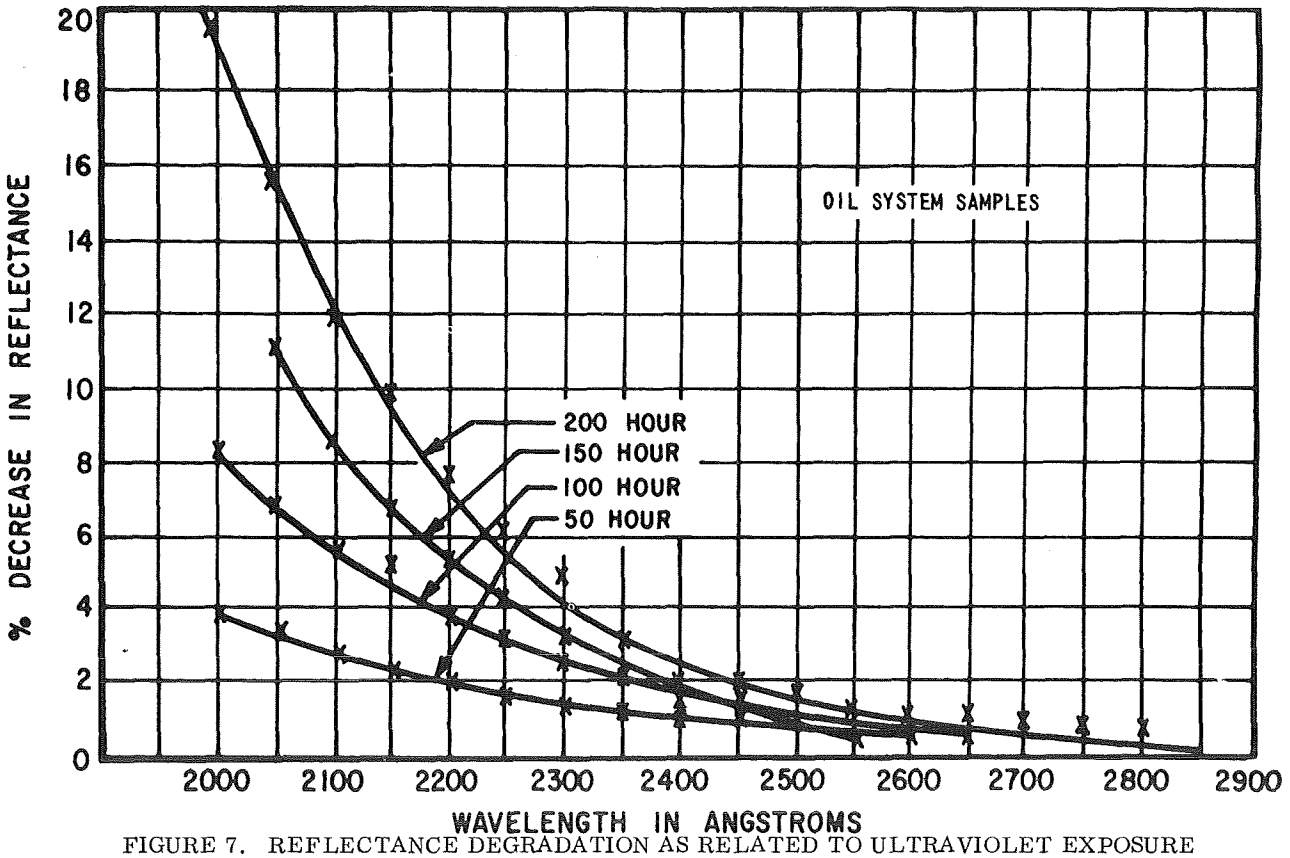

FIGURE 7. REFLECTANCE DEGRADATION AS RELATED TO ULTRAVIOLET EXPOSURE

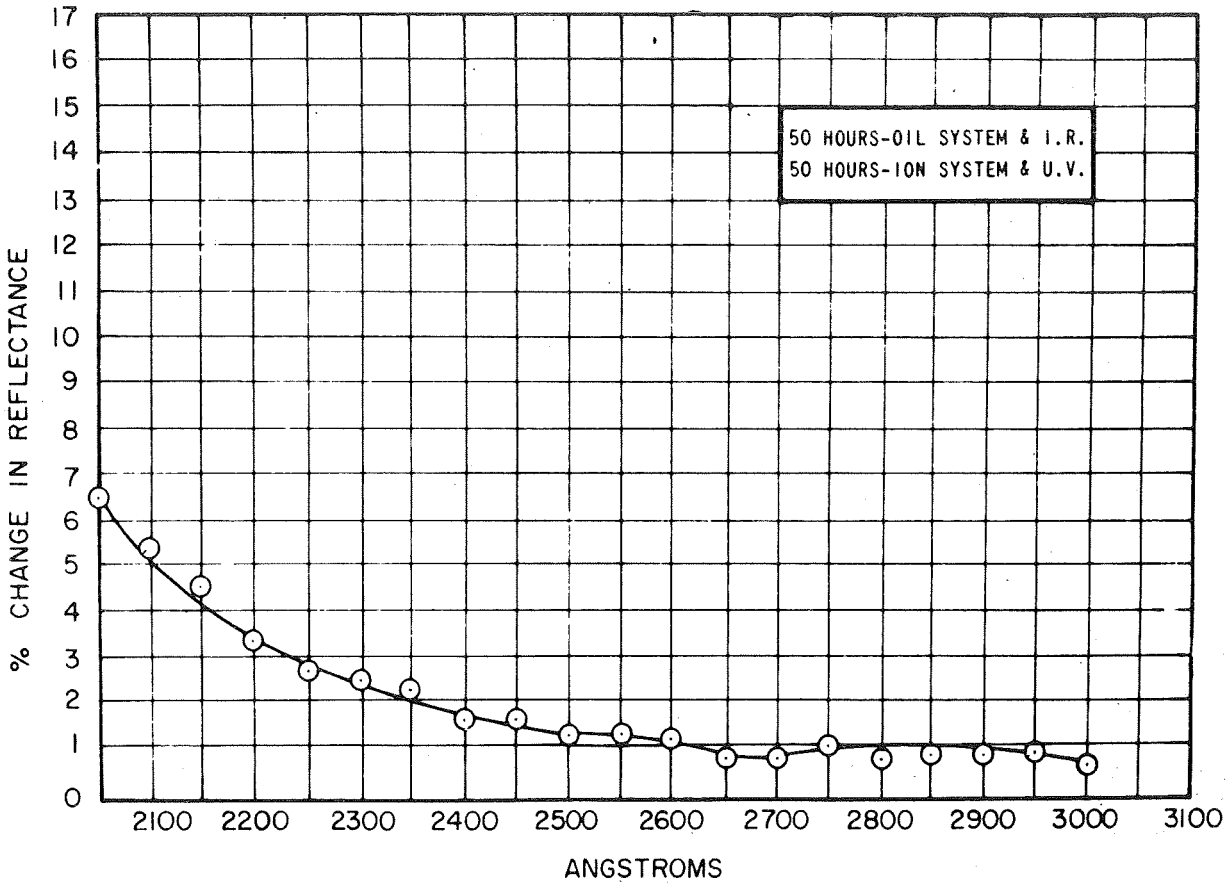

FIGURE 8. REFLECTANCE DEGRADATION IN AN OIL VACUUM SYSTEM

obtained by Dr. A. H. Weber, University of Saint Louis. In Figure 9, clean aluminum appears as a light homogeneous grey area, representing the area on the mirror surface protected from contamination by the edge of the mirror holder as seen in Figure 3. A control mirror not exposed to either the oil or ion system showed only a continuous light grey as in the clean area in the upper left-hand part of Figure 9. The samples were cut to fit in the microscope; the cut edge is apparent in the upper left-hand part of Figure 9. The dark stain with the small particles distributed on the surface is the contaminated area. Remember, as shown in the decrease in reflectance curves, this contaminant is not visible with the use of a high-powered microscope in white light.

CONCLUSIONS

These studies have shown that a typical oil system has the potential of contamination even under careful operation, and that a typical ion system using sorption-roughing pumps does not result in measurable optical degradation (less than 0.5 percent). It was shown that optical damage apparently only occurs below 0.3 microns, and that the damage increases at lower wavelengths to at least 0.2 microns. It was shown that ultraviolet radiation is necessary for degradation to occur, but this is not necessary for condensation of a contaminant on a surface. Finally, it was shown that the contaminant does not form a homogeneous layer, but it is an even layer topped with particles ranging in size from around 0.5 microns (or less) to 50 microns.

Future work will be directed toward determining the degradation occurring in the vacuum ultraviolet region to 0.06 microns and trying to find absorption spectra in the infrared to identify contaminants. Also, efforts will be made to identify the contaminant by using surface analysis techniques such as Auger spectrometry and electron probe analysis. Luminescence and polarization effects in the vacuum ultraviolet will also be studied.

All these studies will eventually lead to the development of techniques to either eliminate contamination or decrease it to an acceptable level.

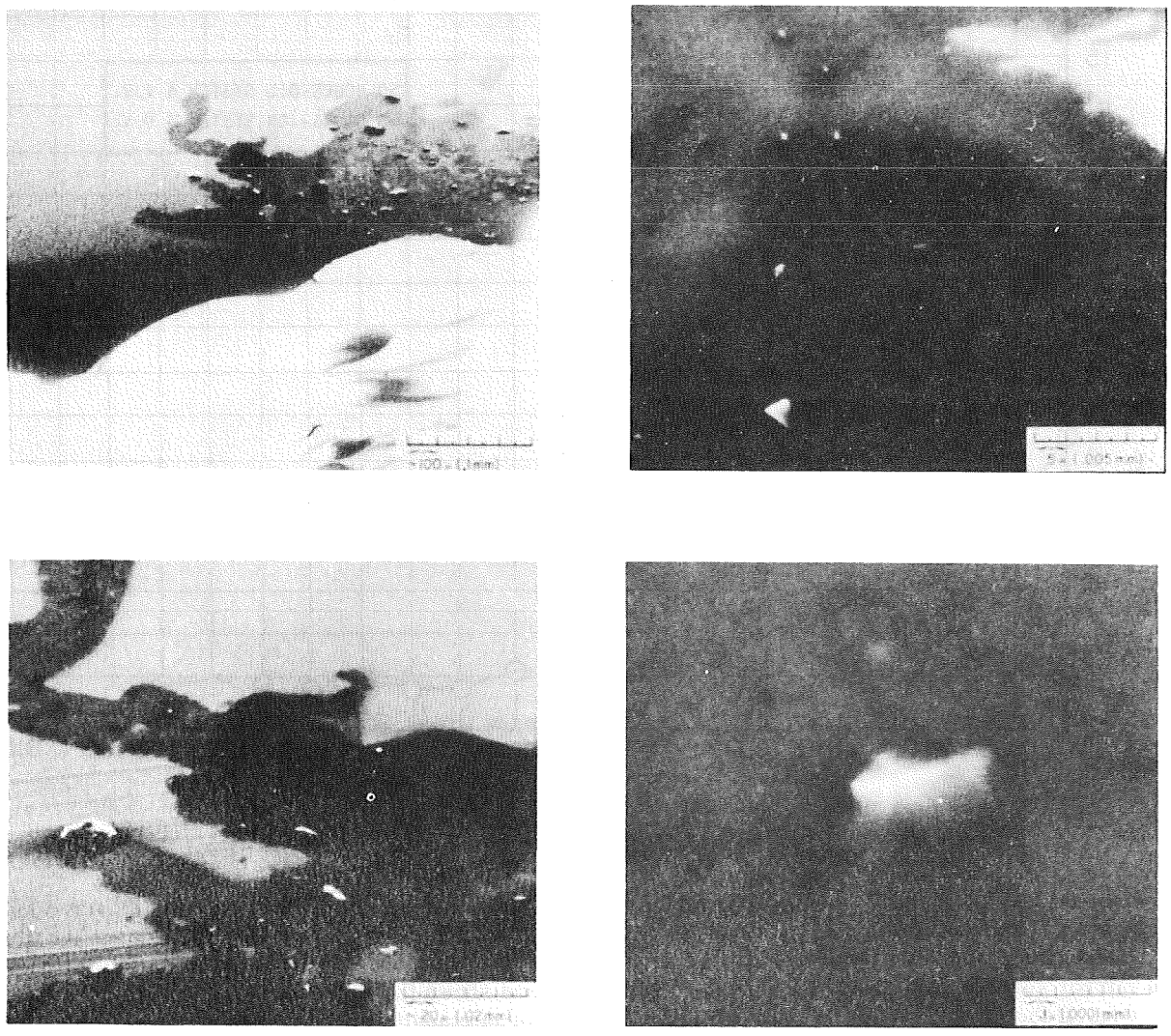

FIGURE 9. SCANNING ELECTRON MICROSCOPE PICTURE

REFERENCE

1. Langdon, W. M.; and Fochtman, E. G.: Backstreaming in Baffled Systems. Proc. of Tenth National Vacuum Symposium, American Vacuum Society, (IIT Res. Inst.), Contract No. AEDC, AF 40(600)-1004, 1963.

THE PTD 500 THERMAL ANALYZER SYSTEM

By

Frederick D. Bachtel

SUMMARY

This paper discusses the PTD500 digital thermal analyzer computer program developed by the Propulsion and Vehicle Engineering Laboratory, Propulsion Division, Fluid and Thermal Systems Branch specifically for the analysis of large radiation-dominated problems. The PTD500 utilizes a thermal analog network and finite difference techniques to obtain steady-state and transient solutions to the general heat flow problem.

The purpose for constructing the PTD500 program was not to obtain a thermal analyzer as such, since many are available, but to produce a system suitable for the analysis of geometrically complex space vehicles, where radiation between various vehicle surfaces and from celestial bodies is of extreme importance. Since thermally isolating components or portions of these vehicles is difficult, mathematical models of entire vehicles must be constructed. These models necessarily contain large radiation networks and an extensive set of external heat rate tables. Consequently, the major portion of computer storage must be allocated to data, and storage required for program logic must be minimized. Since complex vehicle geometry also necessitates shape factor and heat rate programs to calculate the majority of the thermal analyzer input data, an economical method of transferring large amounts of data between runs is mandatory. Finally, long execution times are required to solve these large radiation-dominated networks. Erroneous runs, caused by input (format) errors or network description errors, are highly undesirable.

To satisfy the objectives set forth above, the PTD500 system was constructed in modular form utilizing files for storage of input, intermediate, and output data, and depending upon the installation's system (1108 EXEC), for primary control (file manipulation, sequencing of execution, etc.). The PTD500 maintains its own control language to direct operations within the various modules of the system. The PTD500 operates in four independent phases: input, network processing, network solution, and output. Various utility programs are available to provide versatility in linkage between phases and to interface input/output to other programs.

LIST OF SYMBOLS

Symbol	Definition
C_i	Thermal capacity of node i
C_p	Specific heat
f	Script F form factor including area
G_{ij}	Thermal conductance from nodes i to j
Gr_{ij}	Linearized thermal conductance (radiation) from nodes i to j
k	Thermal conductivity
M	Mass
N_{ij}	Distance from i to j
q	Heat transfer rate (energy/time)
RAD	Radiation constant
S	Area
T_i^t	Temperature of node i at time t
t	Time
β_{min}	Stability criteria
ρ	Mass density
σ	Stefan-Boltzmann constant

INTRODUCTION

The computer program described in this document was written because of the inability of currently available thermal analyzers to satisfactorily handle thermal design problems encountered in the Apollo Applications Program (AAP). In general, the thermal design associated with space vehicles of the AAP type is significantly different from previous thermal problems for which the current thermal analyzers were written.

These space vehicles, containing a multitude of individual components, have become geometrically complex. In addition, the majority of the components are normally in an open environment and thus produce extensive radiation exchange, consisting of infrared radiation between various components of the vehicle, solar radiations, and albedo radiation. Because of the complex geometry and the open space environment, radiation becomes the dominant mode of heat transfer with complicated reflections and blockages that must be included in accurate thermal analyses.

Two additional factors contributing to the requirements for large mathematical models are the interdependency of the components and the rigid thermal tolerances that are routinely imposed. The interdependency of components, resulting from internal heat generation within each component, prohibits an effective thermal isolation of any portion of the vehicle. Thus the entire vehicle must be analyzed simultaneously for a satisfactory analysis. The rigid thermal tolerances imposed by electronic equipment result in the need for precise analyses. Consequently, a detailed mathematical breakdown of the entire vehicle is required, which results in a large mathematical model.

Variable missions further complicate this type of thermal analysis since they impose a wide range of thermal environments that must be analyzed, including various orientations, orbital parameters, and percent shadow times. These parametric studies routinely require alteration of 50 percent of the environmental data for each condition investigated.

Because of the complexity of these problems, large mathematical models have exceeded the capacity of existing thermal analyzers. Forcing the capabilities of these programs causes significant errors in thermal analysis. In addition, the overall time required for analysis has become excessive. Computer run time is significantly increased by large models, and a model may often require several runs to detect and correct network errors. The resulting loss of computer time and engineering time is extremely costly and occasionally impacts program schedules.

Another problem encountered in this type of analysis is handling large amounts of input and output data. Format restrictions on input become troublesome as the amount of data increases, and often the input language is prone to errors. Direct interface between current thermal analyzer programs and other programs required in the analysis is normally difficult. Thus, engineering time is wasted in revising output from one program to an input form suitable for another.

The PTD500 is designed to minimize these problems. Emphasis is placed on obtaining the capability to handle large problems and, at the same time, reduce the labor required by the engineer.

SYSTEM ORGANIZATION

To obtain the large amount of data storage required, the PTD500 is constructed in modular form and contains a system of programs rather than a single unit. This modular construction presents several advantages that will be discussed in the following sections. Figure 1 illustrates how PTD500 is organized, showing the modular breakdown and data allocation. The two types of storage media used are the main or active computer storage and a mass storage unit such as a magnetic drum or disk. The main storage is limited to fixed capacity, either by hardware configuration or system restrictions. All data processing must be performed on information contained within this capacity since the main storage is the only available active medium. The mass storage unit is a secondary standby storage medium which normally holds information that is not immediately required during the current computer processing activities.

In general, two types of information that must be stored within the computer are the instructions which direct the computer and the data which are processed. The storage needed for instructions or logic must be minimized to acquire increased data storage capacity required by the large

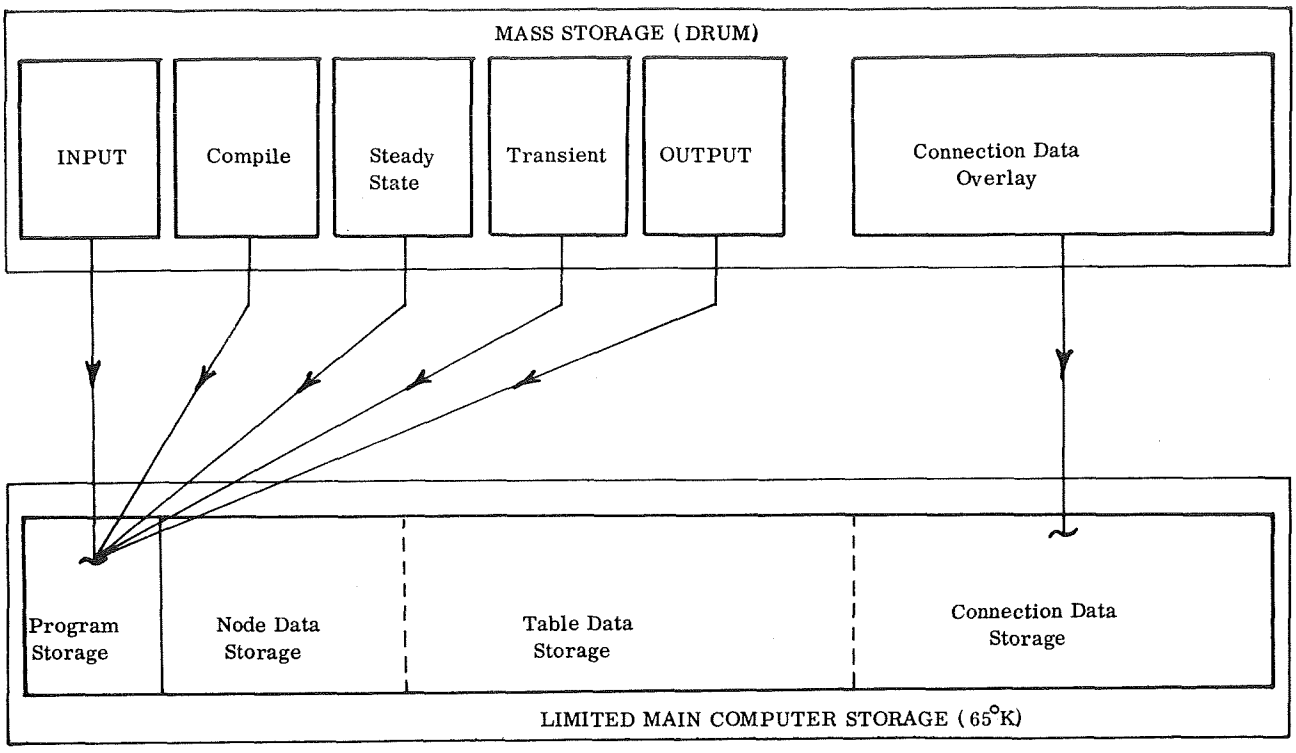

FIGURE 1. PTD500 MODULE BREAKDOWN AND DATA ALLOCATION

mathematical models. To reduce the logic storage requirements, the PTD500 was broken into five sections or modules, which can be executed separately and independent of one another. Only one module is required in the main computer storage at one time. The other modules reside on the mass storage unit. In the same manner, each module is further divided into submodules so that only one submodule is required in main storage at any given time. This overlay method, which is commonly used in other thermal analyzers to a lesser degree, allows over 90 percent of the main storage to be allocated for network data during the steady-state and transient solutions.

In addition to minimizing logic storage, allocation of network data is oriented to specific problems and to the third generation computer in an effort to achieve more efficiency, both in data storage and in turn-around time. In third generation multiprogram computers, programs requiring large amounts of main storage normally have a longer turn-around time than similar programs requiring less storage. For this reason, the PTD500 was designed so that only the steady state and transient modules require the full capacity of the main computer storage. The input module requires only 10 percent of full computer storage capacity, while the compile module operates with a 30 percent maximum storage requirement. With the PTD500 modular concept, the mathematical model can be loaded and checked for input errors by using relatively small programs, with a corresponding reduced turn-around time. The small main storage required for these modules is achieved by extensive utilization of the mass storage media to store the larger amount of network data. This technique is possible because only portions of the network data are required in main storage during the PTD500 input and compilation processes.

However, the steady-state and transient solution modules require all network data to be continuously available throughout the solution. Consequently, it is desirable for all network data to be in the main storage during execution of these modules. In this case, the mathematical model size would be limited by the capacity of the main computer storage. If the PTD500 encounters a model that exceeds the capacity of main storage, the program automatically invokes a data overlay option similar to the program overlay methods described earlier. A portion of the

network data, specifically the connection data, is continuously cycling from the drum to main storage, where it is operated on, and then back to the drum allowing another portion of the connection data to be loaded and operated on. This process obviously increases the turn-around time for the steady-state or transient solution; however, the actual processing time in main storage is not substantially increased because of operating characteristics of the third generation computers. The result of these various overlay methods is a 200 to 500 percent increase in storage capacity over previous programs, depending upon the type of model and the thermal analyzer being compared.

SYSTEM INTEGRATION

The PTD500's ability to interface with other computer programs required in the thermal analysis is one major attribute of the system. The ability to transfer data from one program to another reduces user card handling and allows more efficient use of the thermal analyzer system, thus reducing engineering time.

Figure 2 illustrates how each module of the system communicates with other modules and programs used in the analysis. In Figure 2, the block labeled EXEC 8 represents the computer operating system which controls the PTD500 modules. The user communicates with the EXEC via system control cards which call for execution of one of the 5 modules in the PTD500 system.

The block labeled DRUM Storage represents a library of data files which are blocks of data stored and catalogued on the drum by the EXEC. These data files are the key to operating the PTD500 system since they are the medium through which data are transferred between modules and from other programs

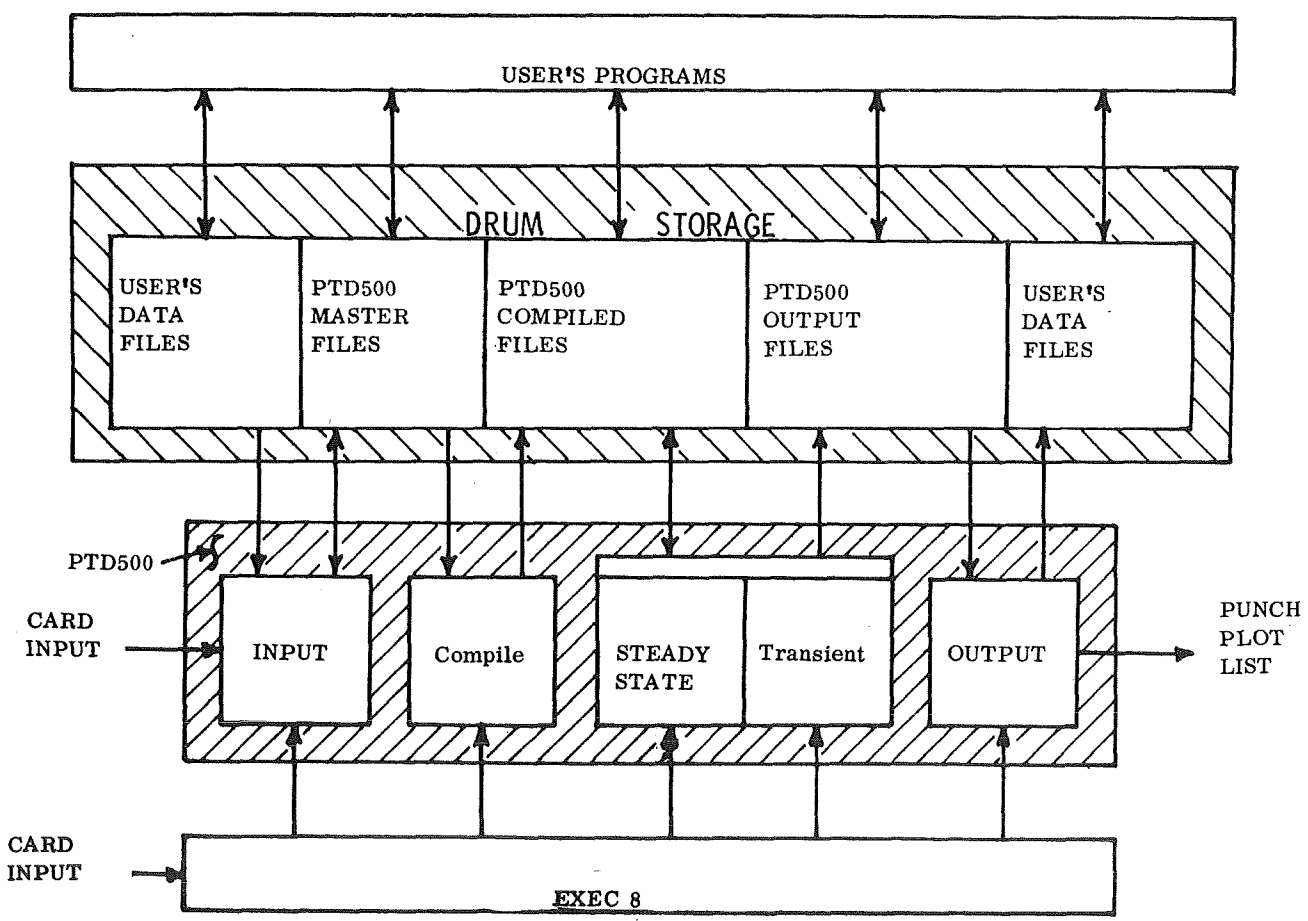

FIGURE 2. PTD500 INPUT/OUTPUT DATA FLOW

used in the analysis. For maximum effectiveness, these files should be maintained permanently intact for an indefinite time period. This would allow data to be stored effectively in the computer, thus enabling the program to save and recall data from one run to the next.

The function of the INPUT module is to merge the data streams from various users' data files with the primary data stream from cards. The output of this module is the master data file containing the entire model, or possibly a partial model constructed from the several input streams. The master file is input that is required for executing the compilation module.

The following example illustrates the utilization of this system. The nodal breakdown data and problem control data could be input from cards. The heat flux tables and radiation conductors could be obtained from users' input files. These files would be constructed from heat rate and view factor program output using the PTD500 interface routines. The result is an effective linking of these two phases of the overall thermal analysis, eliminating much of the routine user data handling.

The INPUT module may also be used to edit an existing master file, deleting erroneous or unwanted data, replacing existing data, or inserting new data from cards or a users' file. For example, suppose an analysis is desired for a given model, but with several different orbital environments. A master file would be created for the basic model with the orbital heat flux tables omitted. Several copies of this file could be made, and each copy could be loaded with a different set of heat flux tables. With little additional effort required by the user, several complete models would be ready for analysis with each containing a different environment.

The function of the COMPILE module is to convert the model data input from a master file to a form suitable for efficient execution. During the compilation procedure, the network is checked for various errors and abnormal conditions, and any error that would prohibit continued execution is fixed. The output of the compilation module is the compiled data file, which is input required by the steady-state and transient modules.

A steady-state or transient solution of the network is obtained by executing the respective module and designating which compiled data file is to be used. The results of the solution may be printed directly from the operating routine, stored in the library as an output file, or used to update the current compiled data file. An updated compiled data file reflects all changes that occurred in the network during the particular solution. For example, the original temperatures would be replaced with the final set of temperatures which existed when the steady-state or transient solution was terminated. By using this option, the steady-state routine could be called to obtain starting temperatures for a transient solution, or either solution could be restarted from a previous run. The compiled data file may also be accessed by user programs to perform various operations such as calculating sink temperatures, etc.

The OUTPUT module is a collection of various programs used to distribute output from the PTD500 system. Available options in this module include standard hard-copy listings, microfilm listings, microfilm plotting, and a general interface routine used to feed programs external to the PTD500 system. An output file may also be converted to an input file to be used in constructing another model, thus enabling several models to be linked together without excessive data handling by the user.

In summary, the modular construction of the PTD500 and the extensive utilization of data files offer the following advantages.

1. Each module or phase of the system may be executed independently if the library of data files is permanent. This enables effective restart capability throughout the system, reducing computer runs and engineering time.

2. External programs may access any file in the library, enabling an effective interface to each phase of the system. Typically, this results in elimination of 90 percent of the card handling and a reduction in engineering time.

LUMPED PARAMETER FUNDAMENTALS

The PTD500 thermal analyzer, as well as most of the current programs in use today, utilizes a thermal-electrical analogy to represent the physical model. In general, the physical model is reduced to a system of capacitors and resistors, interconnected at nodal points to form an analog network. This network can be solved for a steady-state or transient solution by the program.

The network format is very attractive from the programming point of view since it requires relatively simple methods of data handling and solution techniques. The result is a minimum of program logic to obtain the actual solutions. This permits most of the computer's storage cells to be assigned to data, thus obtaining the capability to handle larger problems.

The analog network representation of a thermal model also has undesirable aspects since it is an approximation of the true physical problem. In general, all derivatives in the governing differential equations must be reduced to finite differences to obtain the solution. Reduction of the time derivatives is handled by the program and a given degree of accuracy can normally be guaranteed. In fact, at the expense of run time, a very high degree of accuracy can be achieved. However, the space derivatives are reduced to finite differences by the user, and the degree to which the mathematical model represents the desired physical model depends upon the user's skill and understanding of the problem.

The analog network model is commonly referred to as the "lumped parameter" representation since the continuous mass of the physical model is lumped into small quanta called nodes. The nodes are connected by conductors which represent lumped heat paths within the physical model. Energy can flow from high temperature nodes through the conductors to lower temperature nodes. The following problem illustrates the correspondence between the physical model and the analog network.

Consider a two-dimensional heat transfer problem in a finite slab. The slab is sectioned into nodes as indicated in Figure 1.

The rate of energy being stored by a node, at some time (t), is expressed as

$$q_{stored} = \int_V \rho C_p \frac{\partial T^t}{\partial t} dx\, dy\, dz \qquad (1)$$

where the integration is performed over the node volume in question. If the time derivative $\left(\frac{\partial T^t}{\partial t}\right)$ is assumed to be constant throughout the node, the node can be lumped into a point mass (M), and equation (1) becomes

$$q_{stored} = M C_p \frac{\partial T^t}{\partial t}$$

and

$$M = \rho \Delta x \Delta y \Delta z \quad . \qquad (2)$$

Introducing the thermal capacity (C), equation (2) becomes

$$q_{stored} = C \frac{\partial T^t}{\partial t}$$

and

$$C = M C_p \quad . \qquad (3)$$

The lumped mass is indicated as a point with a capacitor connected to ground, and is referred to as a storage node (Fig. 3).

The rate of energy flow normal to a cross-sectional area (S), is given as

$$q_n = - \int_S k \frac{\partial T}{\partial n} dS \qquad (4)$$

where the integral is taken over the area (S). If the space derivative $\left(\frac{\partial T}{\partial n}\right)$ is assumed to be constant over the surface (S), equation (4) becomes

$$q_n = - k S \frac{\partial T}{\partial n} \quad . \qquad (5)$$

Equation (5) is the heat flux rate through some cross-section (S). If this cross-sectional area is positioned between two adjacent nodes in the model, and if the space derivative $\left(\frac{\partial T}{\partial n}\right)$ is assumed to be constant over the interval between the nodes, then the heat flux rate from node i to node j can be expressed as

$$q_{ij} = - k S_{ij} \frac{(T_j - T_i)}{\Delta N_{ij}} \qquad (6)$$

where ΔN_{ij} is the distance between nodes i and j and S_{ij} is the cross-sectional area between the two nodes.

Introducing thermal conductance (G), equation (6) becomes

$$q_{ij} = G_{ij} (T_i - T_j)$$

and

$$G_{ij} = \frac{k S_{ij}}{\Delta N_{ij}} \quad . \tag{7}$$

Equation (7) is represented by a conductor in the thermal analog network, and is symbolized by a resistor in Figure 3. An energy balance can be written for each node to obtain a set of simultaneous differential equations. From equations (3) and (7),

$$C_i \frac{\partial T_i^t}{\partial t} = \sum_j^n G_{ij} (T_j - T_i) \tag{8}$$

where node (i) is connected to nodes (j = 1, --n) via conductors G_{ij}.

The method of solving this set of equations (8) is discussed in sections titled STEADY-STATE SOLUTION and TRANSIENT SOLUTION.

In summary, the following assumptions were made in constructing the network model.

1. The time derivative $\left(\frac{\partial T^t}{\partial t}\right)$ is constant throughout the storage node.

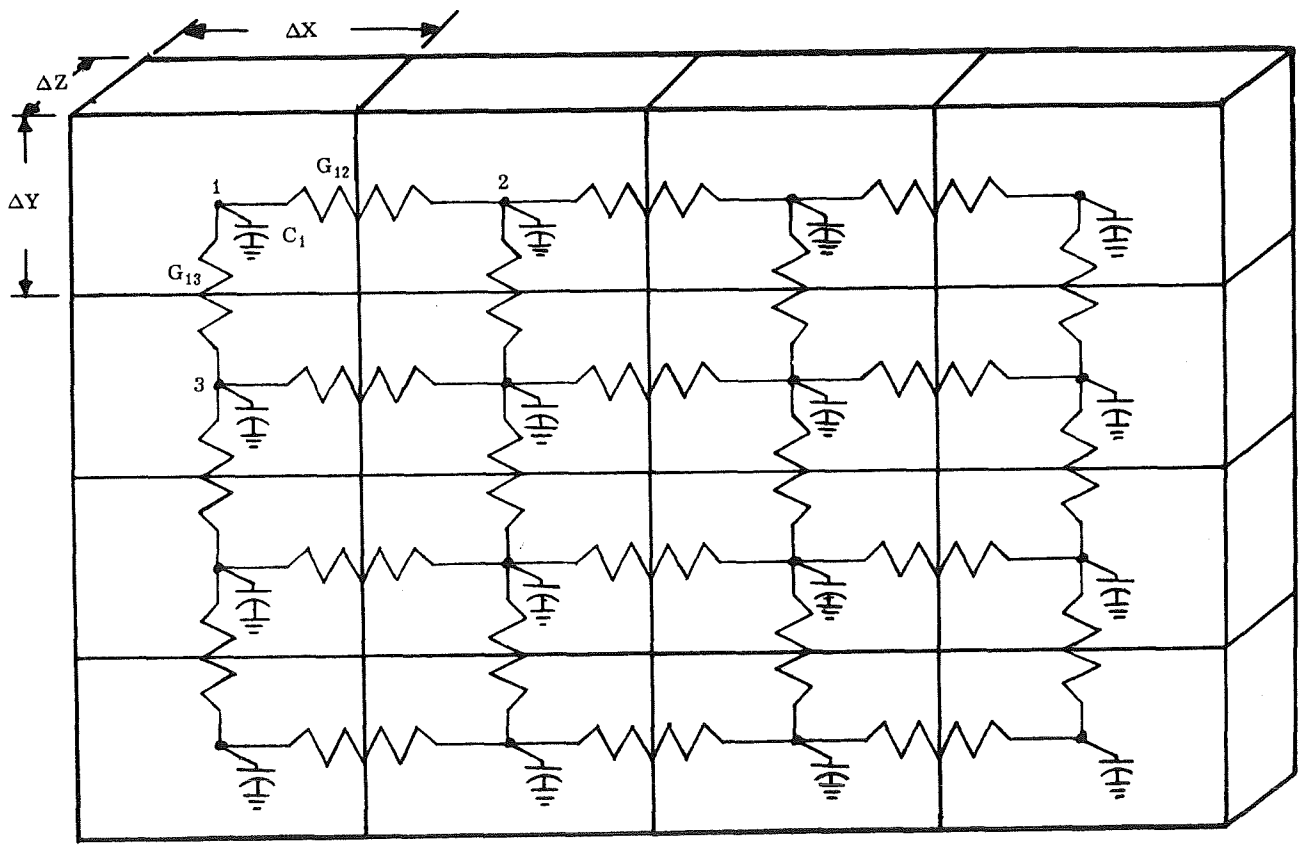

FIGURE 3. LUMPED PARAMETER REPRESENTATION

2. The space derivative $\left(\frac{\partial T}{\partial n}\right)$ is constant everywhere in the region between two adjoining nodes.

It is evident that as the node size becomes smaller, the approximate model approaches the true physical problem. The engineer must choose an optimum node size that will result in a fairly accurate model without using excessive nodes.

NETWORK ELEMENTS

The PTD500 offers the following elements which can be utilized in constructing a network.

Storage Node (constant or variable capacitance)

Dummy Node

Boundary Node (constant or variable temperature)

Conductor (constant or variable)

Resistor (constant or variable)

Radiation Connector

One-Way Conductor (constant or variable)

One-Way Resistor (constant or variable)

Source Element (constant or variable)

Time Tables

Sequential Tables

General Tables

The storage node and the conductor were discussed in the previous section. Other elements are discussed below.

A resistor is the same as a conductor; however, the numerical values are inversely related; i.e.,

$$R_{ij} = \frac{1}{G_{ij}} \quad . \tag{9}$$

The dummy node is included as an aid to network construction and to monitor temperatures between the storage nodes. A dummy node has no storage capability and serves merely as a connecting point in the network. Dummy nodes always receive steady-state solutions.

Boundary nodes provide a means of creating network boundary conditions. These nodes serve as network connecting points which have temperature histories specified by the user.

The source element is used to impress a constant or time-dependent energy function at any storage or dummy node. The normal source element application is to simulate internal heat generation or absorbed heat flux. The variable source elements automatically generate the necessary logic for interpolation and averaging during solution, thus eliminating the user's input of logic which is inherent in other analyzers.

The one-way conductor and one-way resistor are included for fluid flow problems. The one-way conductor enters into the temperature calculation of only one adjoining node, normally the downstream node.

The radiation connector is used to obtain the fourth order radiation exchange between nodes. This element is discussed in detail in the section titled INFRARED RADIATION.

The time, sequential, and general tables are used to input the data tables referenced by variable elements. These tables are checked for correct form during input to eliminate interpolation errors during execution of the solution modules.

The elements listed above are all standard input for the PTD500 thermal analyzer. If a problem is encountered where special elements are required, they can usually be synthesized from the standard set using FORTRAN subroutines patched into the PTD500 solution routines. An interface package is available for including user-written subroutines in the solution sequence with access to all program variables. In this manner, special elements such as thermal control systems, etc., can easily be included in the network.

DIAGNOSTICS

A significant number of input errors routinely result from the large amount of input data required by the large radiation-dominated models. This requires successive runs to completely detect and correct all the erroneous data, thus resulting in excessive computer and engineering time required to obtain the final solution. The ability of the PTD500 to interface with other programs substantially reduces this problem since the input data are obtained directly from the other programs, eliminating the possibility of user errors. To further reduce the problem of input errors, the PTD500 was designed with the following characteristics.

1. Restrictions on format and input sequence were minimized to reduce the number of possible error conditions.

2. Extensive error checking is included in the compile module to warn of abnormal conditions.

3. Error 'Fix' procedures are included to allow continued execution when errors are encountered, enabling more errors to be detected in a given run.

4. Graphical network hook-up display is available, which provides a pictorial representation of network data on microfilm plots.

Card input consists of a label used to identify the data, followed by the actual numerical data. There are no format restrictions on card input, other than the sequence in which the information must appear on the card. Otherwise, the user is free to punch the card in any manner he chooses. It is felt that this feature, available in other analyzers to a much lesser degree, will eliminate many errors and thus eliminate wasted time caused by data starting in the wrong column, missing commas, or other violations of the various format restrictions. Labels must be spelled correctly for proper identification. For this reason, the correspondence between labels and the elements they identify was made to be as evident as possible. However, if the card processor does encounter an invalid label caused by misspelling or keypunch errors, then the library of valid labels is scanned for the closest match to the erroneous label. If a reasonably close match is found, then that label is assumed, and the substitution is noted to the user. Otherwise, the card is flagged as an error. All erroneous data are included in the master file and can subsequently be deleted or replaced by the collector. In a further effort to reduce the possible errors that the user can commit, as few restrictions as possible were placed on the overall sequence of data. To prevent excessive data compilation time, the input must be grouped into three logical groups or blocks of data, but other than this restriction, the sequence of data is arbitrary. For example, all conductors, resistors, and radiation connectors, which compose one of the three major blocks of data, may appear in any order desired.

The error detection and error fix sections function together to produce a mathematically valid network suitable for solution. The compile module ignores any erroneous data on the master file that was flagged by the input module, and considers only the valid information. This information is then scanned for network errors. This includes checks for illegal connections between elements, missing elements, abnormal element values, unused elements, discontinuous networks, and various other network violations. Any condition that would prohibit solution of the network is fixed, and the results are output as a compiled data file. The fix procedures are a set of prescribed alternatives for each possible error condition. For example, if a connector is encountered that references a nonexistent node, the connector is deleted from the network and execution continues. The purpose of the error fix procedures is to allow continued execution to search for additional errors, and to possibly salvage the solution of a large model that contains a few minor errors. Various controls are available to the user to abort execution if a given number of errors is exceeded.

INFRARED RADIATION

Radiation exchange is a complex problem in thermal analyses since determination of view factors, reflection, and blockages is a difficult task. However, these calculations are normally performed by a separate view factor program, and the resulting radiation constant (RAD) or script f form factor is input to the thermal analyzer.

The governing equation for radiation exchange between nodes i and j can be reduced to

$$q_{ij} = \sigma f_{ij} (T_i^4 - T_j^4) \quad , \tag{10}$$

$$q_{ij} = RAD_{ij} (T_i^4 - T_j^4) \tag{11}$$

$$RAD_{ij} = \sigma f_{ij}$$

In general, there is no direct analogy for radiation exchange in the analog network. However, a temperature-dependent conductor can be made to simulate radiation transfer by reducing the fourth order radiation equation to a linear temperature-dependent equation. This is accomplished by multiplying and dividing the left side of equation (11) by the linear temperature difference as follows:

$$q_{ij} = RAD_{ij} (T_i^4 - T_j^4) (T_i - T_j)/(T_i - T_j) \tag{12}$$

$$q_{ij} = RAD_{ij} (T_i^2 + T_j^2) (T_i + T_j)/(T_i - T_j)$$

Introducing the linear radiation conductor Gr, equation (12) can be rewritten as

$$q_{ij} = Gr_{ij} (T_i - T_j) \tag{13}$$

and

$$Gr_{ij} = RAD_{ij} (T_i^2 + T_j^2) (T_i + T_j) \quad . \tag{14}$$

The linear radiation conductor can be treated as a standard conductor. However, after each iteration or time step, the radiation conductors must be re-calculated to reflect the temperature change of the connecting nodes.

This method is incorporated by most current thermal analyzers and introduces no additional error in the transient solution if forward differencing is used.

In a radiation-dominated problem, several disadvantages imposed by the use of linearized radiation conductors are as follows:

1. Steady-state convergence is prolonged since fourth order effects are not included in the solution of the heat balance equation.

2. In most cases, storage cells are required for both radiation constants (RAD) and linear radiation conductors (Gr).

3. Excessive time is consumed by calculating the linear radiation conductor after each iteration or time step.

For these reasons, the PTD500 treats radiation conductors as a separate distinct element of the network. The fourth order temperature equation appears in the solution of the heat balance equation, and storage is required only for the radiation constant (RAD). The linear radiation conductor concept is used to determine stability criteria for transient solutions, but it does not appear as a network element.

STEADY-STATE SOLUTION

A steady-state solution is defined as the equilibrium state of the model, when no time varying properties or forcing functions are present in the network. A steady-state solution allows the user to determine the final equilibrium state of his model, if one exists. For problems where no final state exists, such as the cyclic temperature history normally encountered with orbiting space vehicles, the steady-state solution can be used to obtain a starting point for cyclic transient analysis.

The steady-state solution is obtained by solving the simultaneous set of heat balance equations with all time derivatives set to zero.

Setting the right side of equation (8) equal to zero, and adding radiation and source terms, the steady-state equations are

$$0 = \sum_i G_{in} (T_i - T_n) + \sum_j RAD_{jn} (T_j^4 - T_n^4) + \sum q_{const} \tag{15}$$

where the subscript n represents the node in question. Solving equation (15) for T_n yields

$$T_n^4 \sum_j RAD_{jn} + T_n \sum_i G_{in} = \sum G_{in} T_i + \sum RAD_{jn} T_j^4 + \sum q_{const} \quad . \quad (16)$$

Equation (16) is solved using Newton's method of tangents, an iteration process, and convergence to T_n is normally very rapid.

The network is relaxed to its equilibrium state by the block iteration method. This method consists of solving equation (16) for each node and replacing the old node temperature with the new calculated node temperature. One pass through the network is termed an iteration, and the iteration process is continued until the temperature difference between successive iterations is less than some preset minimum. Because of fourth power effects of radiation conductors, successive iterations will often create oscillations. In some cases, the entire network may become unstable, resulting in a diverging solution. The most common method of preventing divergence is to apply a dampening factor to the block iteration process. This is accomplished by limiting the change in temperature between two successive iterations to some fraction of the calculated change. Most networks can be made to converge in this manner at the expense of an increased number of iterations (extended run time). Furthermore, the dampening required must usually be determined by the user and supplied as input. A more desirable method would allow the program to detect divergence and take corrective action to return the network to stable conditions. The PTD500 has this capability. The PTD500 records the latest three consecutive iterations for each node in a push-down register. As each new temperature is calculated, it is compared with the three previous temperatures to determine any trend. If oscillations are detected, the new temperature is equated to the average temperature about which the oscillation is occurring. If no oscillations are present, and if the temperatures appear to be converging, then a limited extrapolation is applied to accelerate convergence. The resulting new temperature is stored in the register, pushing out the oldest value and leaving the three latest consecutive temperatures for the next iteration. This technique has proved to be successful when applied to networks which cannot be resolved by successive iteration solutions. Solutions have been achieved with 50 percent fewer iterations than are required by the damped relaxation method.

As mentioned above, the normal criterion for convergence is a preset temperature tolerance between iterations. However, some networks which do not have well defined boundary conditions may meet a reasonably low-temperature tolerance and still not be in equilibrium. The PTD500 steady-state solution performs an overall heat balance on the network after the temperature tolerance is met to detect this condition. If the imbalance of the network $(Q_{in} - Q_{out})$ is greater than a present tolerance, the temperature tolerance is lowered and the relaxation routine is continued until convergences to both tolerances are met.

If the steady-state solution is being employed to find starting temperatures for a subsequent transient solution, the time-varying network elements must be replaced with a constant value to obtain the steady-state solution. The PTD500 locates all variable source terms and boundary nodes, and evaluates them at a given time, or averages them over a given time interval, whichever is desired. If a variable boundary node is connected to the network via radiation conductors, a fourth power average is used for that node. These values are used in the steady-state solution.

TRANSIENT SOLUTION

The main objective of any thermal analyzer is to obtain the transient-temperature solution of a problem. All other program functions either prepare the network for solution or process output from the transient analysis. Thus the transient routines emerge as the most important portion of the analyzer.

Many methods have been used to obtain transient solutions having wide ranges of accuracy and stability. The most accurate methods, i.e., those which are of interest here, are the finite difference solutions.

By adding the radiation and source terms to equation (8), the complete storage node heat-balance equation is obtained; i.e.,

$$C_n \frac{dT_n}{dt} = \sum_i G_{in} (T_i - T_n) + \sum_j RAD_{jn} (T_j^4 - T_n^4) + \sum q(t) \ . \tag{17}$$

For equation (17) to be useful, the time derivative $\frac{dT_n}{dt}$ must be reduced to a finite difference. This is accomplished by considering the Taylor series of T_n; i.e.,

$$T_n^{t+\Delta t} = T_n^t + \Delta t \frac{dT_n^t}{dt} + \frac{\Delta t^2}{2!} \frac{d^2T_n^t}{dt} + \dots \ . \tag{18}$$

Disregarding the higher order derivatives, a finite difference equation can be obtained from equation (18) as follows:

$$T_n^{t+\Delta t} \approx T_n^t + \Delta t \frac{dT_n^t}{dt} \tag{19}$$

$$\frac{T_n^{t+\Delta t} - T_n^t}{\Delta t} \approx \frac{dT_n^t}{dt} \ .$$

A positive value of Δt gives a forward difference equation, and a negative value of Δt produces the backward difference equation. The two can also be combined to give a backward-forward difference equation. The backward and backward-forward difference equations can tolerate larger time steps than the forward difference equation; however, they produce a set of implicit equations which must be iterated at each time step to obtain a solution. This disadvantage offsets any advantage gained from the larger time step. The PTD500 employs the simpler forward-difference solution. Replacing the left side of equation (17) with its forward-difference equivalent, equation (19), and rearranging terms yields

$$T_n^{t+\Delta t} = T_n^t + \left[\sum_i G_{in} (T_i^t - T_n^t) + \sum_j RAD_{jn} \left(T_j^{t^4} - T_n^{t^4} \right) + \sum q(t) \right] \frac{\Delta t}{C_n} \ . \tag{20}$$

Equation (20) is inherently unstable for large time steps since the new temperature is a linear extrapolation from the old temperature, based on the time rate of change of the old temperature. Therefore, a stability criterion must be established to prevent an unstable solution caused by a large time step.

A physical analysis of the method of solution would be helpful at this point to illustrate the cause of instability. Consider the process for advancing one time step, from time, t, to time, $t + \Delta t$. At time t, all network temperatures are known. Furthermore, the majority of the network nodes are assumed to be in a state of imbalance, that is, the network is not in a steady-state condition. By considering one particular node, the time rate of temperature change for that node can be calculated based on the surrounding nodal temperatures and the heat source term, if any exist. This time derivative is then multiplied by a finite time step, and the resulting change in temperature is added to the original temperature at time t. The new temperature obtained is obviously closer to the steady-state condition for that node, based on the node environment calculated at time t. The larger the time step, the closer the new temperature is to the original steady-state condition. The time step which allows the node to exactly reach its steady-state value is considered to be the maximum compute interval allowed, since a larger interval would put the node past its steady-state condition. Often an overshoot of this type may not be harmful if it does not pass the next steady-state condition at time $t + \Delta t$. This situation, in general, cannot be guaranteed without using an iteration process between the two time positions, which is similar to the backward-forward method discussed earlier.

The maximum compute interval can mathematically be determined by examining the transient forward-difference equation and solving for the time step required to reduce this equation to a steady-state solution. For simplicity, consider equation (20) with the radiation terms omitted. Rearranging the right side,

$$T_n^{t+\Delta t} = T_n^t - T_n^t \left(\frac{\sum G_{in}}{C_n} \right) \Delta t + \left(\frac{1}{C_n} \sum_i G_{in} T_i^t + \frac{1}{C_n} \sum q(t) \right) \Delta t \tag{21}$$

$$\Delta t = \frac{d_n}{\sum G_{in}} \tag{22}$$

$$T_n^{t+\Delta t} = \frac{\sum G_{in} T_i + \sum q(t)}{\sum G_{in}} \tag{23}$$

For the time step given in equation (22), equation (21) reduces to the steady-state equation (23).

To assure stability, the compute interval must not be larger than β_{min}, where β_{min} is defined as:

$$\beta_{min} = \left(\frac{C_n}{\sum G_{in}} \right)_{min} \tag{24}$$

When radiation is included, the value of Δt that produces a steady-state solution cannot be determined unless an iteration process is used. Therefore, radiation conductors are linearized (in the discussion on INFRARED RADIATION) to determine the maximum compute interval. Replacing the radiation terms in equation (20) with the linearized radiation conductors, equations (13) and (14) and rearranging terms will give

$$T_n^{t+\Delta t} = T_n^t - T_n^t \left(\frac{\sum G_{in}}{C_n} + \frac{\sum Gr_{in}}{C_n} \right) \Delta t + \left(\frac{1}{C_n} \sum G_{in} T_i + \frac{1}{C_n} \sum Gr_{in} + \frac{1}{C_n} \sum q(t) \right) \Delta t \tag{25}$$

For the time step given in equation (26), equation (25) reduces to the approximate steady-state equation (27),

$$\Delta t = \frac{C_n}{\sum G_{in} + \sum Gr_{jn}} \tag{26}$$

and

$$T_n^{t+\Delta t} = \frac{\sum G_{in} T_i + \sum Gr_{jn} T_j + \sum q(t)}{\sum G_{in} + \sum Gr_{jn}} \tag{27}$$

The stability criteria with radiation included is thus given by equation (28),

$$\beta_{min} = \left(\frac{C_n}{\sum G_{in} + \sum Gr_{jn}} \right)_{min} \tag{28}$$

It should be noted at this point that stability does not imply accuracy. If a solution is stable, it can be assumed that round-off errors caused by finite difference are not cumulative. However, the accuracy is unknown. If the compute interval is reduced, a more accurate solution obviously would result; however, unless several solutions with varying compute intervals are compared, the maximum time step for a given accuracy would be a guess at the most.

It would be desirable for the program to estimate the degree of accuracy during the solution and subsequently adjust the compute interval to hold the error within a given tolerance. By considering again the Taylor series used to derive the finite difference equation, it can be seen that the round-off error is represented by the higher order terms which were disregarded,

$$T_n^{t+\Delta t} = T_n^t + \frac{dT_n^t}{dt} \Delta t + \underbrace{\frac{d^2T_n^t}{dt^2} \frac{\Delta t^2}{2} + \ldots}_{\text{Round-Off Error}} \tag{29}$$

and

$$\frac{dT_n^t}{dt} = \frac{1}{C_n} q_{net}^t$$

If the net heat rate $\left(q_{net}^t \right)$ remains constant during the compute interval, there is no error in the time derivative. However, the net heat rate can hardly be expected to remain constant since temperatures of the adjoining nodes are changing. Time varying source elements, which are normally included in the network, must also be considered. The PTD500 transient routine calculates the third term of the Taylor series $\left(\frac{d^2T_n^t}{dt^2} \frac{\Delta t^2}{2} \right)$ for each

node to control the error in the time derivative. The compute interval is adjusted, if necessary, to assure that the third term is less than a preset limit. This term is also included in the solution to increase the accuracy of the time derivative. The method cannot guarantee the accuracy of any one compute interval since the magnitude of the remaining terms in the Taylor series cannot be predicted. However, if the stability criteria are met at each compute interval, studies have shown that the resulting solution is well behaved, and the higher order time derivatives rapidly converge to zero. If a high order derivative does become large, it will cause the third term to grow, eventually causing an adjustment in the compute interval.

CONCLUSION

Figure 4 is a summary of the major problems encountered using existing thermal analyzers for large radiation-dominated thermal problems, and the capabilities offered by the PTD500 to alleviate these problems. Figure 5 illustrates the capacity of the PTD500 for a typical radiation-dominated problem. The expanded capability of the PTD500 offers an analytical environment adequate for the thermal design of existing and foreseeable spacecraft.

PROBLEMS	EXISTING THERMAL ANALYZERS	PTD500
1. LARGE MATH MODELS	EXCEED MACHINE CAPABILITY	SIZE CAPABILITY INCREASED 200 - 500%
2. LENGTHY INPUT DATA PREPARATION	EXCESSIVE CARD HANDLING	INPUT DATA MECHANIZED CARDS REDUCED 90%
3. LOST TIME (ERRORS)	SUCCESSIVE CHECK-OUT RUNS	COMPLETE ERROR DIAGNOSTICS

FIGURE 4. PTD500 CAPABILITIES

- BASELINE

  HEAT FLUX ON 60% OF NODES
  AVERAGE OF 36 CONNECTIONS TO NODE

- CAPACITY WITH 65K STORAGE

  1,000 NODES
  600 HEAT FLUX TABLES (12,000 ENTRIES)
  18,000 CONNECTORS (CONDUCTION, RADIATION, ETC.)

- CAPACITY WITH 65K STORAGE – DATA OVERLAY

  2,500 NODES
  1,500 HEAT FLUX TABLES (30,000 ENTRIES)
  45,000 CONNECTORS (5 OVERLAYS)

FIGURE 5. PTD500 CAPACITY

THERMAL SIMILITUDE

By

Jimmy R. Watkins

SUMMARY

Previous inhouse analytical and contractual experimental work in thermal similitude is mentioned briefly. Results are presented of recent experiments performed under research contract with the Lockheed Palo Alto Research Laboratory on thermal and structural modeling of a 2-meter-aperture Optical Technology Apollo Extension System (OTES) telescope.

The overall results indicate that thermal and structural modeling of large space telescope systems is a procedure that can be used to provide useful information on the flight performance of the prototype system.

INTRODUCTION

Thermal similitude is the term used to refer to the analytical and experimental effort in thermal scale modeling. In order to perform scale modeling experiments, scaling laws are needed to direct and control the experiments to obtain intelligible data on the model for predicting the behavior of the prototype. Earlier work was concerned with derivation and verification of scaling laws for thermal modeling of certain general configurations [1-5]. Subsequent work concerned investigation of the more complex thermal and structural behavior of a large-aperture space telescope. This paper is a summary of the experimental work on thermal and structural modeling of a 2-meter-aperture space telescope performed under research contract with the Lockheed Palo Alto Research Laboratory [6].

CONTRACTUAL EXPERIMENTAL EFFORT

PROTOTYPE AND MODEL DEFINITION

The proposed 2-meter-aperture OTES telescope was chosen as the prototype for the thermal and structural modeling effort. Figure 1 shows the 2-meter OTES concept. The telescope has a 2-meter diameter quartz primary mirror. The system provides a Cassegrainian f/3 parabolic telescope. The secondary mirror is supported by three quartz rods and is approximately 4.76 meters from the primary mirror. The telescope barrel consists of one plastic honeycomb cylinder at the barrel opening on which a sun shutter is mounted, and five multilayer insulated aluminum honeycomb cylinders in addition to the manned support section. The prototype has an overall length of 12 meters and a tube aperture of 2.38 meters.

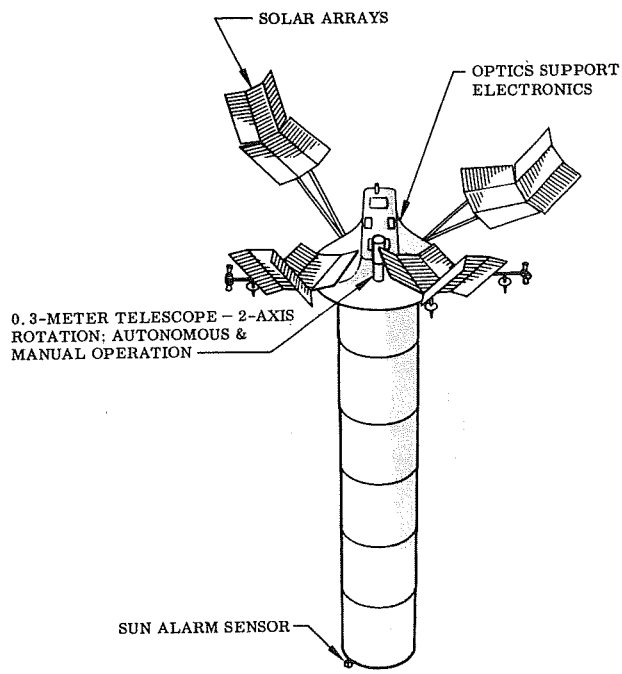

FIGURE 1. TWO-METER OTES CONCEPT

Optimum performance of the prototype requires minimal thermal gradients in the optics, particularly in the primary mirror segments; elimination of thermal transients caused by varying heat inputs; and an average steady-state temperature near the inversion point of the thermal expansion of fused

quartz. Based on the telescope system's conceptual design and operational requirements, a mathematical model was established for the purpose of predicting the space thermal behavior of the prototype system. It was assumed that the telescope would be placed in a 24-hour synchronous orbit and be utilized in an earth-oriented optical axis configuration as shown in Figure 2, where β is the angle between the orbit plane and the solar vector.

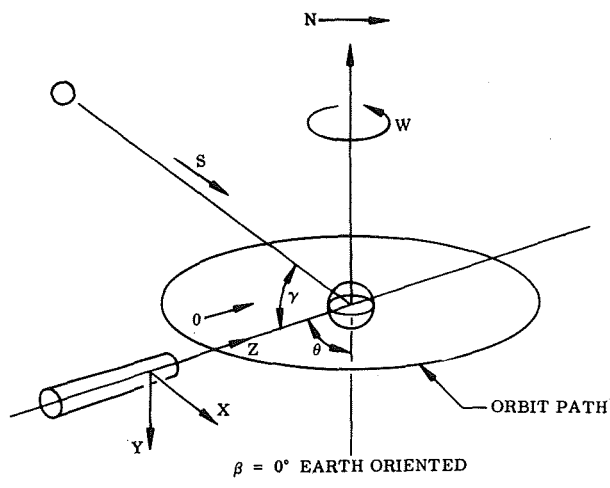

FIGURE 2. ORBIT CONFIGURATION

The design of the telescope model required the use of both thermal and structural modeling criteria. The criteria used for thermal modeling in a radiation-conduction-coupled space-thermal environment are given as follows:

$$\frac{\rho^* V^* C^* T^*}{\theta^*} = A_I^* I^* = Q^* = \frac{K^* A_n^* T^*}{L^*}$$

$$= A_i^* T^{*4} \quad ,$$

where the starred quantities are ratios of properties between the model, m, and prototype, p, at geometrically similar points. The symbols are defined as:

$\rho^* = \rho_m/\rho_p$ = density ratio

$C^* = C_m/C_p$ = specific heat ratio

$V^* = V_m/V_p$ = volume ratio

$\theta^* = \theta_m/\theta_p$ = time ratio

$K^* = K_m/K_p$ = conductivity ratio

$L^* = L_m/L_p$ = length ratio

$A_I^* = A_{I_m}/A_{I_p}$ = area ratio for areas receiving radiation from external sources

$A_n^* = A_{n_m}/A_{n_p}$ = area ratio for areas perpendicular to conduction path

$A_i^* = A_{i_m}/A_{i_p}$ = area ratio for areas interchanging radiant energy

$T^* = T_m/T_p$ = absolute temperature ratio

$Q^* = Q_m/Q_p$ = ratio of rate of energy dissipation within the model and prototype

$I^* = I_m/I_p$ = intensity ratio of external sources of radiant energy

The criteria that must be satisfied for proper modeling of the structural behavior of the telescope system whose performance is closely related to thermal stresses are given in Table I, where σ^*, e^*, E^*, α^*, and ΔT^* are ratios between model and prototype for stress, strain, Young's Modulus, coefficient of thermal expansion, and temperature change in element from reference temperature, respectively.

TABLE I. STRUCTURAL SCALING LAWS

Effect	Scaling Law
Forces: $F \propto \sigma A$	$F^* = \sigma^* L^{*2} = E^* L^{*2} \alpha^* (\Delta T)^*$
Moments: $M \alpha \sigma A L$	$M^* = \sigma^* L^{*3} = E^* L^{*3} \alpha^* (\Delta T)^*$
Linear Distortions:	$y^* = e^* L^* = L^* \alpha^* (\Delta T)^*$
Angular Distortions:	$\theta^* = e^* L^* = (\sigma^* L^* / E^*) = L^* \alpha^* (\Delta T)^*$

By using the thermal and structural modeling criteria, the design of the model was accomplished within the constraints imposed by size of test chamber, availability of materials, and maximum allowable operating temperatures for materials used

as insulation. Figure 3 shows the geometry for the 1/6.43 scale model. The primary mirror was made of pyrex. Pyrex tubing was used for the secondary support rods since it was necessary to have a material with a large coefficient of thermal expansion so that thermal strain could be determined directly in addition to furnishing the desired structural rigidity. Through an extensive experimental program, it was determined that the 1.27-cm thick blanket of multilayer insulation with a layer density of 28.3 layers/cm could be modeled with a blanket 0.457-cm thick having the same layer density. The model was tested at a temperature ratio of $T^* = T_m/T_p = 1.86$ and a time ratio of $\theta^* = \theta_m/\theta_p = 1/26$.

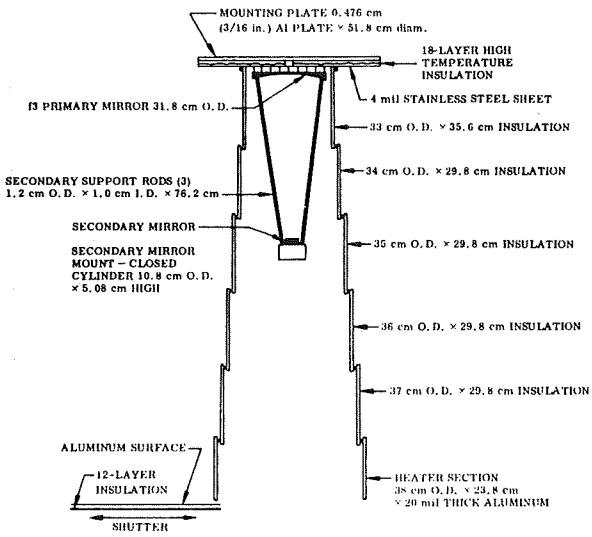

FIGURE 3. GEOMETRY OF THE MODEL

Instrumentation of the telescope model included 73 3-mil-diameter copper-constantan thermocouples for measurement of the thermal response, and 3 linear distortion gages in the pyrex secondary support rods for measurement of the structural behavior. The thermocouple (T.C.) locations for the telescope system are shown in Figures 4 and 5.

Figure 6 shows the optical system installed in the chamber. The complete assembled telescope system is shown in Figure 7 as it appeared before testing. Banks of tungsten filament lamps were automatically programmed to provide modeled skin transient temperatures in accordance with the analytical predictions.

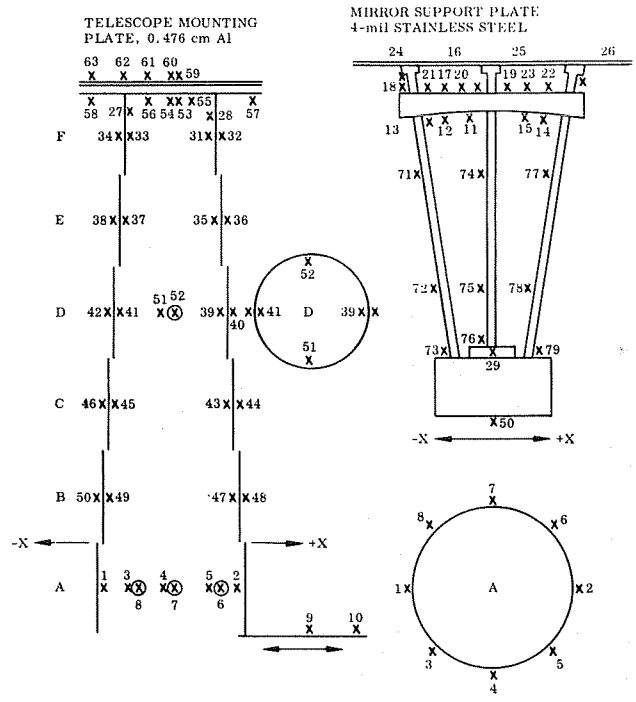

FIGURE 4. THERMOCOUPLE LOCATIONS ON THE MODEL

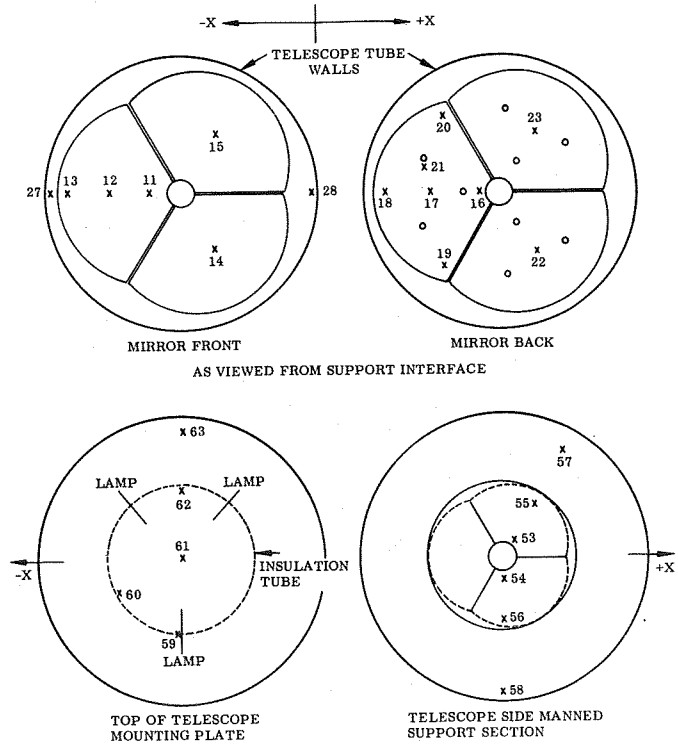

FIGURE 5. PRIMARY MIRROR THERMOCOUPLES

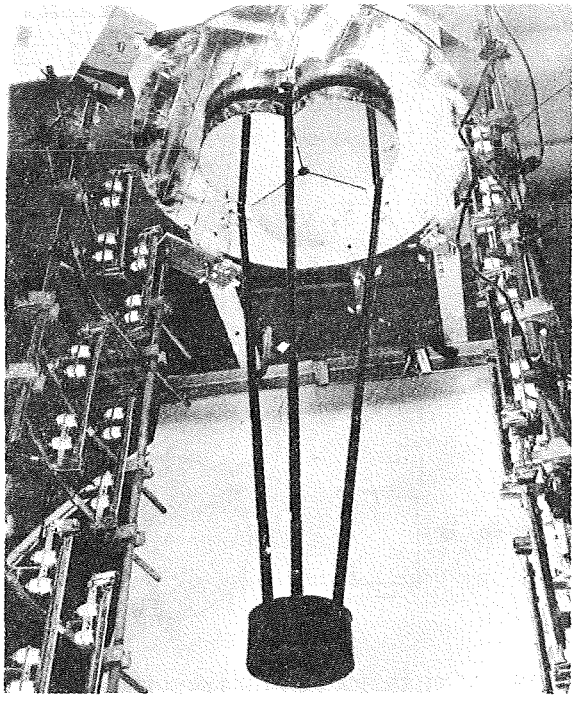

FIGURE 6. ASSEMBLED OPTICAL SYSTEM

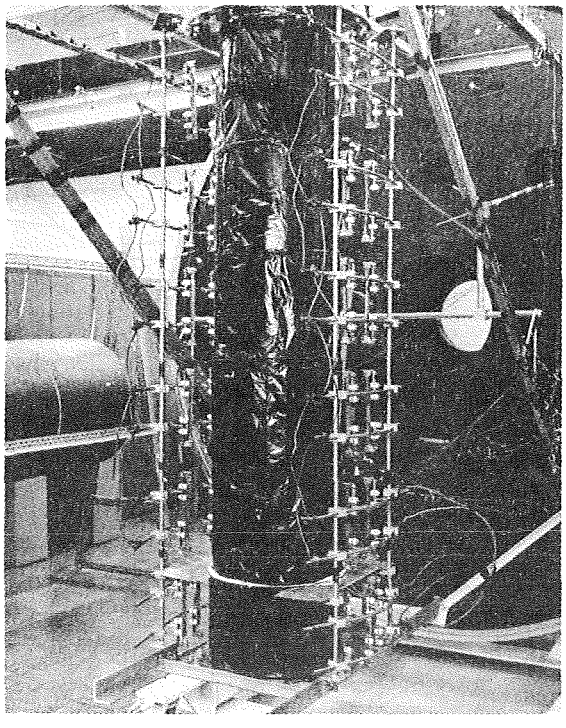

FIGURE 7. ASSEMBLED MODEL BEFORE TESTING

EXPERIMENTAL RESULTS

Prototype temperature-time curves for Section A are shown in Figure 8. The points indicate experimental results, and the curves show the required levels as dictated by the analytical study. The data points show that the required temperature history for Section A was provided except for the +x side where the maximum value was not achieved as a result of insufficient lamp power.

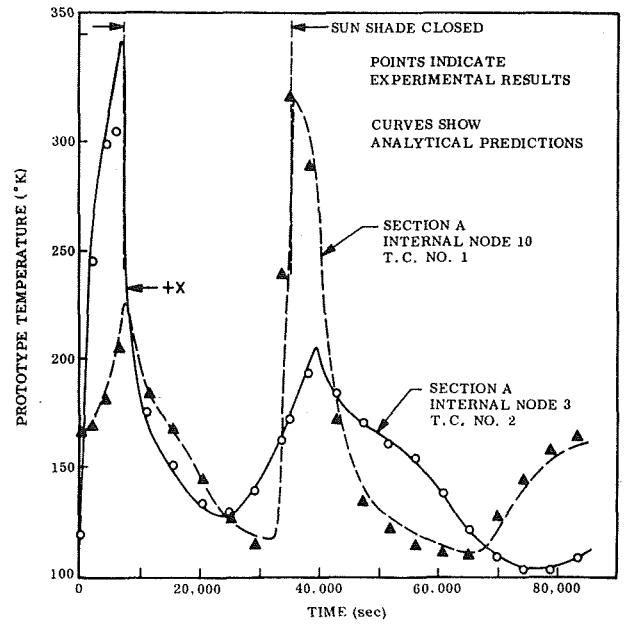

FIGURE 8. TRANSIENT THERMAL BEHAVIOR, SECTION A

The internal temperature-time curves for Sections B, C, and D are presented in Figures 9 through 11, where the model predictions for the prototype are compared to analytical predictions for the prototype. These curves show that the model-predicted average internal temperature levels were approximately 25° K lower than the analytically predicted levels. Transient variation about the mean displayed similar maximum-to-minimum differences, although the response of model internal surfaces was somewhat faster than that predicted analytically.

The transient behavior of the primary mirror and surrounding area is shown in Figure 12. The temperature of the primary mirror is between that of the manned support interface and the average tube temperature, being closer to that of the tube and remaining at an essentially constant level. Figures 9 through 12 show an increase in average temperature for tube sections closer to the primary mirror.

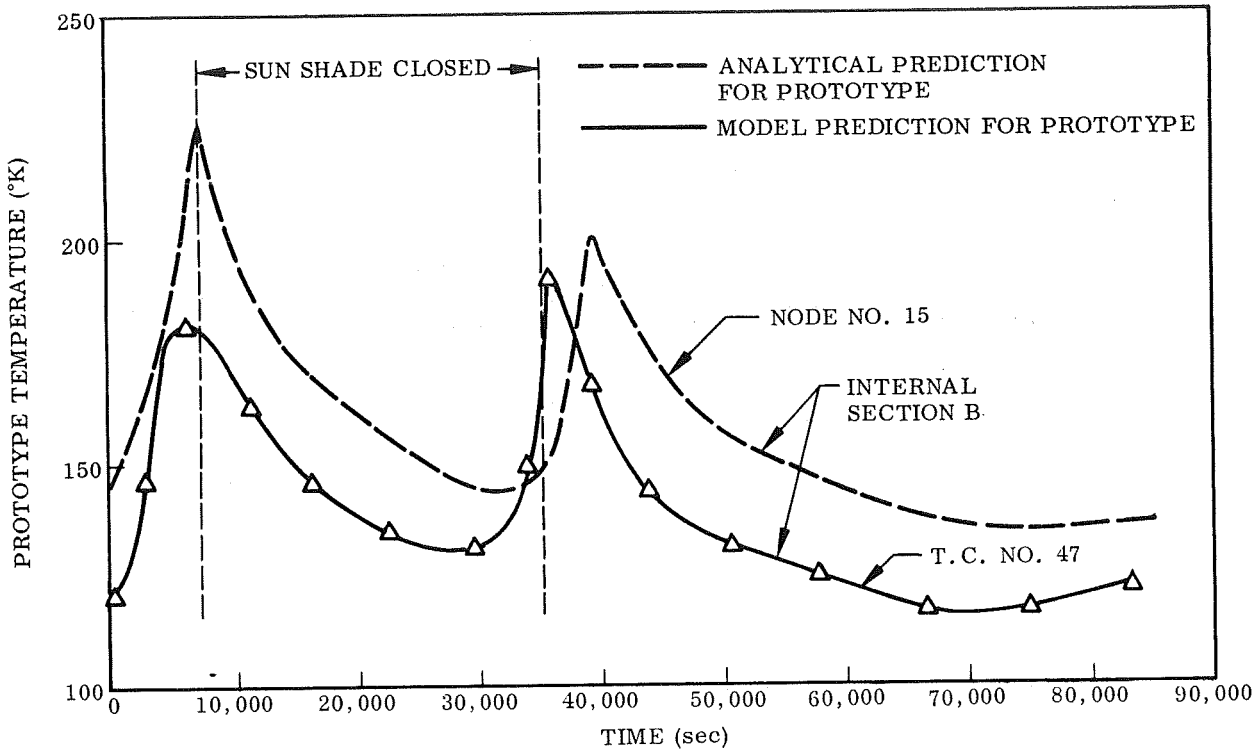

FIGURE 9. TRANSIENT THERMAL BEHAVIOR, SECTION B

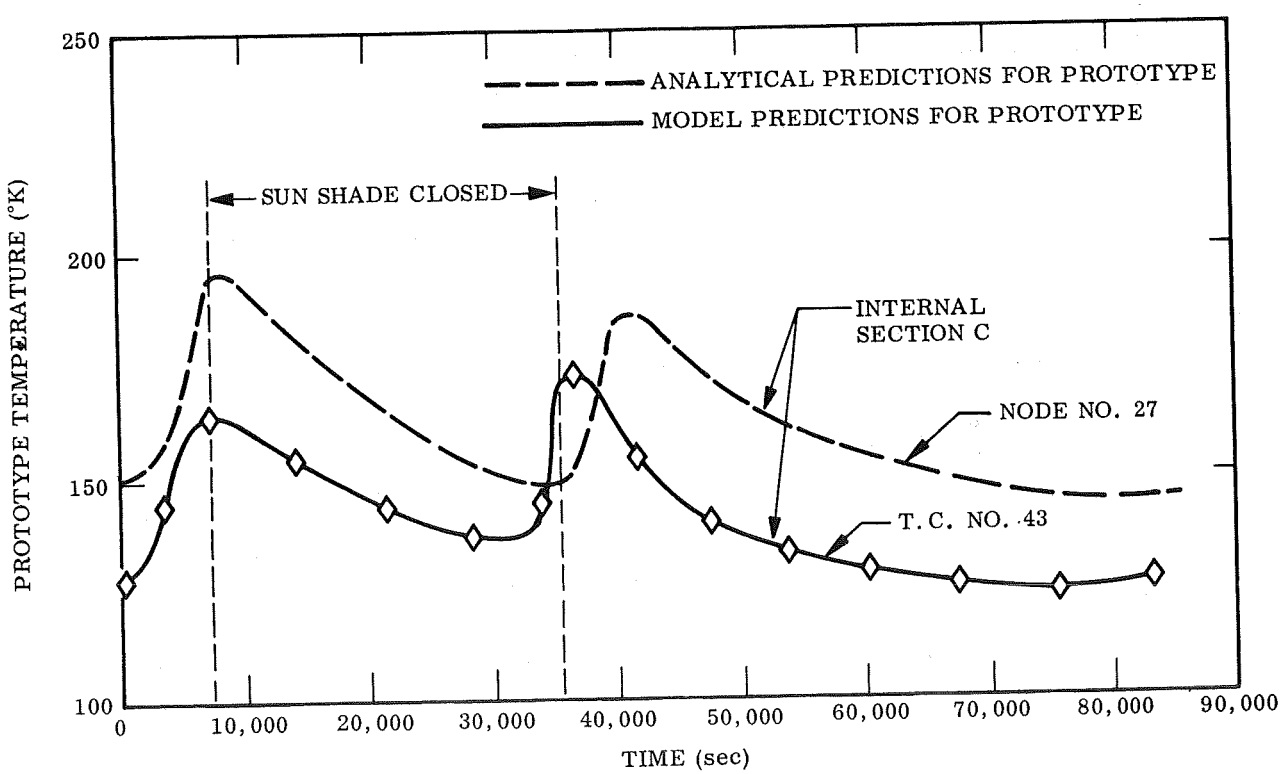

FIGURE 10. TRANSIENT THERMAL BEHAVIOR, SECTION C

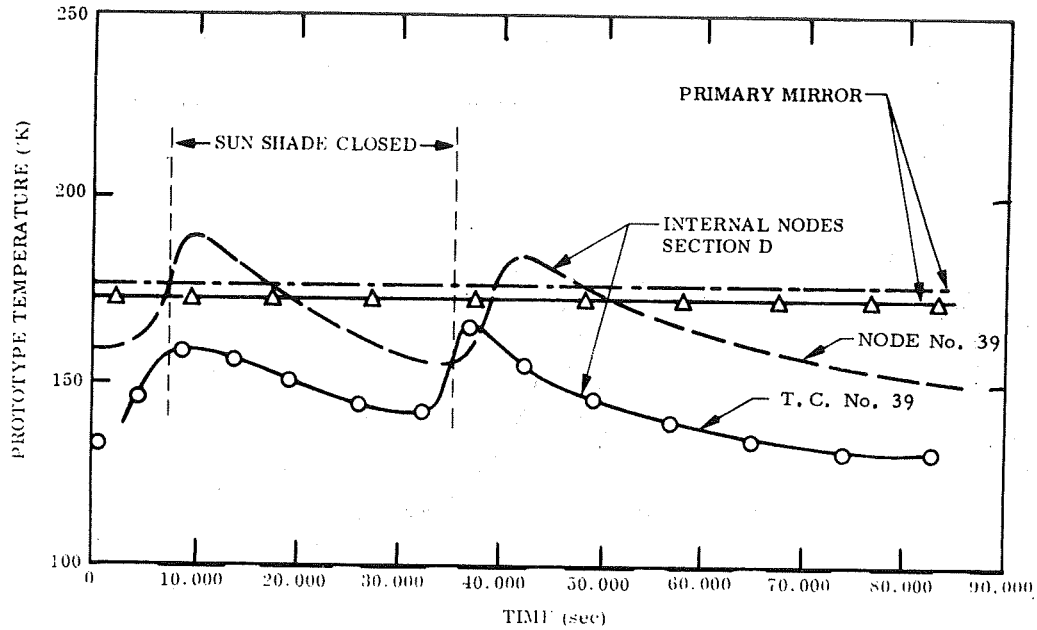

FIGURE 11. TRANSIENT THERMAL BEHAVIOR, SECTION D AND PRIMARY MIRROR

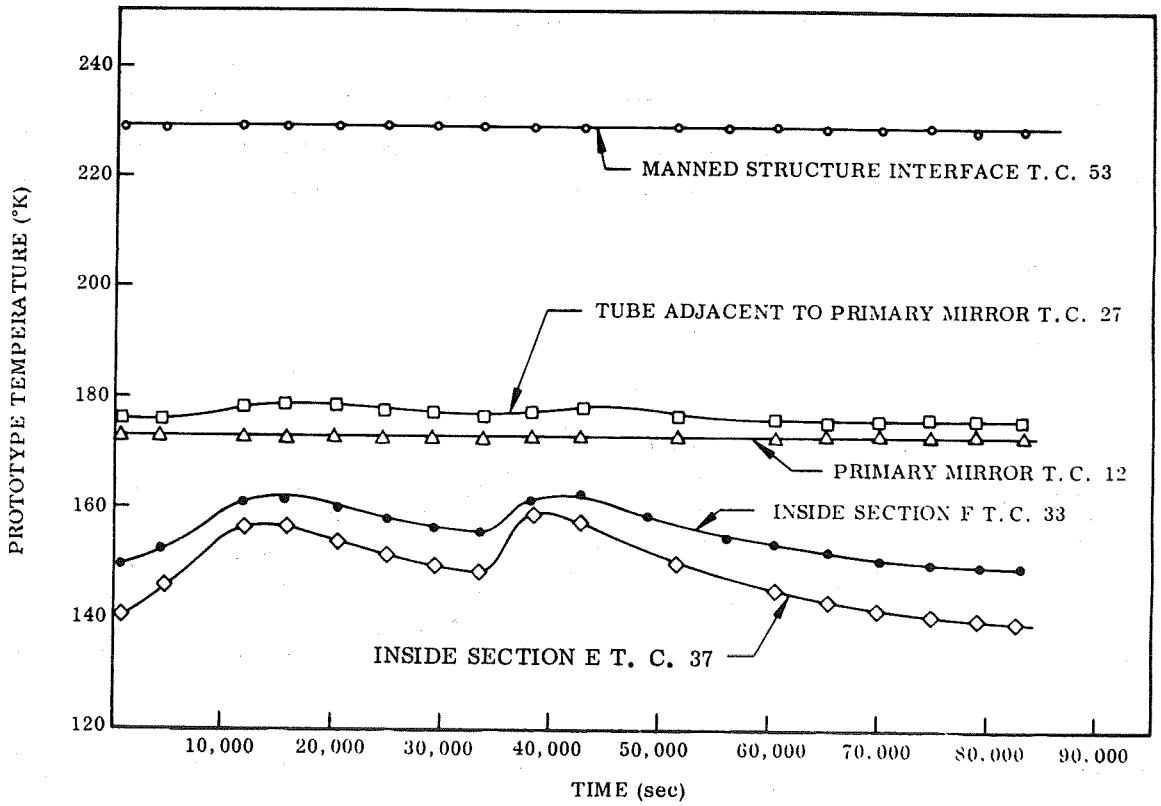

FIGURE 12. TEMPERATURE HISTORY FOR THE PROTOTYPE'S PRIMARY MIRROR AND THE SURROUNDING AREA

Figure 13 depicts the transient behavior of the secondary support rods. The base of the rods (T.C. 24) was at a higher temperature than the primary mirror (T.C. 27 adjacent to mirror) because of the conductive link with the manned structure interface. The temperature histories of the secondary support rods at thermocouple locations removed from the primary mirror were close to those of the adjacent tube sections, thus indicating a strong radiation link.

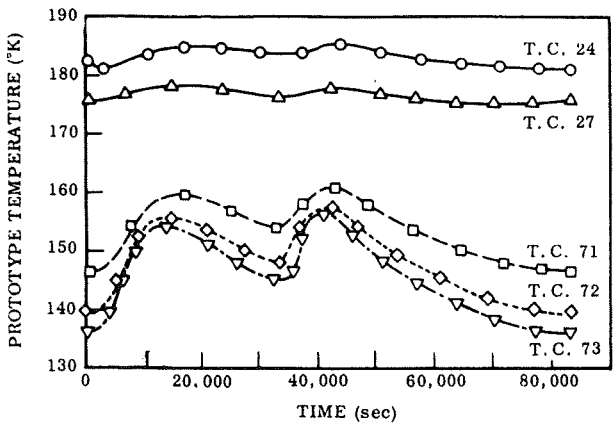

FIGURE 13. TEMPERATURE HISTORY FOR THE PROTOTYPE'S SECONDARY SUPPORT RODS

The thermal expansion of the model's secondary support rods as determined from strain gage measurements is shown by the solid curve in Figure 14.

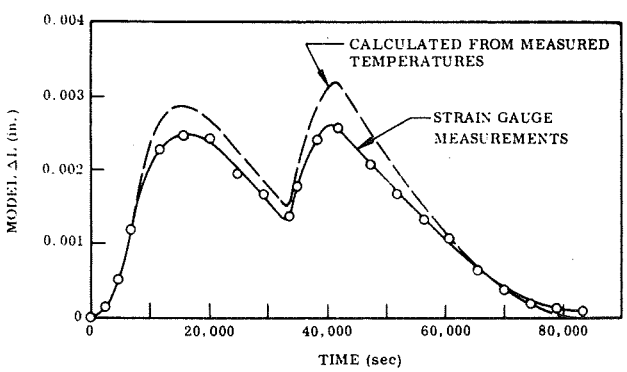

FIGURE 14. THERMAL EXPANSION OF THE MODEL'S SECONDARY SUPPORT RODS

All three rods exhibited nearly identical elongations. The dashed curve shows rod elongation computed from the measured temperature data shown in Figure 13. The maximum predicted prototype rod elongation was 1.88×10^{-6} meters with the corresponding change in optical path between the primary mirror and exit optics of 3.76×10^{-6} meters.

Table II shows the temperature history of the prototype's primary mirror. These values were predicted from measured model temperatures by using the model laws and fall well within the design goals of the prototype. This table and the curve in Figure 12 of the primary mirror's temperature indicate the success achieved in eliminating thermal transients in the primary mirror.

TABLE II. TEMPERATURE HISTORY OF THE PROTOTYPE'S PRIMARY MIRROR (°K) (Determined from Measured Model Temperatures)

Thermocouple	Location	Time (sec)				
		0	20,300	33,800	42,900	60,900
11	Front Center	172.1	172.8	172.6	172.7	173.0
12	Front Middle	172.2	172.5	172.7	173.1	173.0
13	Front Edge	172.4	172.8	172.9	173.3	173.3
16	Rear Center	172.3	172.7	172.9	173.1	173.2
17	Rear Middle	172.9	172.9	173.4	173.7	173.5
18	Rear Edge	173.0	173.0	173.3	173.6	173.7
12	1 Front Middle	172.2	172.5	172.7	173.1	173.0
14	2 Front Middle	172.1	172.5	172.7	173.0	172.9
15	3 Front Middle	172.1	172.4	172.7	173.0	172.8
17	1 Rear Middle	172.9	172.9	173.4	173.7	173.5
22	2 Rear Middle	172.8	172.8	173.2	173.4	173.4
23	3 Rear Middle	172.8	172.8	173.3	173.5	173.4

CONCLUSION

Results of the overall program establish the feasibility of using scaled thermal models for prediction of the thermal and structural behavior of large-aperture space telescope systems. Favorable comparison of analytical and experimental results reinforce the premise that passive thermal control techniques will be sufficient for thermal control of the interior of the assumed prototype 2-meter OTES telescope. During the design phase, a major advantage of a thermal and structural model is that a variety of tests can be performed on a working model, thus offering the thermal designer added flexibility in thermal and structural performance studies and permitting immediate experimental observation of the influence of proposed design changes.

REFERENCES

1. Jones, B. P.: Thermal Similitude Studies. Journal of Spacecraft and Rockets, vol. 1, no. 4, July - August 1964.

2. Watkins, J. R.: Sets of Similarity Ratios for Thermal Modeling. NASA TND-3452, May 1966.

3. Jones, B. P.; and Harrison, J. K.: A Set of Experiments in Thermal Similitude. NASA TMX-53346, October 1965.

4. Rolling, R. E.: Thermal Scale Modeling in a Simulated Space Environment. Lockheed Palo Alto Research Laboratory, Summary Report, Contract NAS8-11152, April 30, 1966.

5. Matheny, J. D.: Thermal Design Studies. Bureau of Engineering Research, University of Alabama, Final Report, Contract NAS8-5270, September 1965.

6. Rolling, R. E.; Marshall, K. N.; and Murray, D. O.: Thermal and Sturctural Modeling of a Large Aperture Space Telescope. Lockheed Palo Alto Research Laboratory, Final Report, Contract NAS8-20411, September 1968.

PHASE CHANGE THERMAL CONTROL DEVELOPMENT

By

Tommy C. Bannister

INTRODUCTION

A very desirable tool for spacecraft thermal control is a thermal capacitor, often referred to as a reversible heat sink. The reason such devices are important is that a spacecraft's thermal control system capability is usually designed according to the maximum expected heat flux rates. If these flux rates have intermittent spike heating peaks and cycles, the thermal control system must be able to handle this maximum situation. A thermal capacitor can be used to smooth out such spike heating peaks, thereby drastically reducing the requirements imposed upon the remainder of the thermal control system. In many cases, sufficient area does not exist on a spacecraft to radiate all of the excess heat to space during the maximum heat loads. Often this maximum heat load period can be dampened out by the addition of a thermal capacitor.

Space Sciences Laboratory, MSFC, has been engaged in analyzing the use of freezing and melting materials (called PCM) such as hexadecane, octacosane, etc., to design a reversible heat sink for spacecraft. These materials melt around room temperature, or from 0° C to 100° C; they have heats of fusion of about 3/4 that of water; and they are nontoxic, noncorrosive, etc. One of their better features is that the thermophysical properties of this family of materials are all very similar, and they melt at different points, which gives a great deal of selectivity.

SUMMARY OF IMPORTANT FACTORS AND PROBLEM AREAS

The important problems and factors that are involved in using PCM for a reversible heat sink are listed in Table I. Obviously, an important parameter is the heat of fusion. The heat of fusion must be large to obtain high heat storage capability. The melting point is of considerable interest because the sink temperature required will vary according to the specific application. A -6.1° C (21° F) heat sink, or thermal capacitor, is presently planned for the Air Lock which connects into the Multiple Docking Adaptor. This is being handled by S&E-ASTN. An octacosane heat sink that melts at 60.5° C (141° F) is planned for use on the LEM (according to the latest report from Grumman).

The specific heat and thermal diffusivity must be known because they are an input in the thermal computer programs used to make the required thermal analysis. The thermal diffusivity is one of the key parameters because it is the limiting factor in using this heat-sink technique. A high diffusivity is required for rapid response; however, high heat of fusion materials usually have low thermal diffusivities. Thus, we are always trying to improve the "effective thermal diffusivity" with our package design. Foamed metal, metallic wool, spacers, and honeycomb can be used to increase the diffusivity; honeycomb usually is best. In the future, heat pipes may be incorporated. Such a system would possess the high heat storage capability of PCM and the rapid heat flow of a heat pipe, resulting in a thermal capacitor with expanded capability.

In one set of studies made on thermal diffusivity several packages were designed and tested. For each package, the effective thermal diffusivity and the additional weight required to obtain that thermal diffusivity were defined. This weight was in the form of honeycomb, metallic conductors, etc. The optimum design for most applications using honeycomb was a ratio of 90 percent PCM and 10 percent honeycomb (aluminum) by weight. Another factor that must be considered is the rate of phase change. Some materials cannot be frozen rapidly; they do not react according to the thermal boundary conditions. The thermal designer must make sure that the material being used responds in a predictable fashion.

Another important parameter is convection in the liquid melt. Convection occurs in three-dimensional heat transfer, oftentimes violently.

TABLE I. THERMAL FACTORS/OTHER FACTORS

THERMAL FACTORS
1. HEAT OF FUSION
2. MELT POINT
3. SPECIFIC HEAT
4. THERMAL DIFFUSIVITY
5. PHASE CHANGE RATE
6. CONVECTION
OTHER FACTORS
1. EXPANSION AND CONTRACTION
2. VOIDS AND BUBBLES
3. DENSITY
4. CORROSIVENESS
5. TOXICITY
6. STABILITY
7. COST

Convection may be a result of several driving forces. The dominant driving force on earth is gravity. There is Marangoni convection, capillary-action convection, fluid motion caused by expansion and contraction, etc. The amount of convection in the melt must be known in any thermal vacuum tests as well as in space orbit. Also, when these materials melt or freeze, they expand or contract. An allowance for this is made in the package design.

In addition, dissolved gases, or hot spots, might create bubbles. The design must insure that a bubble will not be detrimental. A bubble, or a void area, may create a thermal boundary so that the heat cannot get in and out of the phase change material. Density is another factor; the density of the materials being discussed is about 0.8. In some applications, volume might be more of a constraint than weight. In this case a more dense material, such as Gallium or Wood's metal, may be used where a slight sacrifice of the heat of fusion is made for volume. Metals have a density an order of magnitude greater than 0.8.

Other factors to be considered are corrosiveness, toxicity, stability, and cost.

MAJOR ACTIVITIES IN THE AREA

Table II shows a summary of our major activities in this area. Of course, like the thermal diffusivity studies, a number of experimental studies have been made, such as thermal vacuum testing of simple systems. Usually all of the required thermophysical properties are not available in the literature. Calorimetric measurements have been obtained. The heats of fusion and the specific heats have been defined for all the PCM materials studied over the applied range of temperatures. One of the main areas of work has been the optical observation of the growth. The family of materials — hexadecane, octacosane — are organic and are transparent in the liquid state so that a microscope can be focused through the liquid material onto the solid/liquid boundary. By pumping away the heat and inducing freezing and melting, microscopic observations of the solid/liquid interface can be made. You can observe the reactions, the effects of convections, growth rates, grain structure, etc. This is discussed in more detail later.

TABLE II. SUMMARY OF MAJOR ACTIVITIES

A. THERMAL VACUUM TESTING OF SIMPLE SYSTEMS
B. CALORIMETRIC MEASUREMENTS
C. OPTICAL OBSERVATION OF GROWTH
D. FLIGHT EXPERIMENT T005 "FUSIBLE MATERIAL SPACE RADIATOR"
E. RESEARCH AND DEVELOPMENT CONTRACTS
1. NORTHROP (NAS-11163)
2. NORTHROP (NAS8-20670)
3. LOCKHEED (NAS8-21123)
4. MIDWEST RESEARCH INSTITUTE (NAS8-21452)
5. COLORADO SCHOOL OF MINES (NAS8-30511)

Several thermal design groups, including those at the Jet Propulsion Laboratory and the Manned Spacecraft Center, have seriously considered the use of phase change material flight applications, but have rejected it because they did not have sufficient flight data and confidence in the system. Thus, Space Sciences Laboratory proposed a flight experiment where a simple phase-change material package designed in the configuration of a space radiator would be flown to test the technique (Fig. 1). The radiator is designed to be thermally isolated from the spacecraft and would be exposed to solar heating. A simulated (electronic) heat profile has been defined that would be tested. Ten thermistors are incorporated on it to measure the thermal responses. This experiment is still in the definition stage.

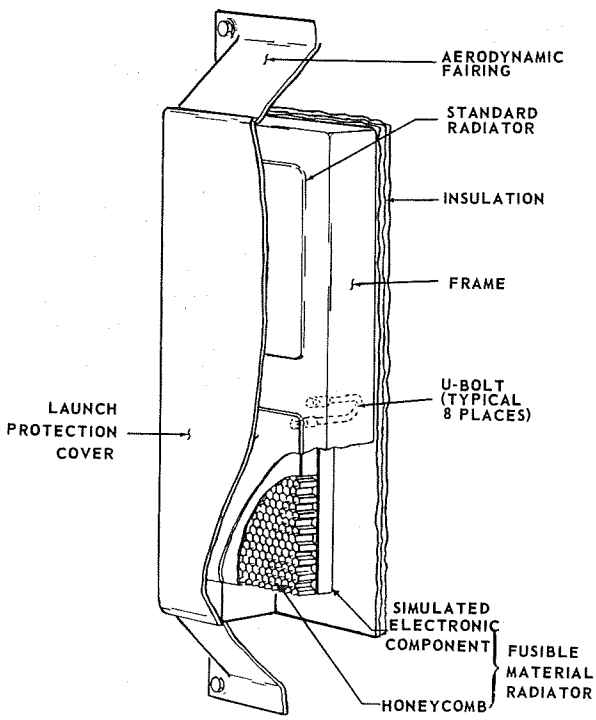

FIGURE 1. THE SPACE RADIATOR EXPERIMENT

Part of the research and development has been performed by contract (Table II). The two Northrop contracts are now completed. The first Northrop contract was to perform basic design studies on phase change packages. The second one was for definition of the flight experiment. The last three contracts are presently active. Lockheed is studying the various mechanisms involved in solidification and trying to ascertain whether or not there will be any zero-gravity effects on these various mechanisms. The real question is: "Will the zero-gravity environment of space affect solidification?" It might be mentioned that this is a basic problem that is being faced, or is going to be faced in the Manufacturing in Space programs where it is proposed to grow semiconductor crystals and other things in space. Zero-gravity effects on the solid/liquid interface might produce a new layer regime, thereby altering the solidification process. Another objective of the Lockheed study is to define possible supercooling and to define additives, or dopants, that can be added to the material matrix to prevent unexpected and erratic supercooling.

There is a contractual study with the Midwest Research Institute (MRI) in Kansas City, Missouri, to study the use of mesocrystalline materials for this type of application. A mesocrystalline phase is between a solid/solid change and a solid/liquid change. The fluid-flow problem in the liquid melt will be much less with mesocrystalline PCM's. Some changes of this type have very high latent heats of transition.

There is a contractual study with the Colorado School of Mines in Golden, Colorado. This is a small study effort on solving the problems of the effects of unsteady-state temperature distributions on solidification.

OPTICAL OBSERVATION OF CRYSTAL GROWTH

Figure 2 shows the experimental arrangement for making the previously mentioned optical observations of the crystal growth. A microscope is focused into a specially designed cell. The cell is about 3 cm high and 1 cm in diameter. A heat pumping system mates to the ends of the cell. A prescribed set of thermal boundary conditions is applied, initiating solidification. The visual observations are recorded on time-lapse film with the camera shown in Figure 2. The camera is operated by a pulse generator to obtain the required framing rate. A 20-minute movie showing crystal growth was produced at the MSFC Photo Lab and is available for showing on request.

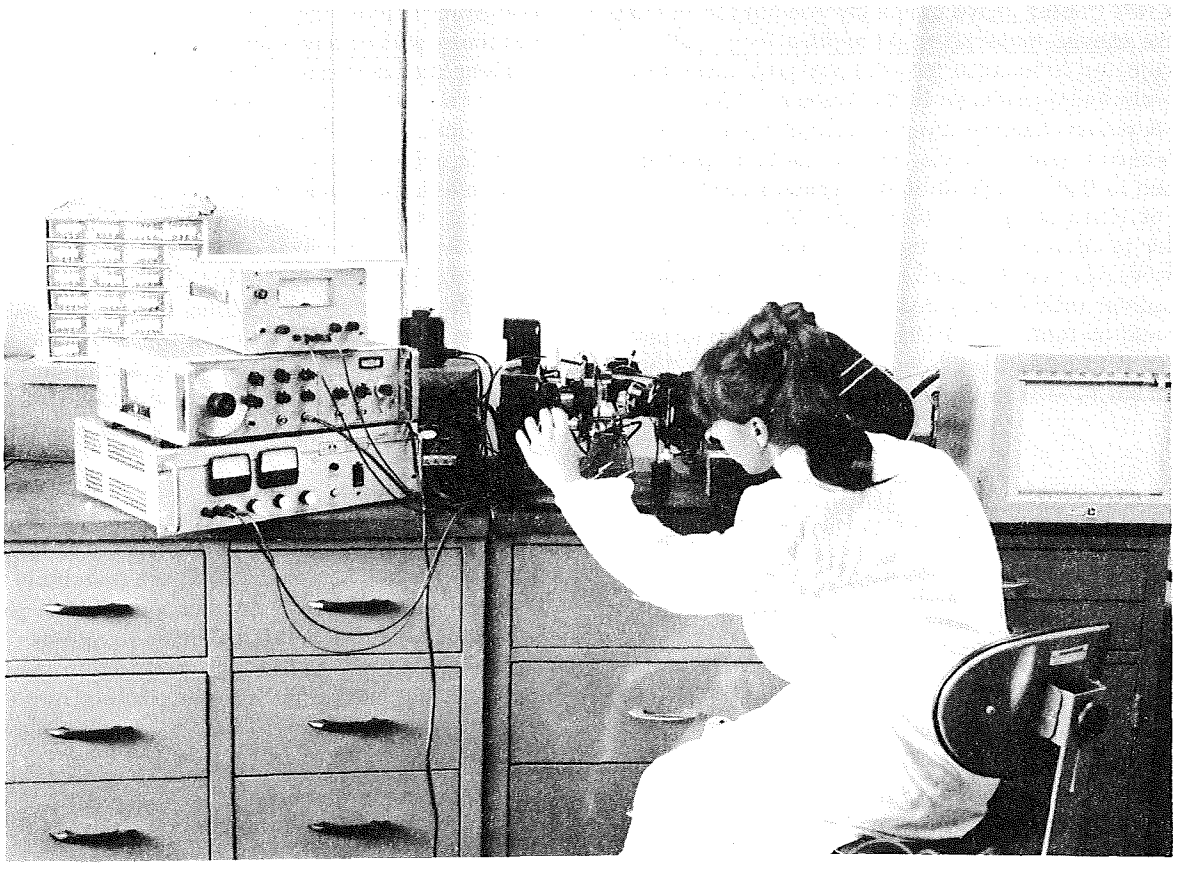

FIGURE 2. OPTICAL OBSERVATION OF CRYSTAL GROWTH

Figure 3 shows a sample microphotograph of the solid/liquid interface. This is magnified about 50 X and can be enlarged to 2000 X on a projection screen without loss of clarity. The solid is shown at the bottom and the liquid at the top (observe the interfacial structure). Figure 4 shows the size of the spikes versus the growth rate, which is a function of the heat pumping rate. It is possible to obtain the growth rate, the average growth rate, the point growth rates (at any point) and the structure of the grains from the microphotographs. The structure of these grains is very similar from one member of this family of materials to another; of course, they do vary. The color is indicative of the thickness of these grains. The convection in the liquid melt can be observed by interjecting inert particles such as carbon dust.

In one study, some of these materials were frozen in a centrifuge, at more than 1 g; i.e., 5 g and 10 g. The results were somewhat surprising. The grain sizes were much, much smaller. The microphotographs were not as good from the centrifuge because of camera alignment problems and space on the centrifuge head. However, these data were such that one can say, with confidence, that the grain sizes were much smaller. Does this mean that these grain sizes will be much larger in space? This is open to conjecture and further studies are required on all possible zero-gravity effects on the mechanism of solidification. The materials shown in Figure 4 are hexadecane mixed with 95 percent octadecane (a binary mixture of this family of hydrocarbons).

FIGURE 3. A TYPICAL MICROPHOTOGRAPH OF A SOLID/LIQUID INTERFACE (34X)

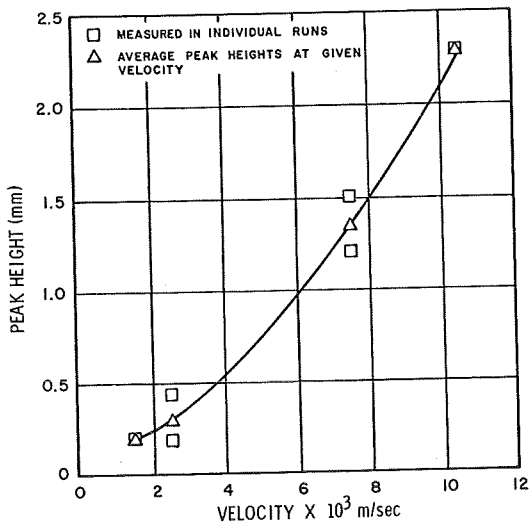

FIGURE 4. PEAK HEIGHTS VERSUS GROWTH VELOCITY IN A BINARY MIXTURE OF 5 PERCENT HEXADECANE AND 95 PERCENT OCTADECANE

SPACE APPLICATIONS OF THE HEAT PIPE

By

C. G. Fritz

SUMMARY

A heat pipe is a self-contained device that achieves very high rates of heat transfer by means of two-phase fluid flow with capillary circulation. The need for high rates of cooling in nuclear reactors and special thermal control applications on space vehicles provided much of the impetus for the current heat pipe development activities.

The primary interest in the heat pipe within the Astronautics Laboratory, Science and Engineering Directorate, George C. Marshall Space Flight Center (MSFC) is centered around thermal control applications in space vehicles. The heat pipe technology effort presently underway has as its principal objective the collection of design data for optimization of wick and pipe geometry.

This paper covers some analytical and experimental results obtained inhouse, as well as efforts both inhouse and on contract, for developing heat transfer techniques for space vehicle applications.

INTRODUCTION

A heat pipe is a closed system for transferring large quantities of thermal energy almost isothermally between a heat source and a heat sink. It functions as a two-phase device, and its operation is based on the transport of energy as latent heat of a vapor from the hot region (evaporator) to the cold region (condenser). In operation, a liquid is vaporized in the hot region and the vapor flows to the cold region where it condenses. The condensate then returns to the evaporator through a wicking material under the action of capillary force (Fig. 1). This last feature, the return of the condensate by capillary action distinguishes the heat pipe from an ordinary refluxing boiler, and therein lies its potential. Since the system does not rely on gravity for its operation, it is suitable for space applications.

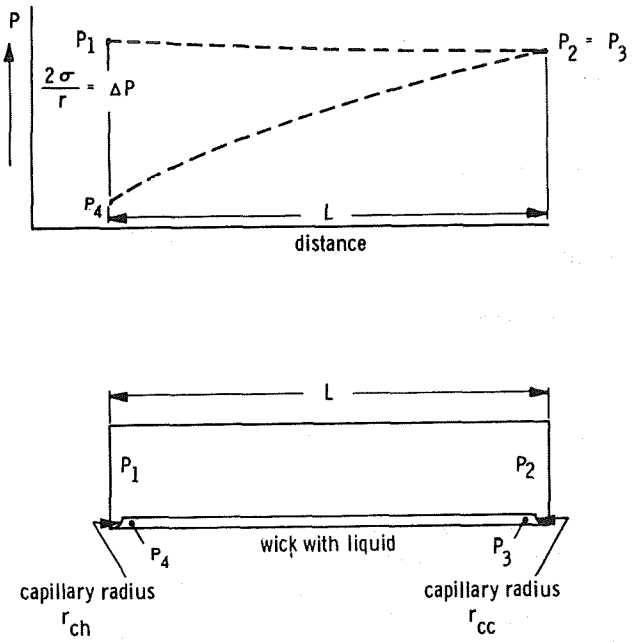

FIGURE 1. HEAT PIPE OPERATIONAL SCHEMATIC

Theoretically, the heat pipe is unlimited in its geometry, and its application will be limited only by engineering, fabrication, and material considerations. However, for the purposes of this discussion, a particular geometry will be considered. The performance of a heat pipe is strongly dependent upon geometry, and by choosing one prudently, the equations describing the system can be greatly simplified without losing sight of the principles involved.

Consider a heat pipe in the form of a long cylinder connecting a heat source to a heat sink. The heat pipe is adiabatic with respect to its environment except at the source and the sink. The capillary wick is an annulus lying against the inner wall of the cylinder. Thus, the vapor flows through the central core of the pipe and the condensate returns through the annular wick.

OPERATION OF A HEAT PIPE

For the systems described, there are essentially six transfer processes operating simultaneously:

1. Heat is transferred from the heat source through the pipe wall and the saturated wick to the liquid-vapor interface.

2. The liquid is vaporized at the interface (wick surface).

3. The vapor flows from the evaporator to the condenser.

4. The vapor condenses at the wick surface (vapor-liquid interface).

5. Heat is transferred from the vapor-liquid interface through the saturated wick and pipe wall to the heat sink.

6. The condensate flows from the condenser to the evaporator through the wick by capillary action.

For now, it will suffice to say that processes 1 through 5 can be considered as series resistance. These resistances must be overcome by a temperature gradient. The five processes will, therefore, determine the relationship between temperature differences and heat flow, which is often expressed in terms of an equivalent, or effectiveness, or "pseudo thermal conductance," of a heat pipe.

The sixth process, capillary flow in the wick, is not temperature-related, but when the heat rate and the resulting evaporation and condensation rates exceed the capability of the wick, operation of the heat pipe stops. The wick will dry out at the evaporator and this can be considered a burned-out condition. The performance of the wick is a limiting factor for the maximum amount of heat that can be transported by a heat pipe.

The other mass transfer processes taking place in the vent pipe, that is, the flow of the vapor from the evaporator to the condenser end, is not limiting for most geometries, because the vapor flow passage is usually large and the pressure drop is low.

Another limitation of the heat pipe is the critical temperature of the working fluid. Operation of the heat pipe depends upon the heat of vaporization and condensation. As this heat becomes zero at the critical point, heat pipe functions will stop. Performance of a heat pipe will show a significant reduction as the critical temperature is approached because of a reduction in heat of vaporization. Heat pipe operation must take place well below the critical point. The working fluids must be selected for the temperature range of heat pipe operations.

There is another limiting condition of the heat pipe. The evaporation of the working fluid at the warm end of the heat pipe will normally occur at the liquid-vapor interface of the free surface of the wick. Because heat is supplied from the outside of the heat pipe, there must be a temperature gradient across the thickness of the wick, and the temperature of the wick next to the tube wall will be higher than the temperature at the free surface. The liquid working fluid retained in the wick at the tube wall must, therefore, be either superheated, or it must be assumed that the pressure at the tube wall is higher than the pressure at the free vapor-liquid interface. The latter is probably true most of the time. It is a result of the capillary pressure in the wick.

This pressure difference is quite small. At high flow rates, nucleate boiling could occur at the wall. The vapor formed would then drive the liquid out of the capillaries of the wick. The heat pipe operation will fail or burn out. To prevent this form of failure, the temperature gradient across the wick should be as small as possible.

ANALYSIS OF THE HEAT PIPE

The heat pipe consists of communicating conduits of vapor and liquid, and these conduits are designed to continuously recirculate a boiling and condensing fluid between a heat source and a heat sink. Figure 1 shows a schematic of a typical configuration. As can be seen, a capillary force is used to maintain the liquid phase in contact with both the heat source and the heat sink.

GOVERNING EQUATIONS FOR THE DEVICE IN STEADY-STATE OPERATION

Conservation of Energy.

$$Q = N \dot{m} h_{f_g} \quad , \tag{1}$$

neglecting the effect of capillary force on the latent heat of vaporization, where

Q = heat transfer rate at either end

N = number of capillaries

$\dot{m}$ = mass flow rate per capillary

h_{f_g} = latent heat of vaporization of liquid at constant pressure

Force Equilibrium.

For the liquid,

$$P_3 - P_4 = \frac{8 \nu_f \dot{m} L N}{\pi r_c^4} \quad ; \tag{2}$$

for the capillary meniscuses,

$$P_1 - P_4 = \frac{2 \sigma \cos \theta}{r_{ch}} - \frac{2 \sigma \cos \theta}{r_c} \quad , \tag{3}$$

and

$$P_2 - P_3 = \frac{2 \sigma \cos \theta}{r_{cc}} \quad ; \tag{4}$$

for the vapor,

$$P_1 - P_2 = \frac{8 \nu_g N \dot{m} L}{\pi R^4} \quad ; \tag{5}$$

where ν_f and ν_g are the kinematic viscosities of the liquid and the vapor, and

L = length of the heat pipe

r_c = radius of the capillary tube

r_{ch} = meniscus radius at the evaporator

r_{cc} = meniscus radius at the evaporator

σ = surface tension of the liquid

R = radius of the vapor tube.

For a simple expression of heat pipe characteristics, it is assumed that

$$P_2 = P_3, \text{ i.e., } r_{cc} = \infty \text{ and } \cos \theta = 1.$$

By substituting equation (1) into equation (5),

$$Q = \frac{\pi h_{f_g} R^4 \Delta P}{8 \nu_g L}, \text{ where } \Delta P = P_1 - P_2 . \tag{6}$$

An approximately equivalent thermal conductivity of the heat pipe can be calculated by assuming that the heat pipe cross section is equal to the cross section of the vapor conduit, or

$$k_e = \frac{g\ell}{A \Delta T} \approx \frac{Q L}{\pi R^2 \Delta T} \tag{7}$$

where $\Delta T = T_1 - T_2$.

By substituting equation (6) into equation (7),

$$k_e = \frac{h_{f_g} R^2}{8 \sigma} \left. \frac{\partial P}{\partial T} \right|_{sat} , \tag{8}$$

which means that to obtain high-equivalent thermal conductivities, fluids of large h_{f_g} require low vapor-phase kinematic viscosity and large changes in saturation pressure as a function of change in saturation temperature. Also notice that the advantages of the heat pipe increase with the square of the radius; in a first approximation these advantages are not a function of length or capillary configuration. However, the maximum heat flux that can be handled by the heat pipe is a definite function of the parameters shown in equations (6), (7), and (8). Adding equations (2), (3), and (5) and assuming that

$$P_2 = P_3 \text{ and } \cos \theta = 1$$

gives

$$Q = \frac{\sigma}{r_{ch}} \frac{\pi}{4} \frac{h_{f_g}}{L} \frac{1}{\left(\frac{\nu_f}{r_c^4} + \frac{\nu_g}{R^4}\right)} , \qquad (9)$$

Since the minimum value that r_{ch} can have is r_c, the maximum heat transfer that can be handled by the heat pipe is

$$Q_{max} = \frac{\sigma}{r_c} \frac{\pi}{4} \frac{h_{f_g}}{L} \frac{1}{\left(\frac{\nu_f}{r_c^4} + \frac{\nu_g}{R^4}\right)} , \qquad (10)$$

which shows that the upper limit of heat transfer is proportional to the surface tension of the liquid and to the heat of vaporization and is inversely proportional to the length and to a rather complex function of r_c, ν_f, ν_g and R. It is clear, however, that Q_{max} is increasing the number of capillaries and the radius, R, of the heat pipe.

EXPERIMENTAL

Today's state-of-the-art of a heat pipe is, at best, only approximate when compared with analytical data. The equations for a heat pipe assume equilibrium conditions and are optimized for higher limits of operation. Figure 2 shows two equations that point out some of the more pertinent parameters encountered. The figure of merit (FOM) is directly proportional to latent heat of vaporization and density of the liquid; inversely proportional to kinematic viscosity; and is a function of temperature only. Thus, the FOM should be used as a basis for showing the relative merits of one fluid versus another, as shown in Figure 3.

The next equation shows the heat transferred and some other important heat pipe parameters such as wick thickness, driving potential for the vapor, and a thermal transformer relationship. Because boiling and condensing processes are essentially independent, either process may be taken over a larger area with a low heat flux, or over a small area with a high heat flux.

The concern at MSFC is two-fold, to develop analytical capability for accurately predicting heat

$$\text{figure of Merit} = \frac{h_{fg_t} \; \sigma_t}{\nu_t}$$

where h_{fg} - latent heat of vaporization
σ - surface tension
ν - kinematic viscosity

subscripts:
t - temperature

$$\dot{q} = \frac{2\pi L_c L_e k \left[\left(T_{s_e} - T_{s_c}\right) - \left(T_{i_e} - T_{i_c}\right)\right]}{\left(L_e + L_c\right) \ln \frac{r_s}{r_i}}$$

L - length
T - temperature
r - radius
k - thermal conductivity
q - heat transfer

subscripts: c - condenser
e - evaporator
s - surface of heat pipe
i - inside of heat pipe

FIGURE 2. EQUATIONS FOR A HEAT PIPE

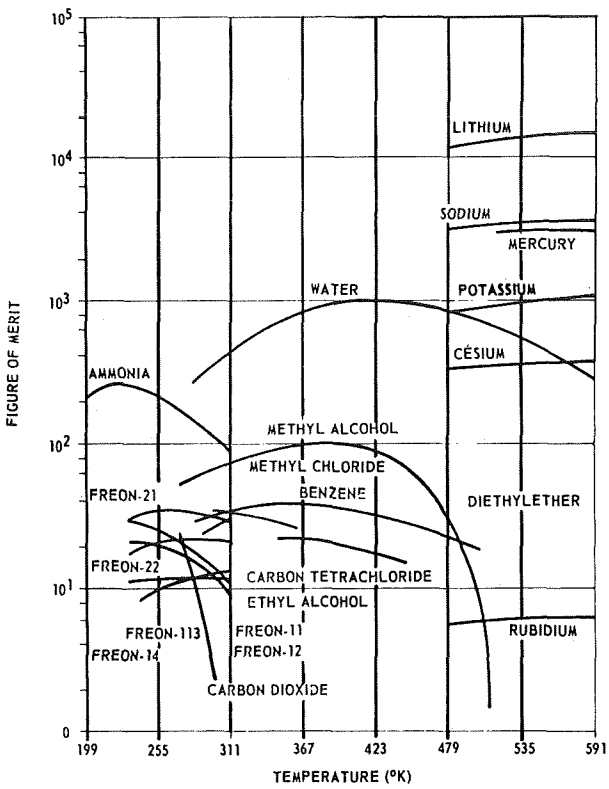

FIGURE 3. COMPARISON OF FLUIDS FOR A HEAT PIPE

pipe design and to determine heat pipe operational characteristics. At present this state-of-the-art is poor, and under transient conditions is impossible. As an interim, an experimental program is being conducted to obtain pertinent data for heat pipe design. A few of the parameters being investigated are L/D ratios, wick thickness, and stabilization times for a heat pipe operation.

THERMAL CONDUCTIVITY VERSUS TEMPERATURE

The thermal conductivity of a stainless steel rod, as shown by the dotted line in Figure 4,[1] was taken from page 22 of Reference 1. The thermal conductivity of the heat pipes at each temperature was determined by interpolating between the results calculated for solid rods from the computer program and comparing these values with the heat input in the experiments. The results are shown in Figure 4.

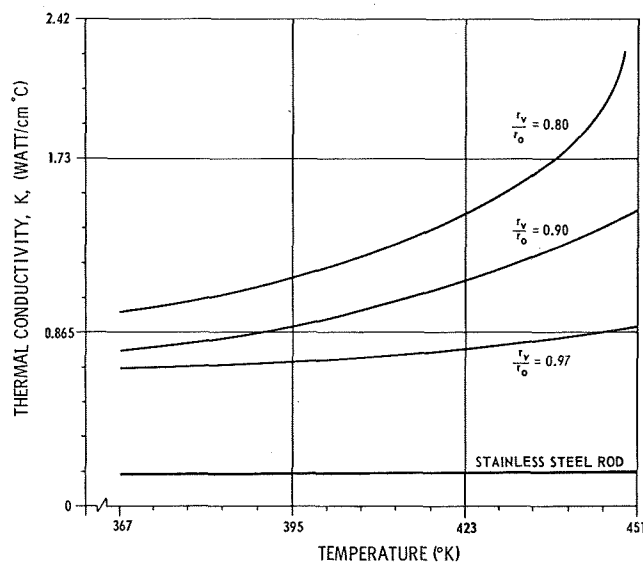

FIGURE 4. THERMAL CONDUCTIVITY VERSUS TEMPERATURE (Heat pipe as a radiating fin)

The data shown in Figure 4 indicate that the thermal conductivity is dependent on the wick thickness. To show the range of r_v/r_o in the experiments, curves were drawn for three different r_v/r_o's. The r_v/r_o ratios chosen were approximately 0.8, 0.9, and 0.97.

TEMPERATURE PROFILE OF A HEAT PIPE AND A SOLID ROD OF COMPARABLE SIZE

To compare the change in temperature caused by a heat pipe occupying a portion of a solid rod and a solid rod of comparable size, a test case for a heat pipe and a run for a solid rod from the computer program were chosen.[2] The computer data were obtained by using a solid rod the same size as the

1. Figures 4, 5, and 6 are taken from a Doctoral Dissertation, "An Experimental and Analytical Study of Water Heat Pipes for Moderate Temperature Ranges" by Billy Grant McKinney, University of Alabama, 1969

2. Price, J. W.: A Computer Program for Finding the Nonlinear Heat Transfer and Temperature Distribution through a Constant Cross-Sectional Area Fin. Report No IN-P&VE-P-68-9, MSFC, Huntsville, Alabama, September 1968.

heat pipe and having a thermal conductivity of 10 Btu/hr-ft-°R. For the computer run, the base and surrounding temperature were assumed to be the same as the operating temperature of the heat pipe and the temperature of the inside of the vacuum chamber. The test case chosen was test No. 4b, and the temperatures, as shown in Figure 5, were taken from the experimental data.

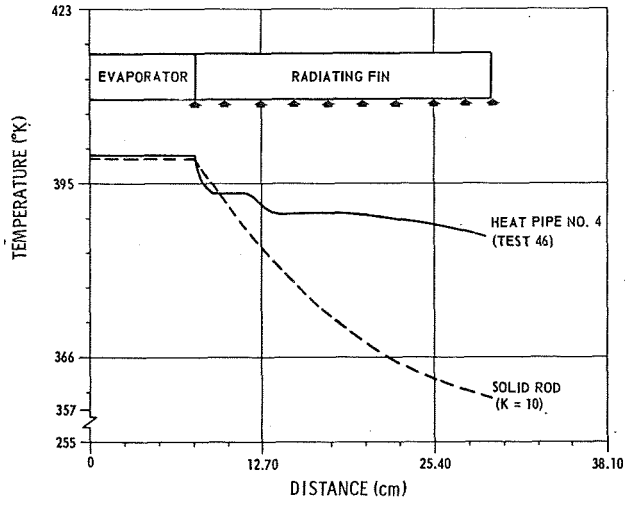

FIGURE 5. COMPARISON OF A HEAT PIPE AND A SOLID ROD

By observing Figure 5, it was apparent that by making a fin a heat pipe, the temperature at the end farthest from the source more nearly approaches the base temperature than if the fin was a solid rod of comparable material. Test No. 4b shows that a heat pipe will raise the temperature of this end approximately 298.15° K above the temperature of the end of a solid rod.

LENGTH-TO-DIAMETER RATIO VERSUS HEAT INPUTS FOR HEAT PIPES AS RADIATING FINS

For heat pipes, L/D ratios have been discussed in previous investigations. The data for making a comparison of L/D ratios were unavailable. In this investigation, four heat pipes having constant wick thicknesses, but with different L/D ratios, were employed. The L/D ratios fell in the range of 4 to 24. To compare L/D ratios, the heat inputs through the containing cylinder were not considered. To arrive at the heat inputs, interpolations were made of the results shown in Table I. These results are plotted in Figure 6.

As the L/D ratio became small, the heat input varied approximately as the radius of the vapor space. This was especially true when going from an L/D of 4 to 8. In this range, as the heat input doubled, the radius of the vapor space approximately doubled. For values of L/D larger than 8, this

TABLE I. SUMMARY OF EXPERIMENTAL HEAT INPUTS AND LOSSES FOR HEAT PIPES AS RADIATING FINS

(1) Heat Pipe Number	(2) Test Number	(3) Date	(4) Time	(5) Temperature In The Vapor Space °K	(6) T_s °K	(7) Heat Input To System Btu/hr	(8) Heat Loss (Calculated) Btu/hr	(9) Heat Input To Heat Pipe Btu/hr
1	1a	10/25/68	0900	377.6	300.9	52	27	25
1	1b	10/22/68	1030	403.7	309.3	98	43	55
1	1c	10/23/68	1045	427.0	310.9	137	60	77
1	1d	10/24/68	0930	454.3	312.7	209	94	115
2	2a	10/30/68	1440	365.9	303.2	65	24	41
2	2b	10/31/68	1300	395.4	307.0	111	47	64
2	2c	11/1/68	1400	420.9	310.9	176	84	92
2	2d	11/5/68	1430	440.4	313.7	293	71	122
3	3a	11/13/68	0730	367.0	305.4	109	48	61
3	3b	11/13/68	1330	393.7	306.5	171	72	99
3	3c	11/14/68	0900	420.3	313.7	245	106	139
3	3d	11/15/68	0730	450.4	325.9	352	164	188
4	4a	11/13/68	1330	433.2	306.5	207	65	142
4	4b	11/14/68	0900	398.7	313.7	269	81	188
4	4c	11/14/68	1530	429.3	317.0	419	142	277
4	4d	11/15/68	0730	447.0	325.9	522	193	329

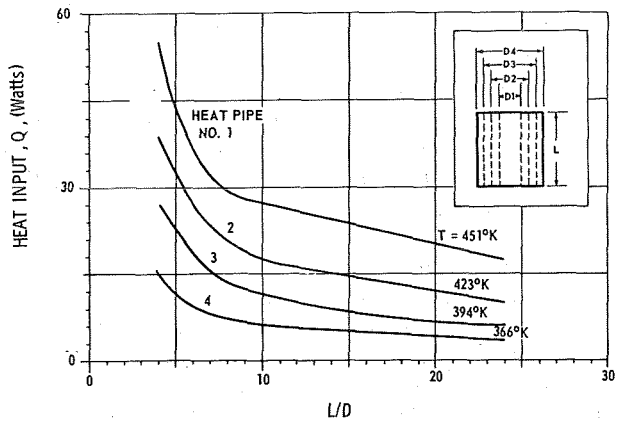

FIGURE 6. HEAT INPUT VERSUS L/D (Heat pipe as a radiating fin)

relation did not hold, because the variation in the heat input was less than the variation in the radius of the vapor space. Also observe that the high L/D ratio heat pipes could arrive at operating temperature at much lower heat input.

Figure 7 gives an indication of stabilization time for a heat pipe. Note that all the data were for a thick-walled heat pipe run vertically. The large mass caused the long time interval. But nevertheless, this points up a fact overlooked by many, that heat pipes are also a function of time to reach equilibrium.

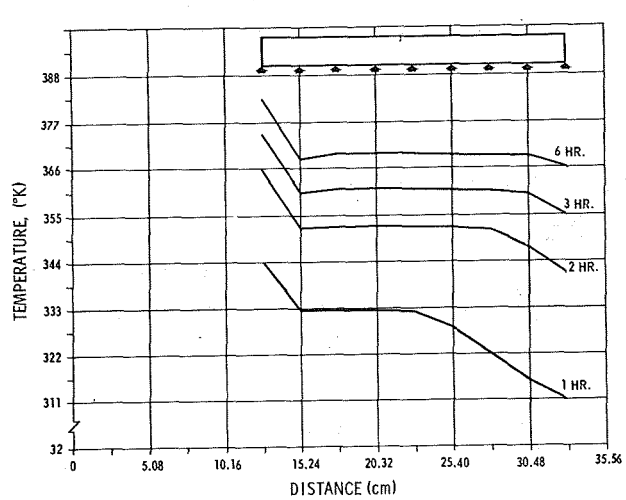

FIGURE 7. TEMPERATURE VARIATION WITH TIME

HEAT PIPE APPLICATION

Figure 8 shows the application of a heat pipe to the temperature equalization of a mirror of a space telescope. Where very close temperature equalization is required, special provisions can be made to reduce all series resistances to a minimum and make the shell and wick of the heat pipe of materials having a high thermal conductivity. A very thin felt or sintered copper or silver can be used. It is reasonable to assume that, for a heat pipe of this type, minimization of the temperature gradient will not require very high heat flow rates. This will permit the use of very thin wicks.

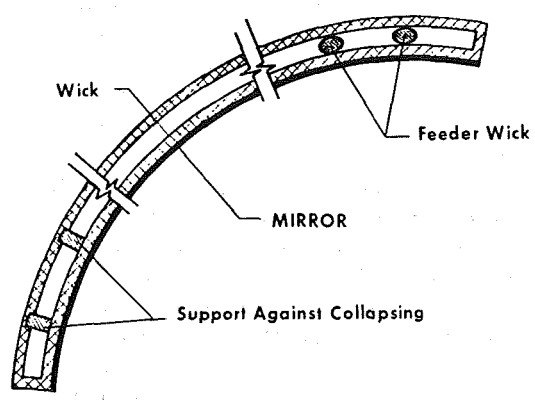

FIGURE 8. TEMPERATURE EQUALIZATION OF AN OPTICAL MIRROR

However, should a situation occur where both temperature equalization and heat flow rate become important, some type of compromise will have to be found. The performance of the wick to induce capillary flow is a limiting factor for maximum heat flow. Flow performance is, of course, a function of cross section, and the cross section of a very thin wick will be small. Where high heat flow rates are required, a very thin wick will not be satisfactory. On the other hand, if the thickness of the wick is increased, the conductive resistance to heat flow is also increased. The use of capillary structures of a high thermal conductivity metal is somewhat limited, because the structure is only 20 to 40 percent metal and 60 to 80 percent pores filled with liquid. Therefore, it would be beneficial to use a liquid of high thermal conductivity. The only liquids that can

be considered good thermal conductors are the liquid metals, which are fine heat pipe working fluids, but for many applications their solidification point is too high. For lower temperatures, water, ammonia, and alcohols are the potential working fluids. Other ways must be found to compromise between the desire for very thin, high thermal conductivity, wick material and high capillary flow rate. A way to accomplish this may be to use feeder wicks to supply relatively small areas of the thin wick layer with adequate liquid. This can be accomplished only at the cost of reduced temperature equalization, because wherever the feeder wick contacts the thin wick layer, there will not be a free liquid-vapor interface. A hot or cold spot will develop. In an actual application, trade-offs will be made between the temperature equalization requirement and the heat flow rate.

Depending upon the vapor pressure of the working fluid and operating temperature, the internal pressure in the heat pipe cavity will be lower, possibly very much lower, than 10 N/cm^2 (1 atm). For structural reasons, low operating pressure is, of course, desirable for operation in space. To prevent collapsing of the cavity during prelaunch conditions, small support studs can be used (as shown on the left side of Fig. 8). These studs would be attached only to the "rear" of the mirror's heat pipe cavity. The "rear" side of the cavity could be designed to deflect enough under exposure to external vacuum as a result of internal pressure, and to lift the support studs away from the wick surface on the back of the mirror to permit evaporation or condensation. This will prevent any "hot" or "cold" spots resulting from the use of the supporting studs.

Figure 9 shows the application of a "heat pipe" to temperature equalization of a cryogenic storage tank in space. A double shell is used as a heat pipe. It will transfer the heat from the solar irradiated side to the side of the tank that is facing space. In combination with an insulation layer, this arrangement could reduce the heat input into the cryogenic tank.

Other arrangements for temperature equalization in a cryogenic storage tank are conceivable. For example, a sort of spider of heat pipes could be located internally in the tank, connecting the warm side to the cold side. This will not be quite as advantageous as the double shell heat pipe with insulation where the heat is essentially piped around the tank.

An approach to the control of moisture condensation on the internal wall of a manned space cabin is achieved by using a device which isn't a true heat pipe, but it is similar to a heat pipe. Figure 10 shows schematically a space cabin, which may be a cylinder. Atmospheric moisture will condense on the side away from the sun, unless adequate insulation and heat input in the inner wall surface maintains the surface above the cabin dew point. Suppose the wall is lined with a capillary material that will transfer condensed moisture to the side of the spacecraft irradiated by the sun. The liquid will then evaporate and return to the cold side and condense. Since this space cabin has an atmosphere of noncondensible gas, it cannot be said that the cabin is a heat pipe in the true sense. The amount of heat transported will be quite small, but

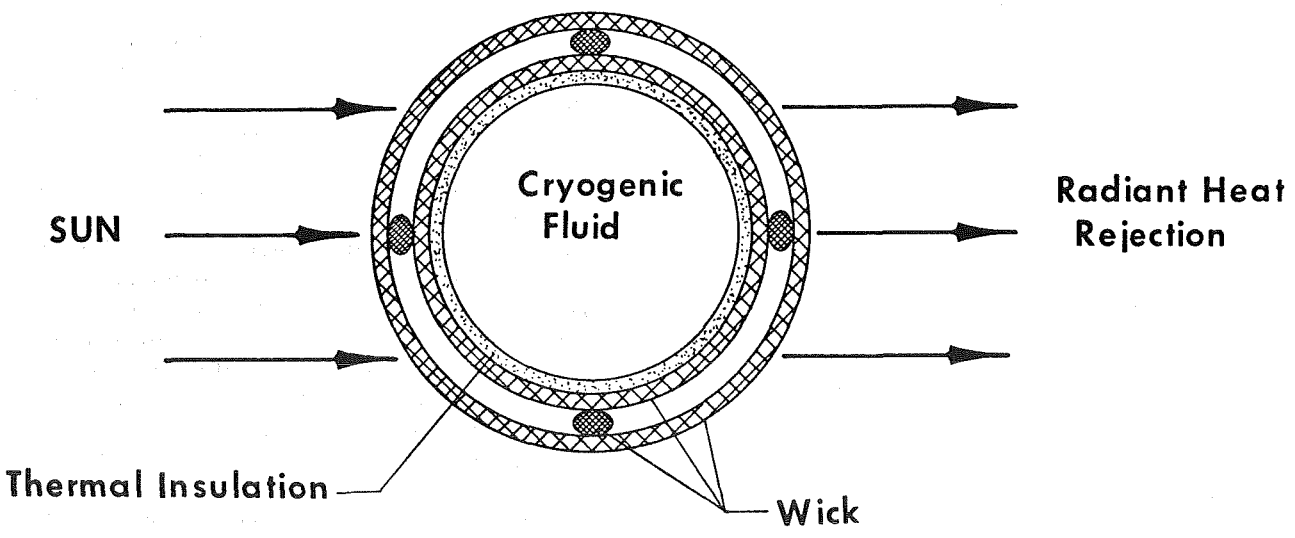

FIGURE 9. TEMPERATURE EQUALIZATION BY A HEAT PIPE DEVICE

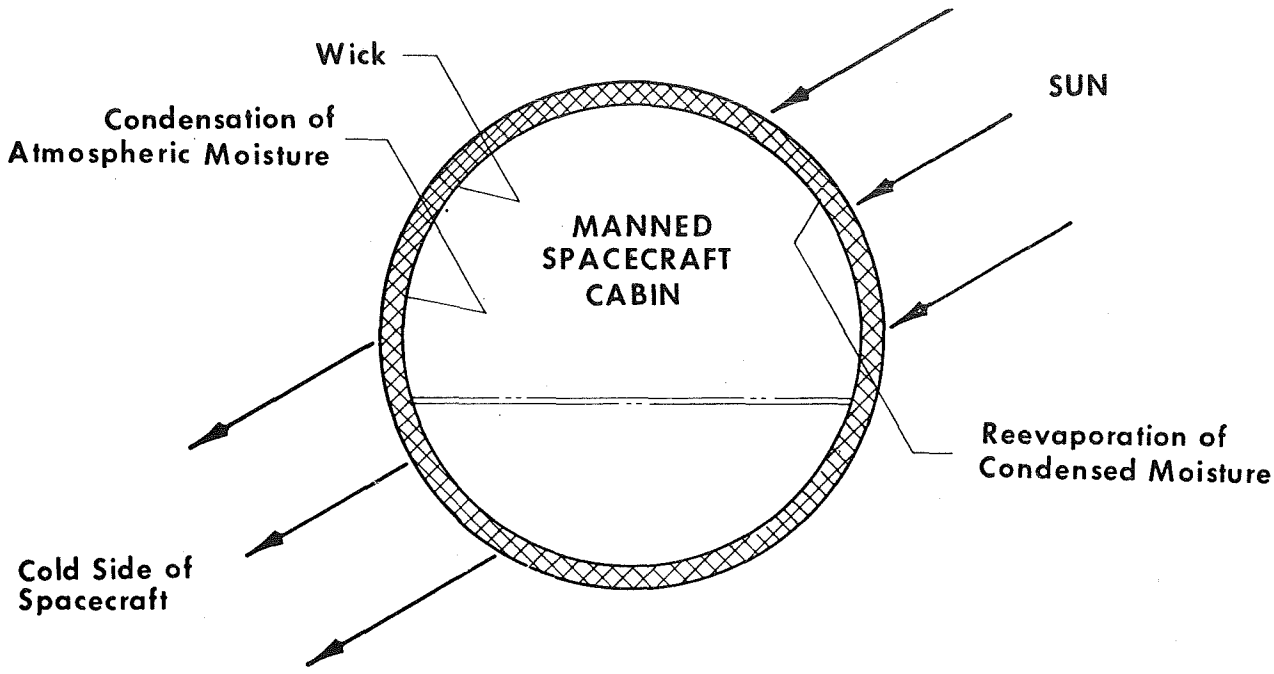

FIGURE 10. A DEVICE (WICK) WHOSE ARRANGEMENT IS SIMILAR TO THE OPERATION OF A HEAT PIPE CAN PREVENT EXCESSIVE CONDENSATION ON THE COLD SIDE OF A SPACECRAFT CABIN

eliminating the wet surface on the cold side of the cabin will also prevent the drying effect a cold surface will have on the atmosphere. The moisture condensing out on the cold side will be returned to the cabin atmosphere from the warm side. Of course, it will not make any difference at a given time which side of the spacecraft is the warm or the cold side, just as it does not make any difference in a heat pipe which end or zone is warm or cold.

The most obvious application of a heat pipe is simple transport of heat. In temperature control work, situations invariably arise when heat is generated where it is not wanted, or heat is rejected when there is a need for heat. In many systems, this has resulted in devices to transfer, or transport, heat from one place to another. The application of heat pipes for this purpose is limited on Earth by the pumping of the wick relative to the weight of the working fluid, which must be pumped from the cold end to the warm end. Under zero gravity conditions, this limitation is removed. The limiting factors for the capability of a capillary structure to transfer liquid are then only the resistance to liquid flow and the vapor pressure difference between the two ends of the wick structure, which result from the vapor flow resistance in the heat pipe. An allowance for both of these factors can be made in design. While a given wick and working fluid combination has a certain maximum lifting capability on Earth, and this limit cannot be exceeded by making the cross section of the wick larger, the cross section of the wick and the vapor flow passage can be designed to match the capability of the wick to induce capillary flow. Therefore, the distance over which heat transfer by a heat pipe under zero gravity conditions is possible has no absolute limit. Heat can, for example, be transferred from a cold plate buried inside a spacecraft to a radiator (Fig. 11).

An interesting application of a heat-pipe-type device for heat diffusion is a combination of a heat pipe with a phase change material heat sink and radiator (Fig. 12). The use of phase change materials to control temperature has been extensively studied under the sponsorship of MSFC. Its use is limited by the difficulties of heat diffusion through the melted layer of a fusible material (or in more general terms, through the layer of the higher enthalpy phase), which forms after heat addition, close to the heat source. The use of

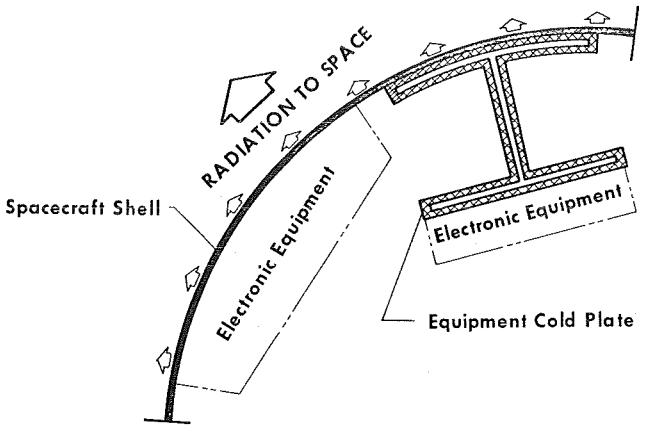

FIGURE 11. HEAT PIPE THERMALLY CONNECTS THE COLD PLATE TO THE EXTERNAL SPACECRAFT SHELL

fusible materials also involves problems of volume change on melting and solidification. These problems can be overcome by the use of very thin slabs of phase change material. The surface area relative to volume in a thin slab is large. The amount of expansion will be small and can be taken up by bulging, or "oil-canning," of the flat container. Heat can enter the containers from both surfaces.

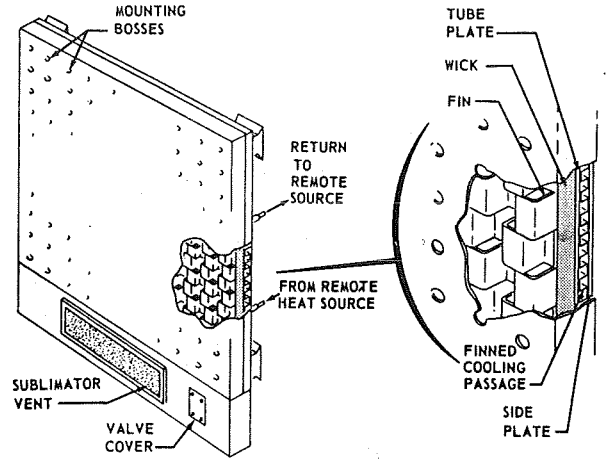

FIGURE 13. THERMAL CONDITIONING HEAT PIPE — SUBLIMATOR PANEL

1. Self-contained — not dependent on external power or pumping to distribute vapor within the panel. Contains its own water supply and control system.

2. Geometry — 0.762 m by 0.762 m (30 in. by 30 in.) as used on IU cold plates in present IU.

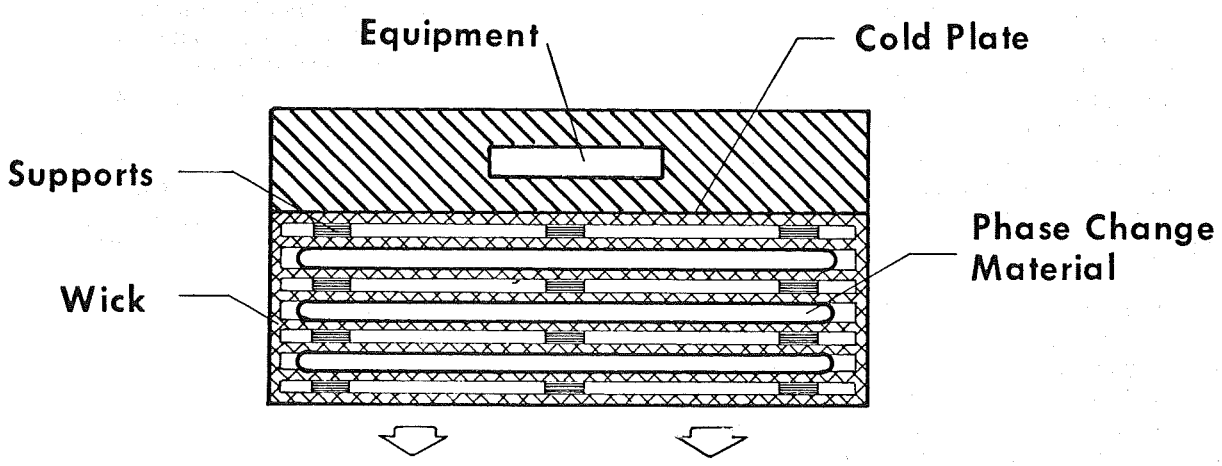

FIGURE 12. THERMAL RADIATOR

In the present Saturn Instrument Unit (IU), cold plates are employed to remove heat from the instruments. In this application, the cold plates are heat pipes with a water sublimator as a cold sink (Fig. 13). The system has the following operating characteristics:

3. Material — stainless steel with sintered porous nickel wicking material.

4. Fluid — water in panel.

5. Capacity — ten watts/mounting boss with 420 W maximum. Water supply of 5.21 kg (11.5 lb).

This amount will provide 8 hours of cooling with a maximum heat load of 1450 Btu/hr or 60 hours of cooling for 50 W.

Also in the process of being tested is the employment of four small heat pipes to increase the temperature distribution of a radiation fin (Figs. 14 and 15). This will give an increased radiation fin efficiency and allow either smaller fins for the same heat loads or higher heat loads for the same size fin.

Purdue University, under MSFC sponsored research, is studying heat pipes of mixed fluids. Here it is anticipated that fractioning of the mixture will take place when heat is added. The high vapor pressure fluid will evaporate first. If the higher vapor pressure fluid is selected (so that at a certain temperature the critical temperature of the fluid is

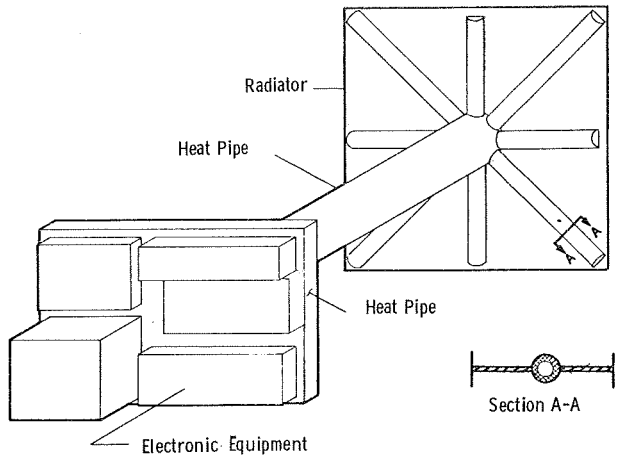

FIGURE 14. HEAT PIPE RADIATOR

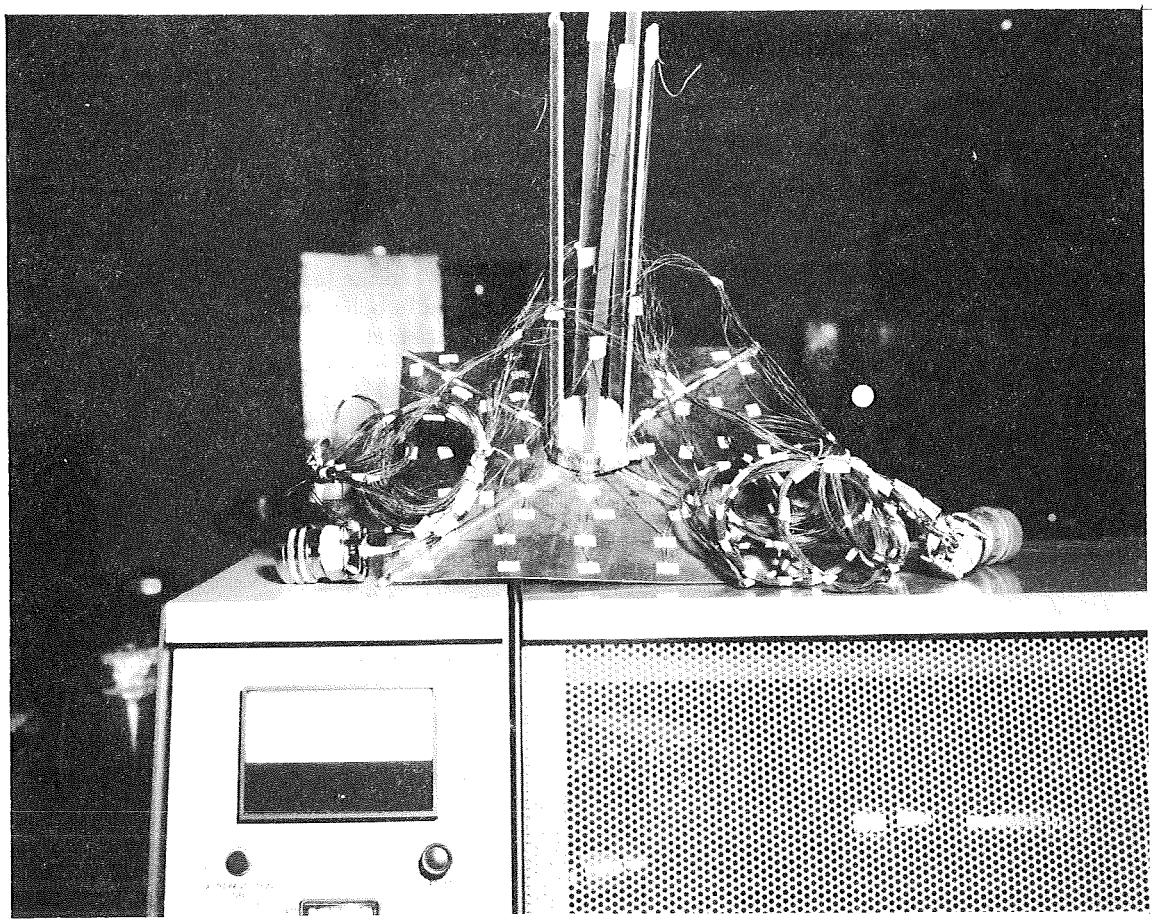

FIGURE 15. HEAT PIPE APPLICATION WITH INSTRUMENT WIRING

reached), it will act in the heat pipe to give the same result as a noncondensible gas; it will be flushed to the cool end of the heat pipe and reduced. By proper selection of mixed working fluids, it may be possible to develop a heat pipe that passively reduces heat flow when a certain temperature is reached. It is fascinating to speculate on the use of mixtures of three or more fluids with suitable critical temperatures that result in heat pipes which transfer larger or smaller amounts of heat in steps as a function of temperature.

As they are presently used, many heat transport systems require the control of the rate of heat flow. A well-known and publicized technique for controlling the heat flow performance of a heat pipe is the introduction and removal of a noncondensible gas. For application to heat pipes using water as a working fluid and operating at normal room temperature (as required in spacecraft environmental control applications and in applications for temperature control of electronic equipment), this technique will not be satisfactory. Therefore, other means must be used to control one of the six processes taking place in a heat pipe. The simplest method would be to control the vapor flow and control the pressure in the heat pipe (Fig. 16). In this heat pipe the wick passage is separated from the vapor passage, and a valve is put into the vapor flow passage. With this approach, when the vapor flow is shut off, heat flow must stop. Throttling of the valve will further permit temperature control, because by buildup of pressure on the warm side, evaporation will occur at higher temperatures, and the temperature difference between the warm and the cold side of the heat pipe will be increased.

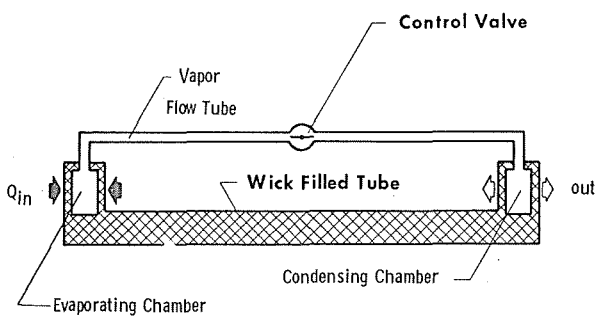

FIGURE 16. VARIABLE HEAT PIPE (Vapor Flow Control Concept)

The practical application of heat pipes is dependent upon our ability to build heat pipes of geometries required for the specific application. It must be possible to make the heat pipes round or flat, long or short, rigid or flexible, as the application requires. Heat pipes (or heat-pipe-type devices) are, however, closed vessels, and depending upon the vapor pressure of the working fluid, the operation temperature, and external pressure, heat-pipe containers may be either pressure vessels or vacuum vessels. In many applications the containers may operate as vacuum vessels before launch, and when in orbit in the absence of an external pressure, the containers become pressure vessels. Therefore, it is necessary to develop techniques that will prevent both collapsing and bursting of the containers under these conditions, regardless of the geometry of the containers. Furthermore, these techniques must permit the use of reasonable lightweight constructions, and the heat pipe shell should preferably have a high thermal conductivity.

As previously mentioned, the operation of a heat pipe will stop when the temperature in the heat pipe reaches the critical temperature of the working fluid. Selection of a working fluid of suitable critical temperature would then result in a temperature-limiting device. As heat is transferred by a heat pipe from a constant source of heat to a heat consumer, heat flow will stop whenever temperature of the heat-consuming device exceeds the critical temperature of the working fluid. When the temperature of the heat-consuming device falls below the critical temperature, the heat pipe will start up again, and heat flow will be restored.

The most important area of future research is the prevention of freeze-up of heat pipes and techniques for restarting a heat pipe that has been frozen. It is unfortunate that good heat pipe working fluids have a relatively high solidification point. This includes, of course, the liquid metals and also water, which is the best working fluid for the temperature range required for equipment cooling and human comfort applications. A heat pipe that freezes will not readily start up again. The reason for this is that when the cold end of a heat pipe goes below the freezing point of the working fluid, the working fluid in the wick will solidify. The vapor pressure at the cold end will drop, causing more evaporation of the working fluid at the warm end and flow of the vapor to the cold end where it will condense and solidify. The terminal result of a freeze-up is that all the working fluid transfers to the cold end of the heat pipe, and the wick at the warm end is dried out. When heat addition at the warm end then increases, there is no working fluid present to evaporate and heat transfers to the cold end and melts the solid formed there.

REFERENCE

1. Jakob, M.; and Hawkins, G. A.: Elements of Heat Transfer. John Wiley and Sons, Inc., New York, 1957.

THERMAL CONDUCTIVITY OF PARTICULATE BASALT AS A FUNCTION OF DENSITY IN SIMULATED LUNAR AND MARTIAN ENVIRONMENTS

By

James A. Fountain and Edward A. West[1]

SUMMARY

The thermal conductivity of a particulate basalt sample (37 to 62 microns in diameter) has been measured as a function of density in simulated lunar and Martian environments. The results are compared with literature data on thermal conductivity of solid basalt at atmospheric pressure. Samples with six densities ranging from 0.79 g/cm^3 to 1.50 g/cm^3 were measured. The A and B coefficients for the Watson equation, $K = A + BT^3$, have been evaluated using a least-squares computer curve fit to the experimental data for each density. These coefficients are useful in predicting temperatures as a function of depth below the surface for application in theoretical models of the lunar surface. A separate effort was made to determine the maximum density obtainable with this specific sample in order to draw qualitative conclusions concerning the ambiguous density value received from the Russian Luna 13 in situ density experiment.

LIST OF SYMBOLS

Symbol	Definition
K	Thermal conductivity
T	Absolute temperature
A, B	Constants
ρ	Density
X	Depth below lunar surface

INTRODUCTION

The Jones model and the Matveev model for the density-depth relationship in the lunar surface closely agree with presently available observational data [1]. Assuming the density-depth relationship is known, and if the density-thermal conductivity relationship can be found, then a conductivity-depth function can be determined that may be used in theoretical temperature-prediction models. Accordingly, the authors initiated this laboratory measuring program which would yield the dependence of the thermal conductivity on the density of a particulate sample under simulated lunar conditions. For comparison, a similar test series was also conducted on the sample under simulated Martian environmental conditions.

THE LUNAR DENSITY

Figure 1 shows a plot of the Jones model for density of the lunar surface as a function of depth. The rectangular blocks show the observational data, both from ground based radiometry and the Surveyors. The solid curves are plots of the model calculated for various model parameters. The range of densities varies from 0.4 g/cm^3 to 2.0 g/cm^3. However, all of these densities are not direct measurements but are inferred indirectly from other measurements.

The results of a direct in situ measurement of the lunar density made by the Luna 13 Russian spacecraft is shown in Figure 2 [2]. Its densimeter was a device in which gamma rays were irradiated into the

1. The authors greatly appreciate the help and suggestions of Billy P. Jones and Edgar R. Miller throughout the course of this program.

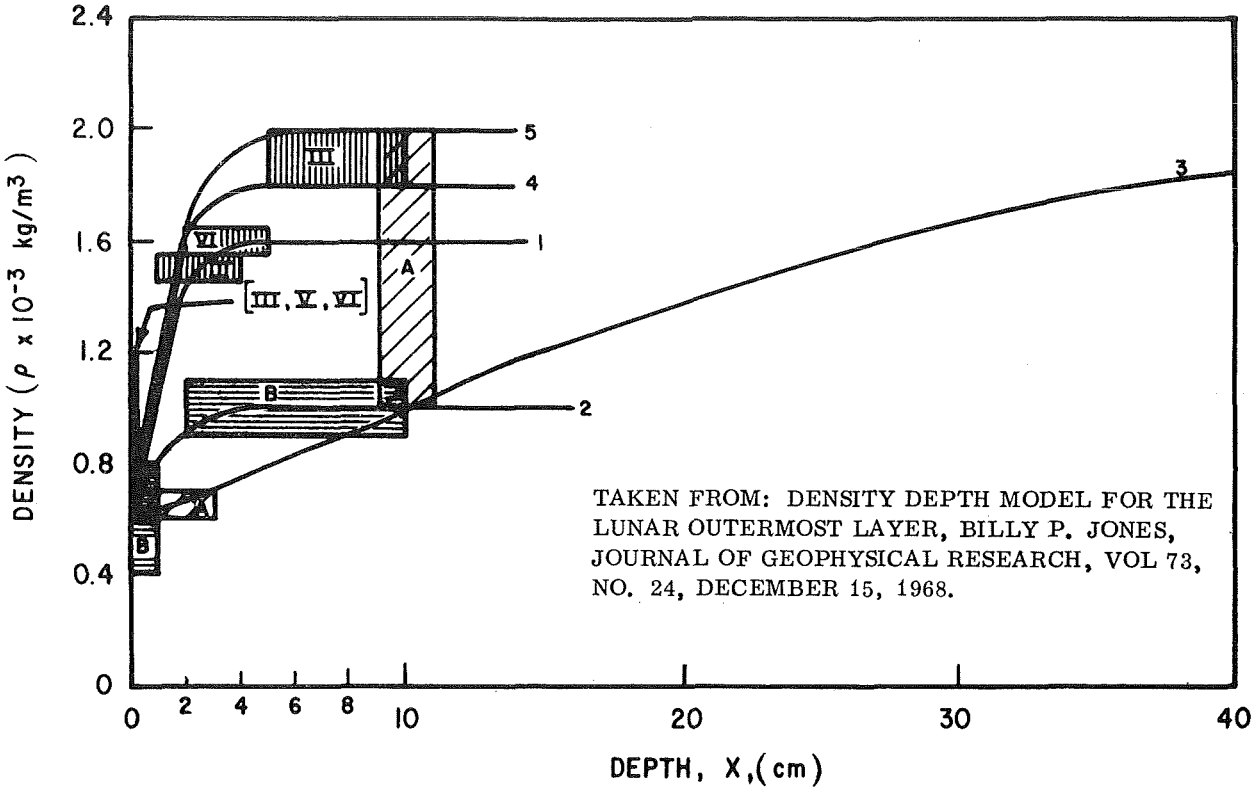

FIGURE 1. DENSITY VERSUS DEPTH IN THE LUNAR OUTERMOST LAYER AND OBSERVATIONAL DATA

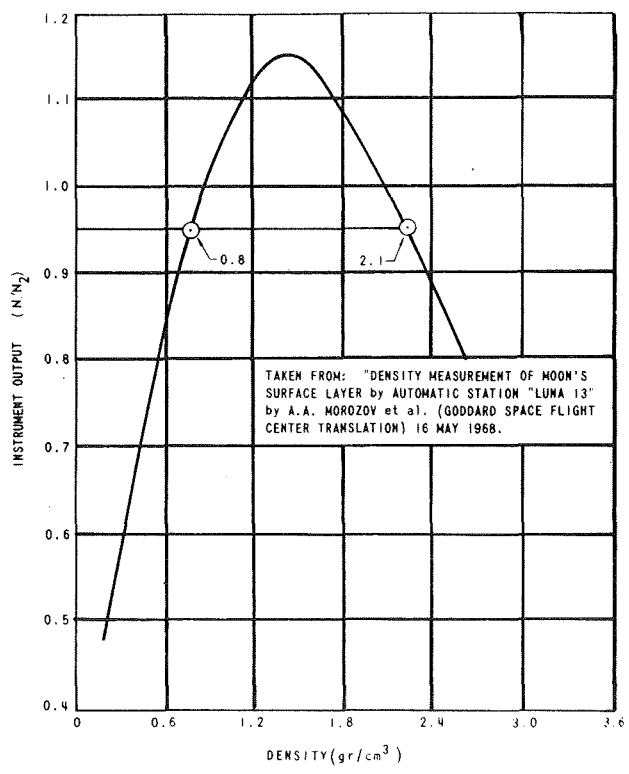

FIGURE 2. CALIBRATION GRAPH OF THE RADIATION DENSIMETER — RUSSIAN LUNA 13

surface. The scattered gamma rays were then detected, yielding an average density value for the first 15 cm of depth. The disadvantage of this method is that the calibration curve is a parabola which, of course, will yield two possible values. The ascending leg of the parabola represents increased Compton scattering by electrons in the volume as the density increases. At a density of about 1.3 g/cm^3, multiple scattering begins to take place, the energy of the gamma rays is decreased, and the gamma rays are absorbed in the medium. Therefore, the problem arises as to which of the two values to choose. The value recorded by the probe as indicated on the ordinate scale is 0.96 which gives density values of 0.8 g/cm^3 and 2.1 g/cm^3. Since these are average values, they roughly agree with the more indirectly obtained results shown in Figure 1.

The Russian investigators discounted the 2.1 g/cm^3 as being too high and accepted 0.8 g/cm^3 as the average density of the upper 15 cm of the lunar surface. However, Scott [3] has concluded that "...the lunar surface material to a depth of a few centimeters at the Surveyor I, Luna 13, Surveyor III, V, VI, and VII landing sites consists of granular material whose density is in the range of

densities of terrestrial soils; i.e., 1.5 to 2.0 g/cm^3." He also concludes that soils of extremely low densities exist only to a depth of 1 to 2 mm.

These investigations provide confidence that the density values of 0.79 g/cm^3 to 1.50 g/cm^3, which were achieved in laboratory experiments by vibration settling, are near or within the postulated values for the lunar surface.

A qualitative experiment to determine the maximum density obtainable with the particulate sample was attempted. One hundred grams of the basalt powder were compressed in a powder-pellet press under a pressure of 5.52×10^8 N/m^2 (8000 psi). The maximum density obtainable was 1.77 g/cm^3. This, of course, was not done in a vacuum and is for a very restricted particle size, so the results are not directly comparable. However, since the density of solid basalt is about 2.4 g/cm^3 to 3.1 g/cm^3, it does indicate that to obtain an average density of 2.1 g/cm^3 for the lunar surface, the volume contains some solid material. Otherwise, for a compacted particulate basalt, this value seems high.

SAMPLE SELECTION

Measurements from laboratory simulations [4] and from the Surveyor alpha scattering experiment [5, 6] have indicated that the lunar surface is composed of a rock which is similar to terrestrial basalt and to basaltic achondrites. Therefore, particulate basalt was chosen for our experiment. Particle size on the lunar surface probably ranges from a few microns up to pebbles and rubble. However, for this first test series it was decided that only the small particle material in the upper few centimeters would be simulated. The best evidence available indicates a mean particle size range of 1 to 100 microns [1]. Therefore, a sample sieved to a range of 37 to 62 microns in diameter was chosen.

TEST PROCEDURE

The sample was baked in a vacuum oven at a temperature of 525° K for five days to remove as many impurities as possible. Then, while it was still hot, the sample was poured into a funnel with a piece of screen wire across the bottom. A vibrator was used to vibrate the funnel, thus sifting the basalt particles into the sample chamber. The initial sifting was done as gently as possible to achieve the lowest density possible. The sample chamber shown in Figure 3 was filled to the top. Since the volume of the chamber and the amount of the basalt powder were known, the bulk density was known. The lowest density achieved was 0.79 g/cm^3. The bell jar was then put into place, and the vacuum chamber was evacuated to 1×10^{-6} N/m^2 (1×10^{-8} torr). The hot oil bath was circulated through the coils in the sample chamber at 360° K for 5 days while the ionization vacuum system pumped. The entire vacuum system was also baked during this time at 360° K. This procedure produced an extremely clean, well-evacuated sample. With the vacuum stabilized, the test series was initiated. The method of thermal conductivity measurement was the Differentiated Line Heat Source developed by Merrill[2]. Data were taken at 360° K, and the sample temperature was changed for measurements throughout as much of the lunar temperature range as was achievable with the temperature control system.

As soon as a sufficient number of thermal conductivity measurements were taken to make a good curve fit, the vacuum chamber pressure was increased to 7 mb (5.25 mm Hg) with carbon dioxide (CO_2), and the Martian environment measurements were conducted.

Then the system was brought up to atmospheric pressure, and the bell jar was removed. An additional amount of basalt was sifted into a mound on top of the sample. The sample chamber was vibrated until the level of the powder was again even with the top of the sample holder. This gave a new density, and the procedure was begun again. This procedure was repeated up to a density of 1.50 g/cm^3. The maximum density attained was 1.61 g/cm^3, which required 12 hours of sample vibration. However, thermal conductivity tests are not yet available for this highest density.

2. Dissertation at Brigham Young University, entitled "Thermal Conductivity Through an Evacuated Idealized Powder over the Temperature Range of 100 to 500° K."

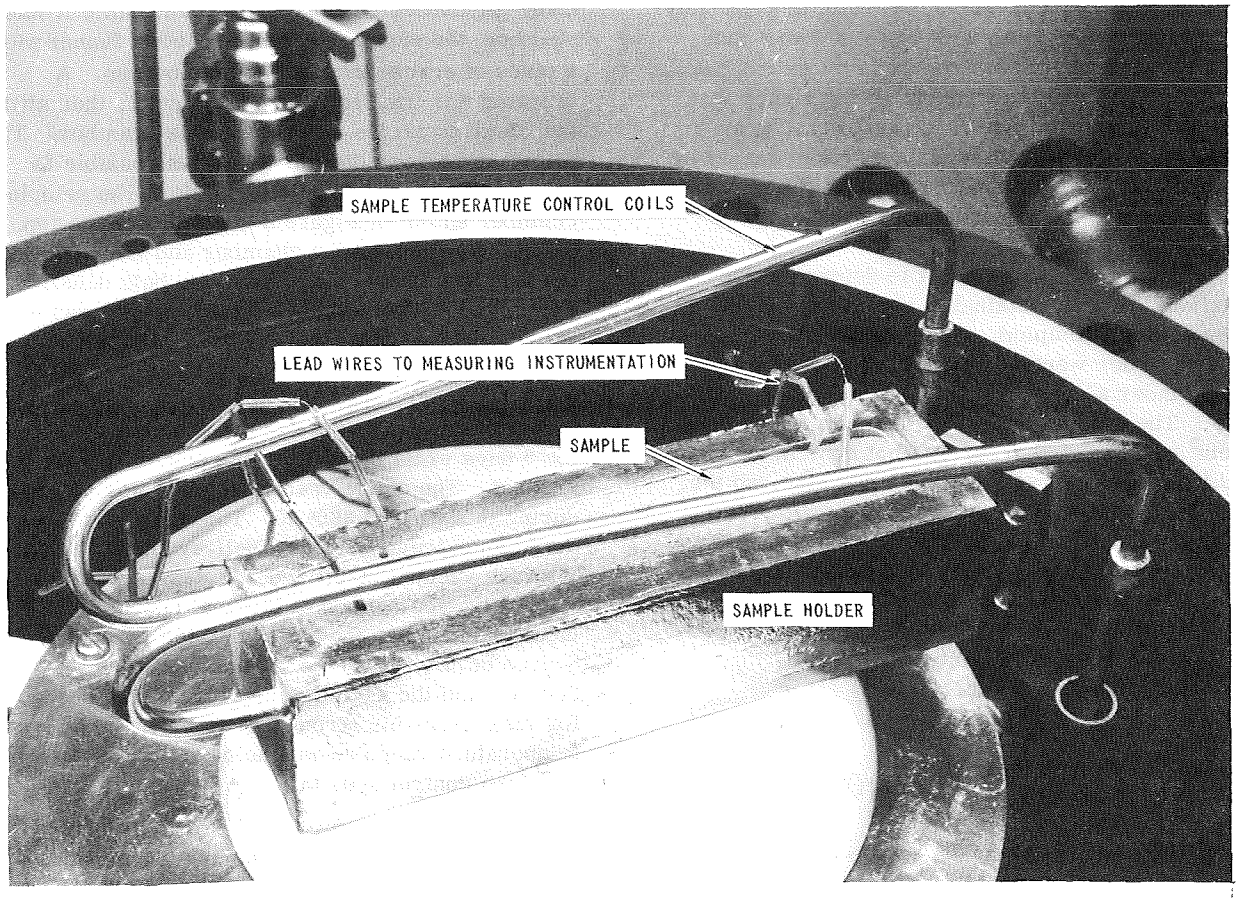

FIGURE 3. SAMPLE HOLDER

RESULTS

THERMAL CONDUCTIVITY DATA: LUNAR ENVIRONMENT

Figure 4 is a plot of the results which yield the thermal conductivity of the sample versus temperature and density under 1×10^{-6} N/m^2 (1×10^{-8} torr) pressure to simulate the lunar environment. The solid curves represent a computer curve fit of the data to Watson's equation, $K = A + BT^3$, for the thermal conductivity of particulate media in a vacuum[3]. The thermal conductivity, K, is a function of a constant conductive term, A, plus a cubic temperature term, BT^3, which represents the radiative transfer in the sample. Curves A, B, C, and E show the excellent agreement between the data and the theoretical curve. Curves D and F did not fit as well as the others. The computer curve fit program yields the A and B coefficients which are given in Table I. These coefficients can be used to calculate thermal conductivities into temperature ranges which could not be achieved experimentally. The dotted portions of the curves show the extrapolations to the computed points at temperatures of 110° K and up to 390° K.

Figure 4 shows a generally increasing thermal conductivity with increasing density but with one exception. Curve C, which is of a higher density

3. Thesis for the California Institute of Technology, entitled "The Thermal Conductivity Measurements of Selected Silicate Powders in Vacuum from 150° - 350° K."

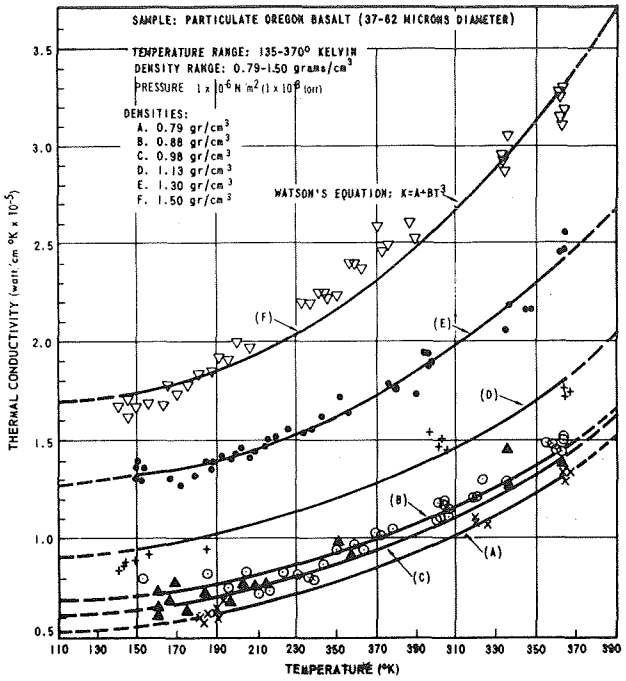

FIGURE 4. THERMAL CONDUCTIVITY OF PARTICULATE BASALT AS A FUNCTION OF TEMPERATURE AND DENSITY

TABLE I. A AND B COEFFICIENTS FROM COMPUTER CURVE FIT PROGRAM

Density g/cm³	$A \times 10^5$ watt/cm° K	$B \times 10^5$ watt/cm° K⁴
0.79	0.509	0.169×10^{-7}
0.88	0.650	0.167×10^{-7}
0.98	0.595	0.172×10^{-7}
1.13	0.887	0.190×10^{-7}
1.30	1.237	0.243×10^{-7}
1.50	1.642	0.343×10^{-7}

than curve B, shows a slightly lower thermal conductivity. To verify the validity of this anomaly would require that this portion of the measurements be repeated, and this has not been done. Since it occurs in a region in which the thermal conductivity dependence is not a strong function of density, it does not pose any particular problem, but it does possibly provide an interesting point for theoretical consideration.

The thermal conductivity-density relationship is shown in Figure 5 with temperature as the parameter. These curves were obtained by a further calculation and extrapolation of the thermal conductivity versus temperature curves in Figure 4 down to temperatures of 50° K and up to 450° K. Then conductivity values were read for specific temperatures from each density curve at 50° K intervals, and the resulting functions were plotted in Figure 5. Thermal conductivity is shown to change by as much as a factor of three over this limited density range. The nonmonotonic portion of each curve is caused by the one anomalous case mentioned above (curve C, Fig. 4).

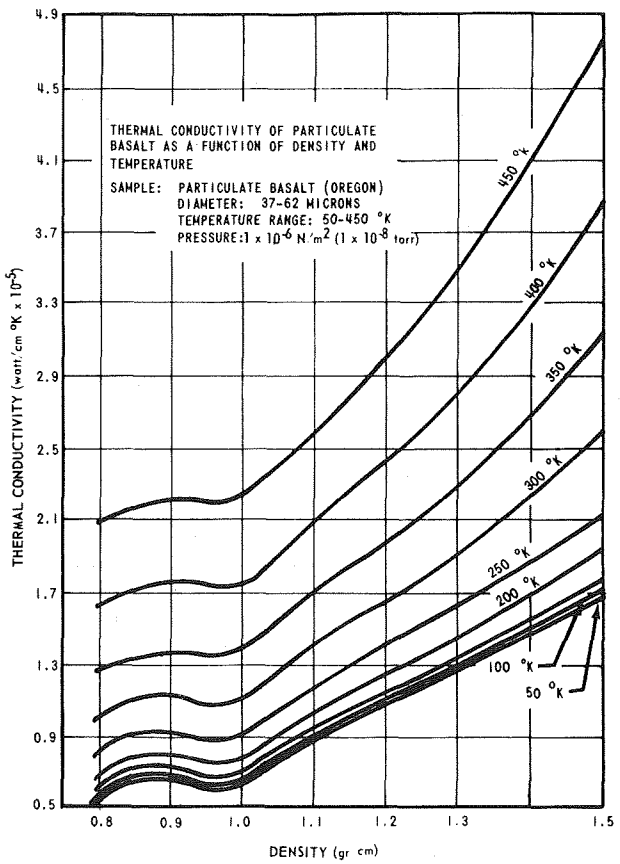

FIGURE 5. THERMAL CONDUCTIVITY OF PARTICULATE BASALT AS A FUNCTION OF DENSITY AND TEMPERATURE

The thermal conductivity-density curve for the 300° K case in Figure 5 is shown in Figure 6 along with literature data on thermal conductivity of some solid basalts. Even though this figure compares data taken in two pressure regimes, the comparison is valid because thermal conductivity of a solid is not a function of pressure.

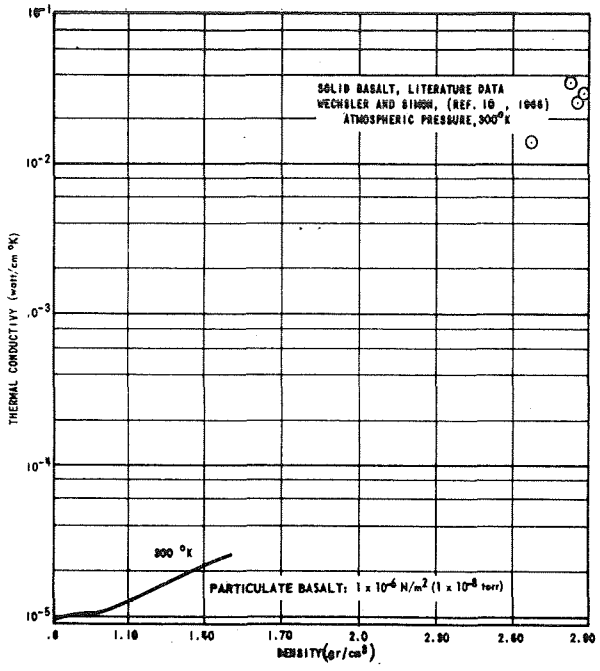

FIGURE 6. THERMAL CONDUCTIVITY OF BASALT AS A FUNCTION OF DENSITY

No attempt is made to interpolate a curve between these sets of data because the effect on thermal conductivity that occurs when separate particles are fused into a solid is not known, However, the figure is useful for showing the four orders of magnitude change that exist between the two cases and the trend of the increasingly compacted powder toward the solid.

THERMAL CONDUCTIVITY DATA: MARTIAN ENVIRONMENT

Observational data have shown that the Martian atmosphere consists primarily of carbon dioxide at a pressure of about 7 mb (5.25 mm Hg) [7]. The temperature range has been shown to vary from about 200° K to 300° K [8, 9]. Between each change in density in the lunar environmental tests, the pressure was raised to 7 mb (5.25 mm Hg) with CO_2 and thermal conductivity tests were conducted over the Martian temperature range. The results, as shown in Figure 7, show only a slight dependence on temperature and density under these conditions. Evidently the interstitial CO_2 tends to negate the effects of temperature and density in the range of the experiments.

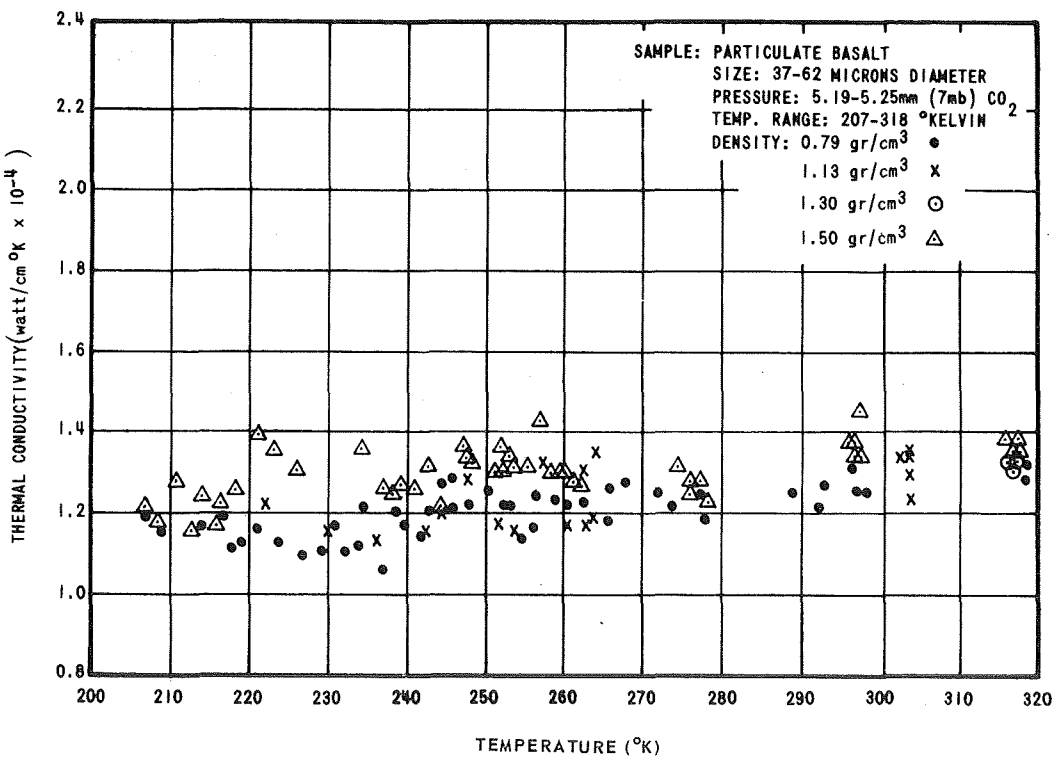

FIGURE 7. THERMAL CONDUCTIVITY OF PARTICULATE BASALT IN A SIMULATED MARTIAN ENVIRONMENT AS A FUNCTION OF TEMPERATURE AND DENSITY

COMPARISON OF LUNAR AND MARTIAN DATA

A summary of the thermal conductivity data in the three pressure regimes is presented in Figure 8 on semi-logarithmic paper for comparison purposes. The literature data for solid basalt at room temperature and atmospheric pressure [10] are shown as circled dots. The Martian data from Figure 7 are represented here by lines drawn through the points. The solid lines through the lunar data from Figure 4 are also shown. This graph clearly shows the vast difference in thermal conductivity when a solid is reduced to a particulate material and is measured under different simulated extraterrestrial environments.

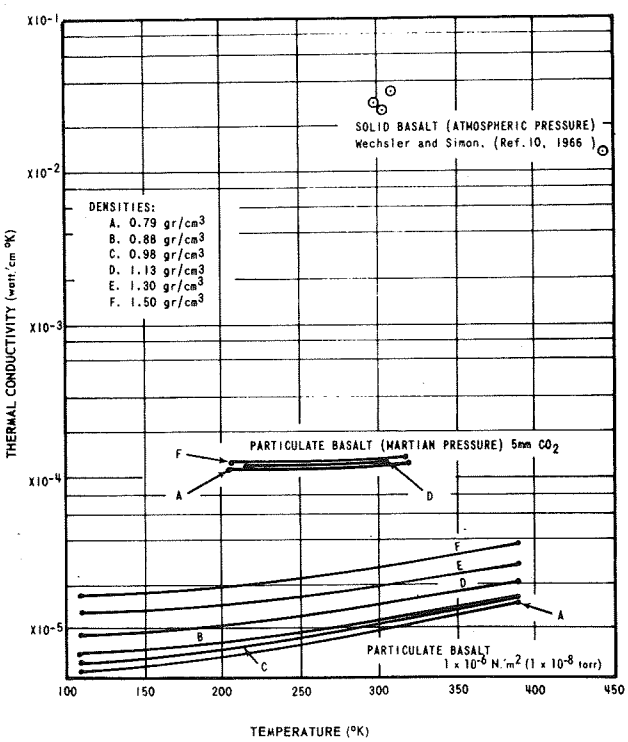

FIGURE 8. THERMAL CONDUCTIVITY OF BASALT

The effects of sample density between the lunar and Martian environments are also evident in this figure. In the Martian tests, the lack of density effect is not surprising because the principal mode of heat transfer is the gaseous convection and conduction of the CO_2. The conductive and radiative heat transfer between particles is overshadowed, and therefore, density effects are slight.

CONCLUSIONS

1. It has been shown that the thermal conductivity of particulate basalt varies with density over the range which simulates the apparent lunar surface density, and the amount of that variation has been established. With these data it will now be possible to refine lunar temperature calculations using density models that are depth dependent and conductivity models that are both depth and temperature dependent. These models will supersede the present homogeneous models, quasi-homogeneous (two layer) models, or models in which conductivity is only temperature dependent.

2. The data presented here will also be useful in providing more insight into the question of the contribution of the conductive and radiative terms to the effective conductivity as discussed by Jones [11], since the increase in density affects the two terms differently. As can be seen in Table I, A increases by a factor of 3 over the density range, while B (which also means BT^3) increases by a factor of 2.

3. On the basis of the qualitative "powder press" data, it is suggested that the 2.1 g/cm^3 density, as recorded by the Luna 13 probe, is too high for a volume of particulate material only and is probably a volume of particulate material with some solid material.

4. Based on a basalt type sample, the magnitude of thermal conductivity expected on the Martian surface has been established. It has been demonstrated that the effects of density and temperature will not be as significant in thermal analyses of the Martian surface as they are in lunar surface studies.

REFERENCES

1. Jones, Billy P.: Density-Depth Model for the Lunar Outermost Layer. Journal of Geophysical Research, Vol. 73, No. 24, December 15, 1968, pp. 7631-7635.

2. Morozov, A. A.; Smorodinov, M. I.; Shvarev, V. V.; and Cherkasov, I. I.: Density Measurement of Moon's Surface Layer by Automatic Station "Luna-13." Translation of Russian report by Goddard Space Flight Center under Contract NAS5-12487.

3. Scott, Ronald F.: The Density of the Lunar Surface Soil. Journal of Geophysical Research, Vol. 73, No. 16, August 15, 1968, pp. 5469-5471.

4. Snoddy, W. C.; Zwiener, J. M.; Newton, Thomas F.; and Russell, L. W.: Infrared Emission During Simulated Lunar Eclipse. Progress in Astronautics and Aeronautics, Vol. 20, 1967, pp. 371-385.

5. Jaffe, L. D.: Surveyor VI Lunar Mission. Journal of Geophysical Research, Vol. 73, No. 16, August 15, 1968, pp. 5297-5300.

6. Turkevich, A. L.; Franzgrote, E. J.; and Patterson, J. H.: Chemical Analysis of the Moon at Surveyor VI Landing Site: Preliminary Results. Surveyor VI: A Preliminary Report, National Aeronautics and Space Administration (Washington, D. C., 1968), Publication No. NASA SP-166, pp. 109-132.

7. Spinrad, Hyron; Schorn, Ronald A.; Moore, Roger; Giver, L. P.; and Smith, Harian J.: High-Dispersion Spectroscopic Observations of Mars I. The CO_2 Content and Surface Pressure. Astrophysical Journal, November 1966, pp. 331-338.

8. Sinton, W. M.; and Strong, John: Radiometric Observations of Mars. Astrophysical Journal, January - May, 1960, pp. 459-469.

9. Gifford, Frank, Jr.: The Surface-Temperature Climate of Mars. Astrophysical Journal, Vol. 123-124, 1956, pp. 154-161.

10. Wechsler, Alfred E.; and Simon, Ivan: Thermal Conductivity and Dielectric Constant of Silicate Materials. Prepared by Arthur D. Little, Inc., Cambridge, Massachusetts, NASA Contract NAS8-20076, December 1966.

11. Jones, Billy P.: Predicting Lunar Temperatures. To be published in Volume 21, Progress in Astronautics and Aeronautics, AIAA, edited by Jerry T. Bevans.

APPROVAL

RESEARCH ACHIEVEMENTS REVIEW
VOLUME III REPORT NO. 6

The information in these reports has been reviewed for security classification. Review of any information concerning Department of Defense or Atomic Energy Commission programs has been made by the MSFC Security Classification Officer. These reports, in their entirety, have been determined to be unclassified.

These reports have also been reviewed and approved for technical accuracy.

G. B. Heller

G. B. HELLER
Director, Space Sciences Laboratory

Karl L. Heimburg

KARL L. HEIMBURG
Director, Astronautics Laboratory

F. B. Moore

F. B. MOORE
Director, Astrionics Laboratory

UNITS OF MEASURE

In a prepared statement presented on August 5, 1965, to the U. S. House of Representatives Science and Astronautics Committee (chaired by George P. Miller of California), the position of the National Aeronautics and Space Administration on Units of Measure was stated by Dr. Alfred J. Eggers, Deputy Associate Administrator, Office of Advanced Research and Technology:

"In January of this year NASA directed that the international system of units should be considered the preferred system of units, and should be employed by the research centers as the primary system in all reports and publications of a technical nature, except where such use would reduce the usefulness of the report to the primary recipients. During the conversion period the use of customary units in parentheses following the SI units is permissible, but the parenthetical usage of conventional units will be discontinued as soon as it is judged that the normal users of the reports would not be particularly inconvenienced by the exclusive use of SI units."

The International System of Units (SI Units) has been adopted by the U. S. National Bureau of Standards (see NBS Technical News Bulletin, Vol. 48, No. 4, April 1964).

The International System of Units is defined in NASA SP-7012, "The International System of Units, Physical Constants, and Conversion Factors," which is available from the U. S. Government Printing Office, Washington, D. C. 20402.

SI Units are used preferentially in this series of research reports in accordance with NASA policy and following the practice of the National Bureau of Standards.

CALENDAR OF REVIEWS

FIRST SERIES (VOLUME I)

REVIEW	DATE	RESEARCH AREA	REVIEW	DATE	RESEARCH AREA
1	2/25/65	RADIATION PHYSICS	12	9/16/65	AERODYNAMICS
2	2/25/65	THERMOPHYSICS	13	9/30/65	INSTRUMENTATION
3	3/25/65	CRYOGENIC TECHNOLOGY	14	9/30/65	POWER SYSTEMS
4*	3/25/65	CHEMICAL PROPULSION	15	10/28/65	GUIDANCE CONCEPTS
			16	10/28/65	ASTRODYNAMICS
5	4/29/65	ELECTRONICS	17	1/27/66	ADVANCED TRACKING SYSTEMS
6	4/29/65	CONTROL SYSTEMS	18	1/27/66	COMMUNICATIONS SYSTEMS
7	5/27/65	MATERIALS			
8	5/27/65	MANUFACTURING	19	1/6/66	STRUCTURES
9	6/24/65	GROUND TESTING	20	1/6/66	MATHEMATICS AND COMPUTATION
10	6/24/65	QUALITY ASSURANCE AND CHECKOUT	21	2/24/66	ADVANCED PROPULSION
11	9/16/65	TERRESTRIAL AND SPACE ENVIRONMENT	22	2/24/66	LUNAR AND METEOROID PHYSICS

SECOND SERIES (VOLUME II)

REVIEW	DATE	RESEARCH AREA	REVIEW	DATE	RESEARCH AREA
1	3/31/66	RADIATION PHYSICS	7	3/30/67	CRYOGENIC TECHNOLOGY
2	3/31/66	THERMOPHYSICS	8**	5/25/67	COMPUTATION
3	5/26/66	ELECTRONICS	9	7/27/67	POWER SYSTEMS
4	7/28/66	MATERIALS	10	9/28/67	TERRESTRIAL AND SPACE ENVIRONMENT
5	9/29/66	QUALITY AND RELIABILITY ASSURANCE	11	11/30/67	MANUFACTURING
6	1/26/67	CHEMICAL PROPULSION	12	1/25/68	INSTRUMENTATION RESEARCH FOR GROUND TESTING

THIRD SERIES (VOLUME III)

REVIEW	DATE	RESEARCH AREA	REVIEW	DATE	RESEARCH AREA
1	3/28/68	AIRBORNE INSTRUMENTATION AND DATA TRANSMISSION	5	11/21/68	COMMUNICATION AND TRACKING
2	5/22/68	ASTRODYNAMICS, GUIDANCE AND OPTIMIZATION	6	1/30/69	THERMOPHYSICS
			7	3/27/69	RADIATION PHYSICS
3	7/25/68	CONTROL SYSTEMS	8	3/23/69	METEOROID PHYSICS
4	9/26/68	AEROPHYSICS			

* Classified. Proceedings not published.

** Proceedings summarized only.

Correspondence concerning the Research Achievements Review Series should be addressed to: Research Planning Office, S&E-R, Marshall Space Flight Center, Alabama

MSFC—RSA, Ala